To the Graduate Council:

I am submitting herewith a dissertation written by William Kelley Tuttle, III, entitled "Levels in ^{113,115}In as Seen by the Coulomb Excitation and (HI,xn) Reactions." I recommend that it be accepted in partial fulfillment of the requirements for the degree of Doctor of Philosophy, with a major in Physics.

Paul H. Stelson

Paul H. Stelson, Major Professor

We have read this dissertation
and recommend its acceptance:

Felix E. Obenshain Jr.

Russell L. Robinson

Leo J. Rieding Jr.

J. Davis O'Kelley

Accepted for the Council:

Hilton A. Smith

Vice Chancellor
Graduate Studies and Research

LEVELS IN ^{113,115}In AS SEEN BY THE COULOMB EXCITATION AND (HI,xn) REACTIONS

A Dissertation

Presented for the

Doctor of Philosophy

Degree

The University of Tennessee

William Kelley Tuttle, III

March 1976

1270518

ACKNOWLEDGEMENTS

It is a pleasure to express my sincere appreciation to Dr. P. H. Stelson who directed the research, and to Drs. R. L. Robinson, W. T. Milner and F. K. McGowan for their considerable collaboration and involvement in the accomplishment of this work. I also wish to thank Drs. L. L. Riedinger, R. O. Sayer, S. Raman, and H. Kim for their helpful suggestions and for their assistance in taking data.

Mrs. Anita Barker was especially patient and diligent in typing the manuscript under trying conditions. Miss Lynda Hawkins and Mrs. Virginia Hill were of great help in typing the rough draft and the manuscript for the associated journal article.

The research described in this dissertation was carried out in the Physics Division of the Oak Ridge National Laboratory, which is operated by Union Carbide Corporation under contract with the U. S. Energy Research and Development Administration. The assistance of the entire staff of the Van de Graaff Laboratory, particularly the staff of the Tandem accelerator, and financial support from the U. S. Public Health Service in the form of a Radiological Health Physics fellowship and from Oak Ridge Associated Universities in the form of a Laboratory Participation front are greatfully acknowledged.

The doctoral committee consisted of Professors P. H. Stelson, L. L. Riedinger and F. E. Obenshain, Jr. of the Physics Department and G. D. O'Kelley of the Chemistry Department of the University of Tennessee, and Dr. R. L. Robinson of ORNL.

I wish also to thank my wife Charlene and son Kelley for their patience and understanding throughout this research. We finally made it.

ABSTRACT

Having one proton hole in a major proton shell closing at Z = 50 makes the odd mass indium nuclei prime candidates for description by the weak coupling model. Thus, these nuclei, particularly ^{115}In have been the subject of a number of investigations, both theoretical and experimental. These studies have postulated that a deformed rotational band coexists with the core-coupled states. The purpose of the Coulomb excitation study was to update the information on ^{115}In and to do a thorough study of ^{113}In for which little information is known. In the (HI,xn) study, it was hoped that the deformed rotation band could be found.

For the Coulomb excitation measurements, four types of experiments were performed. First, using beams of 9.4, 10.0, and 10.6 MeV ^{4}He ions, γ-ray yields were taken with an angle between the beam and the detector, θ, of 55°. With these data one can confirm existing level diagrams, look for new transitions, and measure B(E2)'s and branching ratios. Secondly, γ-γ coincidence measurements were performed with a 10.6 MeV ^{4}He beam to confirm the level diagrams and search for new transitions. Next, angular distributions were taken for a 10.0 MeV ^{4}He ion beam to determine spins, parities and mixing ratios. Finally, a beam of ^{16}O ions was used to determine the lifetimes of states whose decaying γ rays showed Doppler broadening.

For the ^{110}Pd(^{6}Li,3n)^{113}In measurements, two types of experiments were performed, both with a 24 MeV ^{6}Li beam. First γ-γ coincidences were performed to find new transitions feeding those states previously

known. Next, angular distributions were performed to confirm old spin assignments and to establish a basis for assignments to new levels observed.

The results of the Coulomb excitation studies were that ^{113}In is structurally very similar to ^{115}In. Both nuclei can, to first order, be described by using an intermediate coupling strength in a weak coupling model. A firm experimental basis for spin and parity assignments to all levels except one (1630 keV in ^{113}In) was established.

In the (HI,xn) studies, levels which are candidates for higher lying core-coupled states were observed. Additionally, a strongly populated cascade was observed which is a good candidate (but not definitely confirmed) for the deformed rotational band. Finally, a very puzzling cascade of low energy ($\sim$ 200 keV) γ rays was observed to feed a level at 2.2 MeV.

TABLE OF CONTENTS

CHAPTER		PAGE
1.	INTRODUCTION	1
2.	NUCLEAR MODELS	4
	The Shell Model	
	Collective Models	
	Unified Models	
3.	THE COULOMB EXCITATION AND (HI,xn) REACTIONS	21
	The Coulomb Excitation Reaction	
	The (HI,xn) Reaction	
	The Extraction of Nuclear Properties	
4.	EXPERIMENTAL ARRANGEMENT AND PROCEDURE	48
	General	
	The γ-Ray Singles Experiments	
	The γ-γ Coincidence Experiments	
	Ge(Li) Detector Efficiency	
	Reduction of Spectra	
5.	EXPERIMENTAL RESULTS	65
	Coulomb Excitation Results	
	Discussion of Level Properties (Coulomb Excitation)	
	Results from $^{110}Pd(^{6}Li,3n)^{113}In$	
	Discussion of Level Properties ($^{110}Pd(^{6}Li,3n)^{113}In$)	
6.	DISCUSSION AND CONCLUSIONS	110
	Discussion of Structure (Coulomb Excitation)	
	Discussion of Structure Observed in the $^{110}Pd(^{6}Li,3n)^{113}In$ Reaction	
	Conclusions	
REFERENCES		124
VITA		128

LIST OF TABLES

TABLE		PAGE
5-1.	Summary of coincidence information obtained from the Coulomb excitation of $^{113,115}In$	69
5-2.	Summary of $B_{ex}(E2)$, $B_{ex}(E3)$ values obtained from the Coulomb excitation of $^{113,115}In$	74
5-3.	Summary of γ-ray anisotropy results from the Coulomb excitation of $^{113,115}In$	78
5-4.	Mean lives of Coulomb excited states in $^{113,115}In$ obtained by Doppler line shape analysis	79
5-5.	Summary of information obtained from the Coulomb excitation of ^{113}In	83
5-6.	Summary of information obtained from the Coulomb excitation of ^{115}In	84
5-7.	Summary of coincidence information obtained from the $^{110}Pd(^{6}Li,3n)^{113}In$ reaction	93
5-8.	Angular distribution coefficients obtained from the $^{110}Pd(^{6}Li,3n)^{113}In$ reaction	97
5-9.	Table of $R_{\gamma_1-\gamma_2}(90°,22°)$ for the strongest cascade observed in the $^{110}Pd(^{6}Li,3n)^{113}In$ reaction	102
5-10.	Table of $R_{\gamma_1-\gamma_2}(90°,22°)$ for the $^{110}Pd(^{6}Li,3n)^{113}In$ reaction	103
6-1.	Comparison of calculated and experimental $B_d(E2)$ values for ^{115}In	111
6-2.	Comparison of calculated and experimental $B_d(M1)$ values for ^{115}In	112

LIST OF FIGURES

FIGURE		PAGE
2-1.	The neutron- and the proton-level scheme in the shell model	6
2-2.	Energy levels for a simple vibrational nucleus	10
2-3.	Angular momentum diagram for deformed nuclei	13
2-4.	Energy levels for a deformed even-even nucleus with β- and γ-vibrational bands	14
3-1.	Schematic diagram illustrating the formation and subsequent decay of a compound nuclear system	31
3-2.	Diagram illustrating possible de-excitation modes of highly excited nuclei	33
3-3.	Energy level diagram illustrating various mechanisms for populating a level	38
4-1.	Schematic illustration of the arrangement for performance of Coulomb excitation and (HI,xn) experiments with the ORNL EN tandem Van de Graaff accelerator	49
4-2.	Block diagram of the electronics setup for γ-ray singles experiments	53
4-3.	Ge(Li) detector positions for Coulomb excitation and (HI,xn) studies, top view	55
4-4.	Block diagram of electronics setup adjacent to the target for γ-γ coincidence measurements	57

FIGURE PAGE

4-5. Block diagram of the electronics setup adjacent to the data acquisition system for γ-γ coincidence measurements 58

5-1. Energy levels observed in the Coulomb excitation of ^{113}In 66

5-2. Energy levels, observed in the Coulomb excitation of ^{115}In 67

5-3. Ge(Li) pulse-height spectrum of the low energy γ-rays from an enriched ^{113}In target bombarded with 10.0 MeV ^{4}He ions 70

5-4. Ge(Li) pulse-height spectrum of the high energy γ-rays from an enriched ^{113}In target bombarded with 10.0 MeV ^{4}He ions 71

5-5. Ge(Li) pulse-height spectrum of the low energy γ-rays from a natural indium target bombarded with 10.0 MeV ^{4}He ions 72

5-6. Ge(Li) pulse-height spectrum of the high energy γ-rays from a natural indium target bombarded with 10.0 MeV ^{4}He ions 73

5-7. Level diagram of ^{113}In displaying excitation strengths to the various states of ^{113}In 75

5-8. Level diagram of ^{115}In displaying excitation strengths to the various states of ^{115}In 76

FIGURE PAGE

5-9. Doppler-broadened γ-ray peaks observed when ^{113}In was Coulomb excited with ^{16}O projectiles 80

5-10. Doppler-broadened γ-ray peaks observed when ^{115}In was Coulomb excited with ^{4}He projectiles 81

5-11. Doppler-broadened γ-ray peaks observed when ^{115}In was Coulomb excited with ^{16}O projectiles 82

5-12. Level diagram of all states in ^{113}In as observed in the $^{110}Pd(^{6}Li,3n)^{113}In$ reaction except those known levels for which no feeding could be established . . 90

5-13. Level diagram of states observed in the $^{110}Pd(^{6}Li,3n)$ ^{113}In reaction to feed the $11/2^{+}$ 1173.0 KeV and $13/2^{+}$ 1344.4 KeV levels 91

5-14. Level diagram of states in ^{113}In observed in the $^{110}Pd(^{6}Li,3n)^{113}In$ reaction which do not feed any of the states observed in the Coulomb excitation reaction 92

5-15. Ge(Li) pulse-height spectrum of the 121 to 583 KeV γ rays from an enriched ^{110}Pd target bombarded with 24 MeV ^{6}Li ions 98

5-16. Ge(Li) pulse-height spectrum of the 583 to 1046 KeV γ rays from an enriched ^{110}Pd target bombarded with 24 MeV ^{6}Li ions 99

5-17. Ge(Li) pulse-height spectrum of the 1046 to 1483 KeV γ rays from an enriched ^{110}Pd target bombarded with 24 MeV ^{6}Li ions 100

FIGURE PAGE

5-18. Ge(Li) pulse-height spectrum of the 1483 to 1954 KeV γ rays from an enriched ^{110}Pd target bombarded with 24 MeV ^{6}Li ions 101

6-1. Plot obtained by Dietrich of $B_{ex}(E2,9/2 \rightarrow J)$ versus coupling strength for the $g_{9/2}^{-1} \otimes 2_1^+(Sn)$ multiplet in ^{115}In 113

6-2. Plot calculated by Dietrich of B(M1) values versus coupling strength for the $g_{9/2}^{-1} \otimes 2_1^+(Sn)$ multiplet in ^{115}In 114

CHAPTER 1

INTRODUCTION

It is the purpose of this research to investigate the level structure of the odd In isotopes, specifically ^{113,115}In. The synopsis of the investigation will be presented in five chapters, the purpose and content of which is the subject of this introduction.

First of all, the question of what might be expected is addressed in Chapter 2, Nuclear Models. Since these indium nuclei are one particle away from the major proton shell closing at Z = 50, they are prime candidates for description by the weak coupling model. Thus it is expected that the collective features would be dominated by a quintet of states with $I^{\pi} = 5/2^{+}$ to $13/2^{+}$ resulting from the coupling of a hole in the $g_{9/2}$ proton shell ($g_{9/2}^{-1}$) with the one phonon quadrupole vibrational state (2_1^{+}) of the adjacent even Sn core (denoted $g_{9/2}^{-1} \otimes 2_1^{+}$). If the coupling strength itself is weak, the sum of the $B_{ex}(E2)$ for this multiplet should be the same as the $B_{ex}(E2, 0^{+} \rightarrow 2^{+})$ for the adjacent even Sn core, and each $B_d(E2)$ for the multiplet should be the same as the $B_d(E2, 2^{+} \rightarrow 0^{+})$ for the adjacent even Sn core. Furthermore, the "center of gravity" of the multiplet should be the energy of the 2^{+} state of the adjacent even Sn core, and there can be no M1 component in the ground state transitions. The development of the weak coupling model will be emphasized in Chapter 2 while at the same time trying to bring out its relationship to the subject as a whole and suggesting other descriptions.

Next, one asks the question "How can nuclear properties be determined?". The Coulomb excitation and (HI, xn) reactions have been chosen for this work, and are the subject of Chapter 3, the (HI, xn) work being a supplement to the more extensive Coulomb excitation study. The theory of each reaction will be discussed in a general overview, while the extraction of specific nuclear properties will be presented in greater detail.

Chapter 4, Experimental Arrangement and Procedure, details the implementation of Chapter 3, i.e., "How the nuclear properties were determined." For the Coulomb excitation studies, four types of experiments were performed. First, γ-ray yields were taken at E_α = 9.4, 10.0, and 10.6 MeV with the angle between the beam and γ-ray $\theta = 55°$ to confirm established level diagrams, to look for new transitions, and to obtain B(E2)'s and branching ratios. Next, γ-γ coincidences were taken with E_α = 10.6 MeV as a check of level diagrams and branching ratios. Thirdly, angular distributions ($\theta = 0°, 90°$), E_α = 10.0 MeV were taken to establish spins, parities, and E2/M1 mixing ratios. Finally, a beam of ^{16}O ions was used to determine lifetimes of states which showed Doppler broadening. This last measurement in some cases can eliminate assignments permitted by the angular distributions. In the case of the (HI, xn) studies, two types of measurements were performed, both using a 24 MeV ^{6}Li beam to make ^{113}In by the selective $^{110}Pd(^{6}Li, 3n)^{113}In$ reaction. First γ-γ coincidences were taken to establish new transitions and levels. After this, angular distributions were taken to determine spin and parity assignments for new levels and to establish the strengths of the various transitions observed.

The results (both calculated and directly measured) of the measurements are presented in Chapter 5. Here the level structures deduced and their properties are presented. This chapter essentially answers the question "What were the nuclear properties found?". It forms the basis for the final, and perhaps the most important, chapter.

The final chapter, Chapter 6, is entitled Discussion and Conclusions. Here, the results are discussed within the framework of current nuclear models, and are compared to previous findings. Failings and shortcomings of current theories are pointed out and the possibilities for future work are discussed.

CHAPTER 2

NUCLEAR MODELS

A model as defined by the dictionary[1] is: "10: a description or analogy used to help visualize something which cannot be directly observed. 11: a system of postulates, data and inferences presented as a mathematical description of an entity". Accordingly, a nuclear model should fit some data (as it must), predict some other data (a test) and, hopefully, should contain both physical insight and a firm theoretical basis.

Generally speaking, nuclear models have proceeded along two lines; individual particle or shell models and collective models. These have been synthesized into so-called unified models. These three types will be discussed here in fairly general terms with more detail for aspects particularly relevant to the indium nuclei. Since this is an overview and nothing new is presented, the treatment here follows and borrows heavily from standard books[2-4] and fundamental papers.[5-7]

1. THE SHELL MODEL

Because of the success of atomic shell theory, it has always been tempting to describe the nucleus in terms of a shell model. Early theoretical workers (1930-1940) were, however, troubled with the concept that the strong, short range nuclear force could somehow average out to a spherically symmetric central potential. As time went on, more and more experimental evidence pointed to the existence of so-called "magic

numbers" (Z,N = 2,8,20,28,50,82) for protons and neutrons. This overwhelming collection of data necessitated some attempts, the first of which used potentials such as an infinite square well or an infinite harmonic oscillator. These yielded promising, but not entirely satisfactory results. Independently, Mayer[8], and Haxel, Jensen and Suess[9] were able to obtain the magic numbers by assuming a potential of the form

$$V(r) = -V_0 + \tfrac{1}{2} M\omega^2 r^2 - \frac{2\alpha}{\hbar^2}(\vec{l}\cdot\vec{s}) \qquad (2\text{-}1)$$

where the filling of levels is governed by the Pauli principle. Figure 2-1 shows an energy level diagram obtained using such a potential.

The simplest shell model is the extreme single particle shell model. It assumes that, in the nuclear ground state, individual nucleons are paired with like nucleons, so the bulk of properties are determined by the last unpaired nucleon. Thus for indium (Z=49), a ground state of $I^\pi = 9/2^+$ is expected due to a hole in the $g_{9/2}$ proton shell. States with $I^\pi = 1/2^-$, $3/2^-$, $5/2^-$ are also expected due to holes in the $2p_{1/2}$, $2p_{3/2}$ and $1f_{5/2}$ shells. For higher energy excitations, states of a two-hole (in the $1g_{9/2}$ shell), single particle (in the $1g_{7/2}$, $2d_{5/2}$, $2d_{3/2}$, $3s_{1/2}$ shells) nature with $I^\pi = 7/2^+$, $5/2^+$, $3/2^+$, $1/2^+$ might also be observed.

Further refinements in the shell model, such as considering interactions between nucleons in unfilled shells, have been carried out, but will not be considered here.

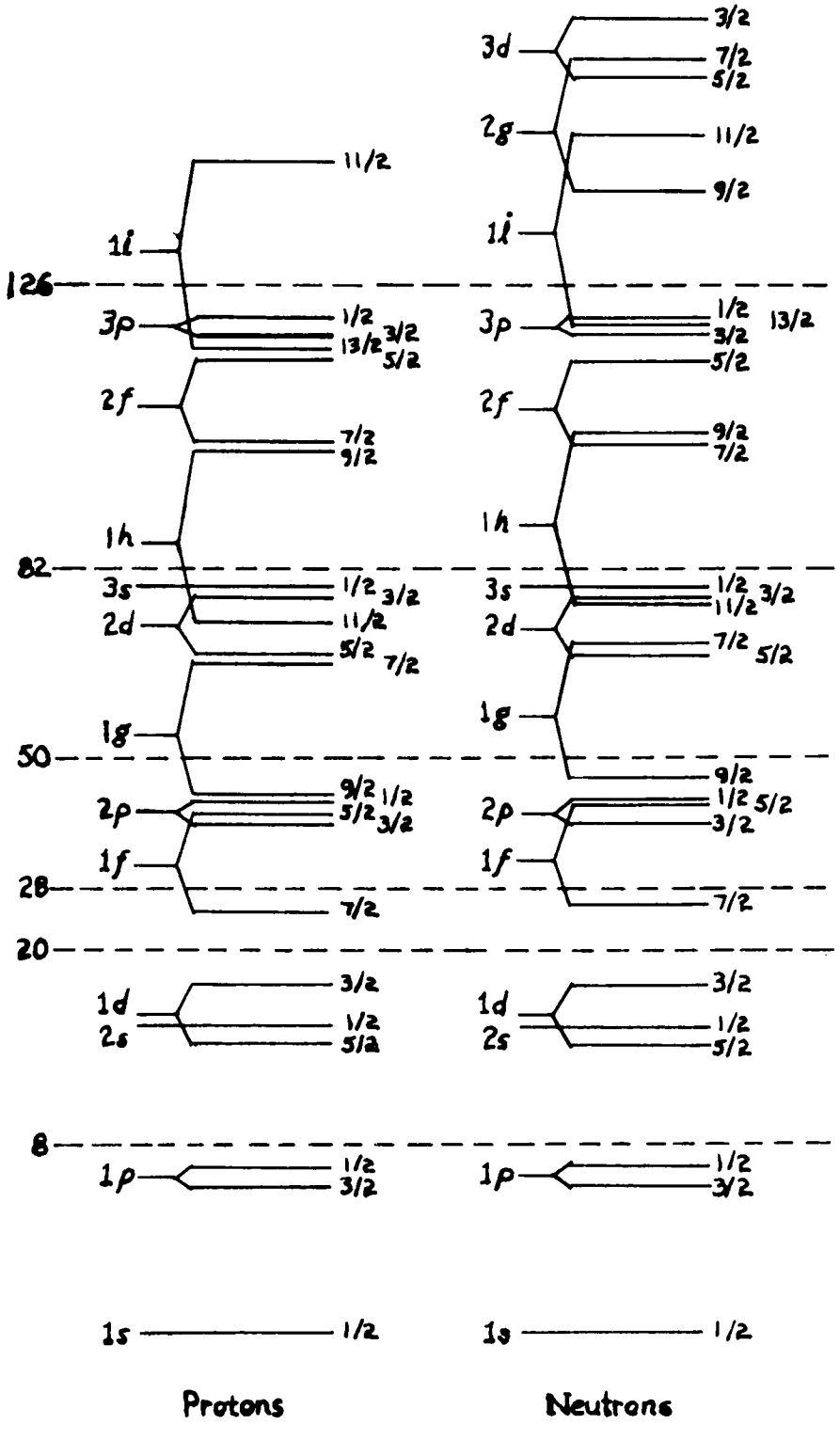


Figure 2-1. The neutron- and the proton-level scheme in the shell model. The calculations are by Klinkenberg.[10] The proton-energy levels have been corrected for the proton's Coulomb energy.

2. COLLECTIVE MODELS

The need for a collective type of model was first seen in the late 1930's with theoretical attempts to explain nuclear fission. Perhaps its first formulation was by Weizsacker[11] who considered the nucleus as a liquid drop to develop his semiempirical mass formula. A bit later, Flügge[12] was the first to discuss surface vibrations and rotations of nuclei. Rainwater,[13] in order to explain large quadrupole moments, suggested that a single odd nucleon could polarize a core. However, perhaps the most significant contribution to the model, and the real impetus for bringing it to the forefront, was provided by the works of A. Bohr and B. R. Mottelson. Bohr[5] worked out the basic model, especially its quantization. Bohr and Mottelson[6] generalized and extended it. Since 1953, various coauthors with Bohr and Mottelson have continued to extend development of this model.

The formulation of the collective model starts by expressing the nuclear radius in a form such as

$$R(\theta,\phi,t) = R_o \left[1 + \sum_{\lambda=0}^{\infty} \sum_{\mu=-\lambda}^{+\lambda} (-1)^{\mu} \alpha_{\lambda,-\mu}(t)\, Y_{\lambda\mu}(\theta,\phi)\right] . \qquad (2\text{-}2)$$

By allowing the expansion parameters $\alpha_{\lambda\mu}$ to differ for a particular (λ,μ), and allowing them to have time variation, a multitude of nuclear shapes are allowed, and these shapes may have time variation. The terms with $\lambda = 0$ correspond to a volume change of the nucleus ("breathing mode") and are expected to be extremely high in energy. The terms with $\lambda = 1$ may be shown (for small $\alpha_{1\mu}$) to correspond to translation, and

therefore are not considered. Terms with $\lambda = 2$ are called quadrupole terms, and are usually those which are discussed in some detail. It should be noted that because of symmetry properties for $\lambda = 2$, there are only five independent expansion coefficients, $\alpha_{2\mu}$.

Now, the Hamiltonian for the system may be expressed as

$$H = T(\pi_{\lambda\mu}, \alpha_{\lambda\mu}) + V(\alpha_{\lambda\mu}), \tag{2-3}$$

where the $\pi_{\lambda\mu}$ are the canonically conjugate momenta to the variable $\alpha_{\lambda\mu}$. Considering $\lambda = 2$ only and assuming small $\pi_{2\mu}$ and $\alpha_{2\mu}$, expansion yields

$$T(\pi_{\lambda\mu}, \alpha_{\lambda\mu}) = \frac{\sqrt{5}}{2} \frac{1}{B_2} \sum_{\mu,\mu'} C^{220}_{\mu\mu'0} \pi_{2\mu} \pi_{2\mu'}$$

$$+ \text{Higher Order Terms (H.O.T.)} \ldots\ldots \tag{2-4}$$

and

$$V(\alpha_{2\mu}) = \frac{C}{\sqrt{5}} \sum_{\mu,\mu'} C^{220}_{\mu\mu'0} \alpha_{2\mu} \alpha_{2\mu'} + \text{H.O.T.} \ldots\ldots . \tag{2-5}$$

The form of these expressions can be made more plausible by hydrodynamic arguments. This means considering nuclear matter to be an incompressible fluid with irrotational flow.

It is worthwhile emphasizing at this time the importance of the expression of the potential energy surface, (2-5). The special properties of the nucleus (e.g., deformed or spherical ground and excited states, harmonic or anharmonic vibrations, coexistence of different shapes, etc.) are for the most part determined by the expression. It is easiest (both for collective and unified models) to consider two cases.

First, for small oscillations about a spherical shape only first order terms are of importance, so the Hamiltonian is written as

$$H = \frac{1}{2} \sum_{\lambda,\mu} (|\pi_{\lambda\mu}|^2 / B_\lambda + C_\lambda |\alpha_{2\mu}|^2) . \tag{2-6}$$

To quantize, recall that the Hamiltonian for the harmonic oscillator is

$$H = p^2/2m + m\omega^2 q^2/2 , \tag{2-7}$$

so that its quantum mechanics, already well known (see, e.g., Merzbacher[14]), may be directly applied. Resultant wave functions are of the form $|\lambda NLM\rangle$ with notations as follows: λ is the type of phonon vibration, N is the number of phonons of the type, L is the associated angular momentum, and M is the z-component of L. Shown in Figure 2-2 is a schematic diagram of energy levels for the simple vibrational model. The assumption of a constant density irrotational fluid implies that

$$\omega_3 \approx 2.2\, \omega_2 . \tag{2-8}$$

The second case of collective motion to consider is a more general expression for the Hamiltonian. For this case, more physical insight is

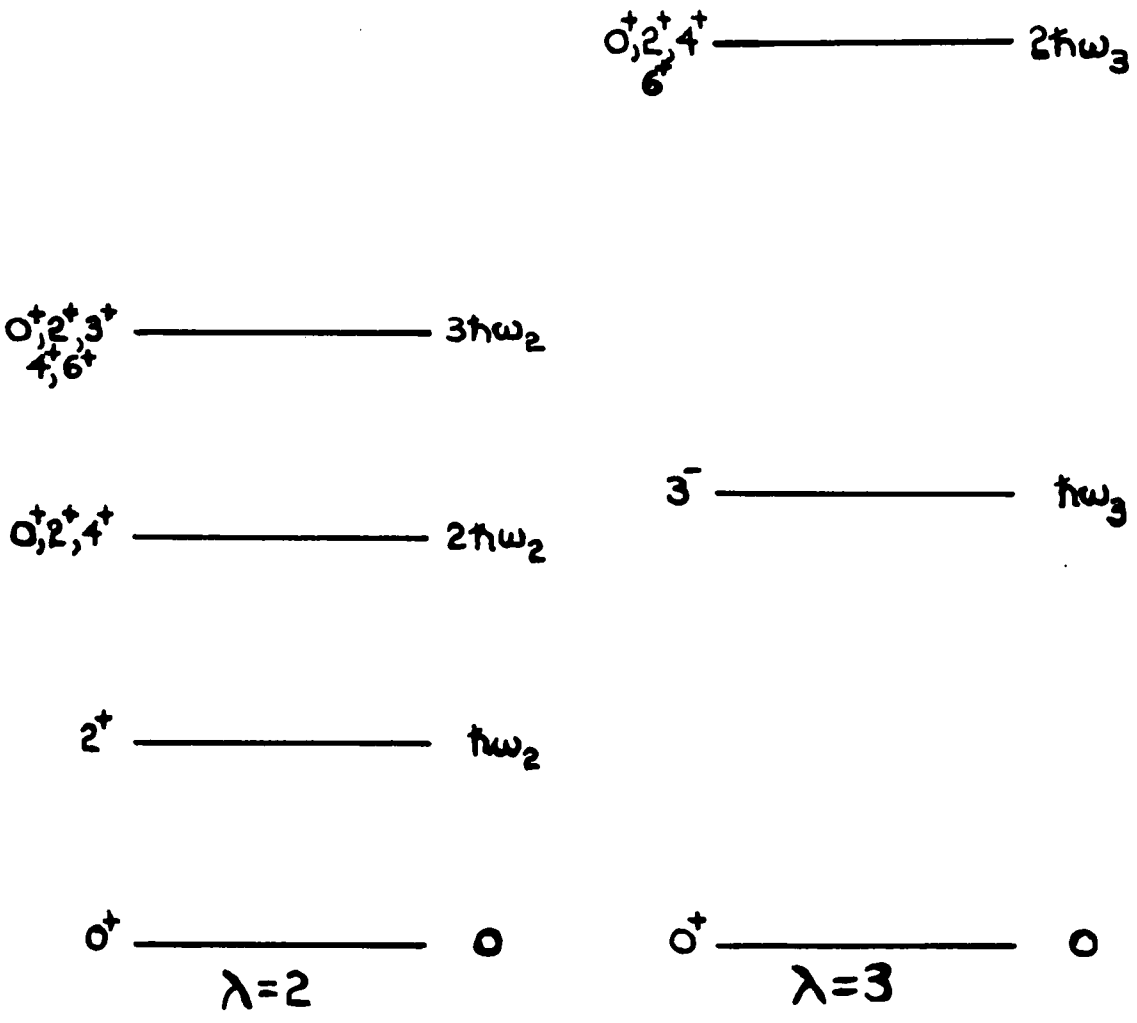


Figure 2-2. Energy levels for a simple vibrational nucleus.

obtained (considering $\lambda = 2$ only) by making a transformation of variables. Instead of the set $\{\alpha_{2\mu}\}$, consider the set $\{\beta,\gamma, \phi, \theta,\psi\}$ where

$$\alpha_{20} = \beta \cos\gamma \tag{2-9}$$

$$\alpha_{22} = (\beta/\sqrt{2}) \sin\gamma \tag{2-10}$$

and (ϕ, θ,ψ) are the Euler angles which specify the orientation of the principal axis of the nucleus with respect to the space fixed axes. Under the transformation, the expression for the kinetic energy (to first order) becomes

$$T = T_{VIB} + T_{ROT} = (B/2)(\dot{\beta}^2 + \beta^2\dot{\gamma}^2) + \frac{1}{2}\sum_{k=1}^{3} Q_k \omega_k^2 , \tag{2-11}$$

where

$$Q_k = 4B\beta^2 \sin^2(\gamma - k\tfrac{2\pi}{3}), \tag{2-12}$$

and the potential energy (to the first order) becomes

$$V = \tfrac{1}{2} C\beta^2 , \tag{2-13}$$

where

$$\beta^2 = \sum_{\mu} |\alpha_{2\mu}|^2 \tag{2-14}$$

is a measure of the total deformation of the nucleus. Using the angular momentum representation for wave functions, and referring to Figure 2-3, for an axially symmetric rotor ($\mathcal{I}_1 = \mathcal{I}_2 = \mathcal{I}_0 \neq \mathcal{I}_3$) we have

$$T_{ROT} = \frac{\hbar^2}{2}\left[\frac{L(L+1)-K^2}{\mathcal{I}_0} + \frac{K^2}{\mathcal{I}_3}\right]. \qquad (2\text{-}15)$$

Now, assume small oscillations around a deformed shape, that is write the potential energy as

$$V(\beta,\gamma) = \tfrac{1}{2} C_\beta (\beta-\beta_0)^2 + \tfrac{1}{2} C_\gamma \gamma^2. \qquad (2\text{-}16)$$

Solution of the Schroedinger equation for this system is facilitated by including the last term of (2-15) in a T'_{VIB} term in the Hamiltonian, so that the equation

$$(T'_{ROT} + T'_{VIB} + V(\beta,\gamma))\Psi(\theta_i,\beta,\gamma) = E\Psi(\theta_i,\beta,\gamma) \qquad (2\text{-}17)$$

has solutions of the form

$$\Psi(\theta_i,\beta,\gamma) = f(\beta)g(\gamma)|LMK\rangle. \qquad (2\text{-}18)$$

Allowed energy levels are

$$E = \hbar\omega_\beta(n_\beta+\tfrac{1}{2}) + \hbar\omega_\gamma(n_\gamma+\tfrac{1}{2}) + \frac{\hbar^2}{2\mathcal{I}_0}[L(L+1)-K^2]. \qquad (2\text{-}19)$$

An energy level diagram for the basic three rotational bands (ground state, beta, and gamma) is shown in Figure 2-4. Other effects such as

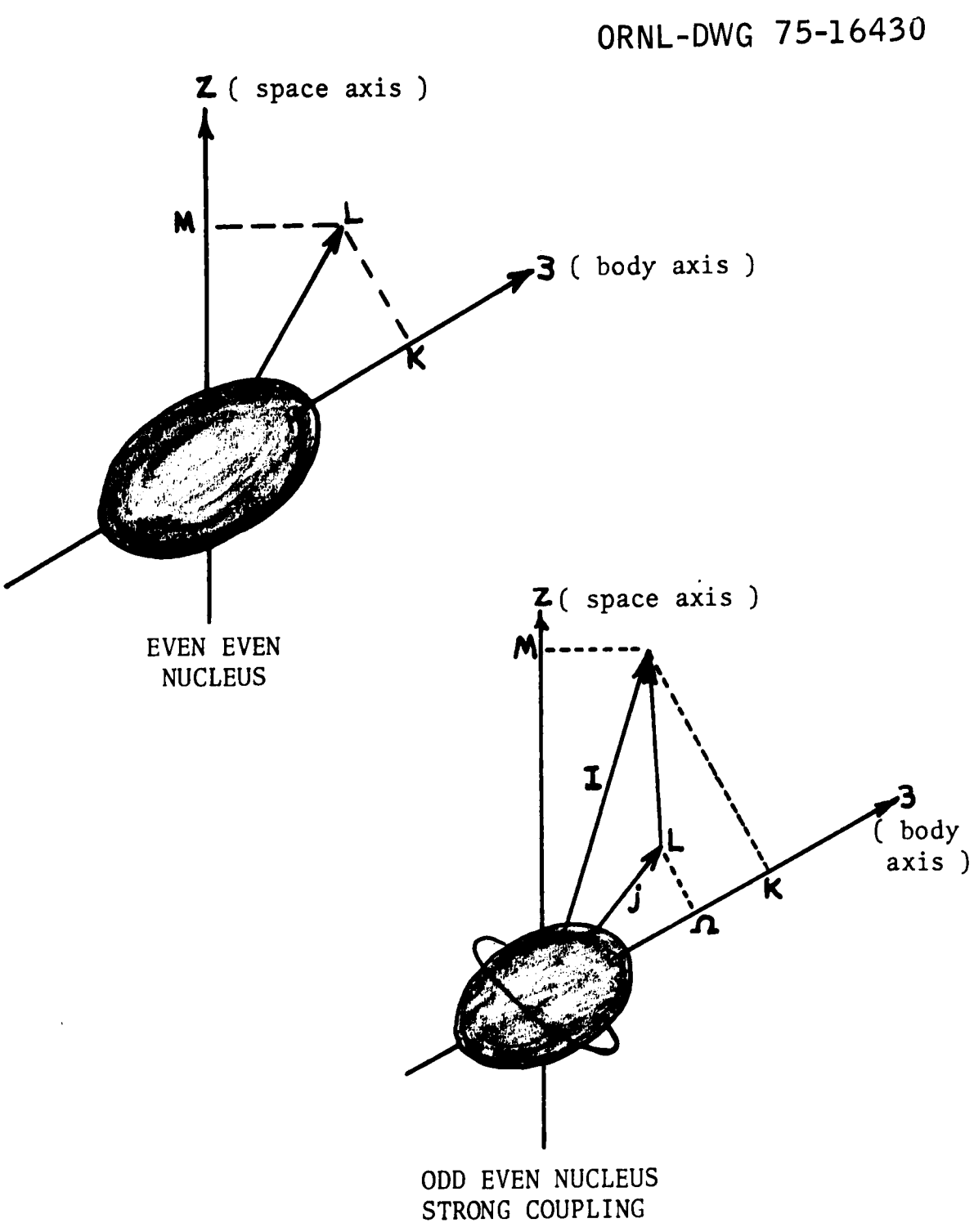


Figure 2-3. Angular momentum diagram for deformed nuclei.

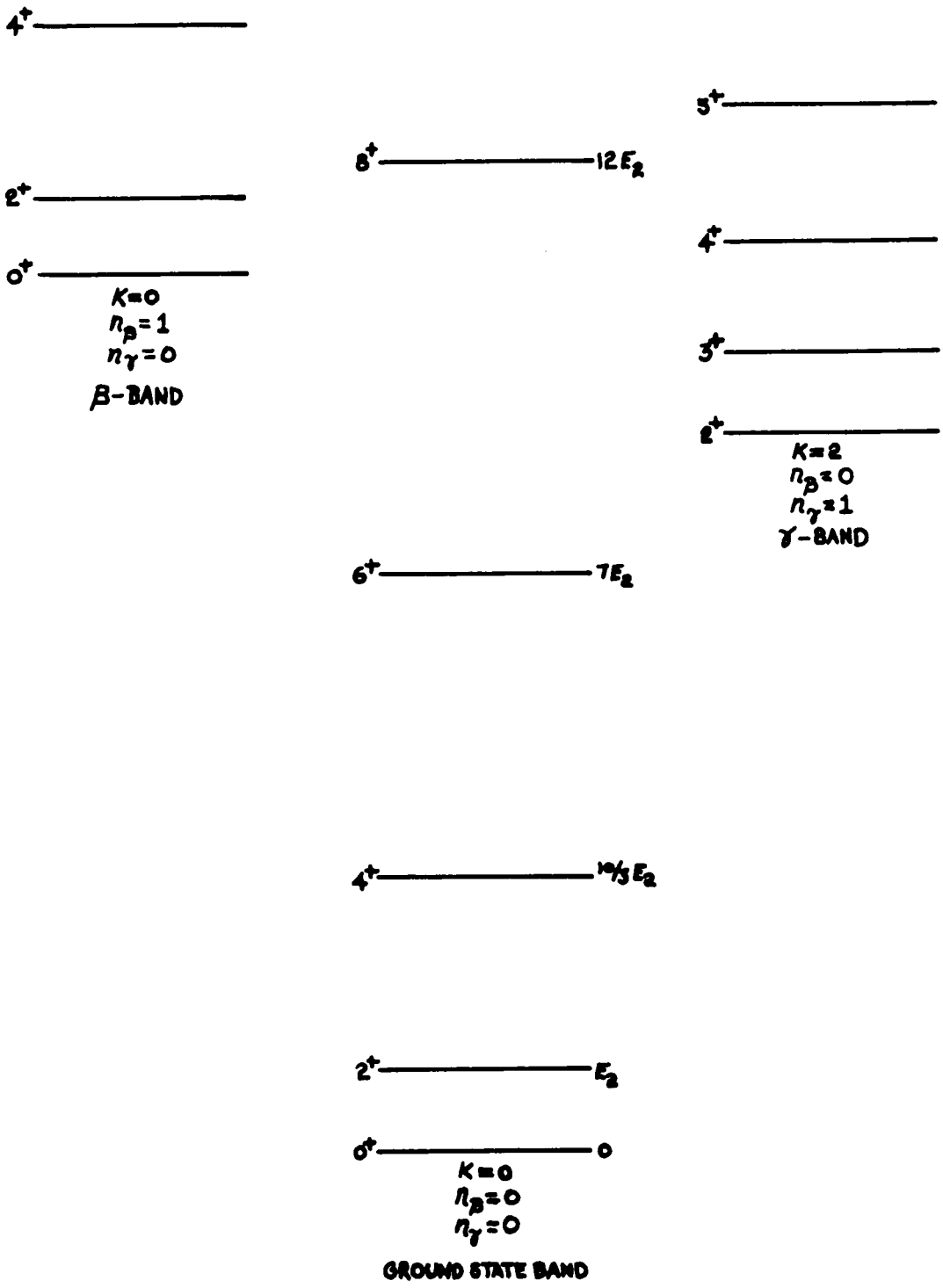


Figure 2-4. Energy levels for a deformed even-even nucleus with β- and γ-vibrational bands.

centrifugal stretching and band mixing resulting from more detailed considerations of the moment of inertia and rotation vibration interactions will not be considered here.

3. UNIFIED MODELS

The structure of the potential energy surface obviously influences the orbits of single particles. Since this surface is not in general spherically symmetric, and is a dynamic quantity, some sort of interaction between collective and single particle motions must be formulated. Such formulations are known as unified models.

The basic formulation of these types of models begin by regarding the nucleus as consisting of a collective core (either the nearest closed shell, or an adjacent even-even nucleus) and extra-core nucleons. The Hamiltonian for such a system may be written as

$$H = H_{coll} + H_{part} + H_{int} , \tag{2-20}$$

where H_{coll} is the collective Hamiltonian, H_{part} is the Hamiltonian for the extra particle(s), and H_{int} is used to account for the particle(s)-core interaction. Wave functions for such a system are expanded in direct products of collective and single particle eigenfunctions, that is

$$|\Psi\rangle = \sum_{i,k} C_{ik} |\Phi_{ik}\rangle = \sum_{i,k} C_{ik} |coll\rangle_i |part\rangle_k , \tag{2-21}$$

and these must satisfy the Schroedinger equation

$$H|\Psi\rangle = E|\Psi\rangle . \tag{2-22}$$

Using (2-21) and (2-22), multiplying by $\langle \text{coll}_j | \cdot \langle \text{part}_\ell | = \langle \phi_{j\ell} |$, and integrating gives

$$\sum_{i,k} C_{ik} \left[\langle \phi_{j\ell} | H | \phi_{ik} \rangle + E \delta_{ij} \delta_{k\ell} \right] = 0, \tag{2-23}$$

which implies

$$\left| \langle \phi_{j\ell} | H | \phi_{ik} \rangle - E \delta_{ij} \delta_{k\ell} \right| = 0. \tag{2-24}$$

Using (2-21) in (2-24) yields

$$\left| \langle \phi_{j\ell} | H_{int} | \phi_{ik} \rangle + \left(E_{coll,j} + E_{part,k} + E \right) \delta_{ij} \delta_{k\ell} \right| = 0. \tag{2-25}$$

Solution of this eigenvalue problem yields predicted energy levels and associated wave functions. From the latter, other nuclear properties can be calculated for comparison with experiment. Examination of Equation (2-25) discloses what input quantities are necessary. The $E_{coll,j}$ are obtained from the structure of the core. For single-particle coupling, the $E_{part,k}$ are obtained from transfer reactions, although in some formulations when data are incomplete, they may be treated as variables. This leaves the term $\langle \phi_{j\ell} | H_{int} | \phi_{ik} \rangle$. The form of H_{int} is[2,3,6]

$$H_{int} = k(r) \sum_{\mu} \alpha^*_{2\mu} Y_{2\mu} = -r \frac{dV_0}{dr} \sum_{\mu} \alpha^*_{2\mu} Y_{2\mu} . \tag{2-26}$$

The problem can now be solved by choosing appropriate wave functions with which to calculate $\langle \phi_{j\ell} | H_{int} | \phi_{ik} \rangle$. Evaluation of this matrix element

yields the strength of interaction. Sometimes this is treated as a variable in the calculations, otherwise either k(r) or V_o is specified. Obviously, the specification of the term of the core, and hence $|\phi_{ij}\rangle$, $E_{coll,j}$, $E_{part,k}$, is critical. In general, there are two situations, and these will be discussed next in terms of odd-even nuclei and a single particle coupled to a core. For both cases the adiabatic approximation (particle motion >> core motion) is utilized.

For odd-even nuclei near closed shells, one uses what is called the weak coupling model. In this region it is expected that

$$\langle \phi_{jl} | H | \phi_{ik} \rangle \ll E_{coll,j}, E_{part,k} \qquad (2\text{-}27)$$

(i.e., weak coupling strength) so the extra particle does not distort the core significantly. Accordingly, the core is taken to be a spherical vibrator and the single particle potential is assumed spherical. Further discussion is facilitated by considering the odd indium nuclei specifically.

Since the odd indium nuclei (Z=49) are one proton away from the closed shell at Z=50, they are expected to be prime candidates for the weak coupling model. With such a model, the prominent low energy structure (exlcuding possible single hole excited states) should be a quintet of states with $I^\pi = 5/2^+$, $7/2^+$, $9/2^+$, $11/2^+$, and $13/2^+$ resulting from the coupling of a $g_{9/2}$ hole to the first phonon vibration state (2_1^+) of the adjacent even tin nucleus (denoted $g_{9/2}^{-1} \otimes 2_1^+$). If the coupling strength is extremely weak, the sum of the $B_{ex}(E2,0^+\rightarrow 2^+)$ for the adjacent even tin nucleus, and the $B_d(E2)$ for each member of

the multiplet should be the same as the $B_d(E2,2^+\rightarrow 0^+)$ for the adjacent even tin nucleus. The center of gravity of the multiplet as given by

$$E_{CG} = \sum_{i=1}^{5} E_i(2J_i+1) / \sum_{i=1}^{5} (2J_i+1) \qquad (2\text{-}28)$$

should be the same as the energy of the 2_1^+ state in the even tin core. Furthermore, because of the nature of the multipole operator, there can be no M1 component in the ground-state transitions. If these conditions are not found, modifications in the theory, such as increasing the coupling strength, must be made.

Similar conclusions can be made for states resulting from the coupling of a hole to the one octupole phonon and two quadrupole phonon vibrational states in the adjacent even tin core.

The opposite situation to weak coupling is strong coupling. Here, the interaction between the particle(s) and core is so strong that the nucleus assumes a permanent deformation. It is assumed that the motion of the odd nucleon in the potential formed by the core and seen from the reference frame fixed in the nucleus is identical with that of a nucleon moving in a similar, but spatially fixed potential. This assumption affects the commutators of angular momentum operators. Let $\vec{L}$ be the angular momentum of the core and $\vec{j}$ be the angular momentum of the extra core nucleon. Neither of these will be constants of motion, but the total angular momentum $\vec{I}$ defined by $\vec{I} = \vec{L} + \vec{j}$ will be. The strong coupling assumption implies that in the body fixed frame

$$[I_1, I_2] = -i I_3 \text{ , cyclically} \qquad (2\text{-}29)$$

$$[j_1, j_2] = -i j_3 \text{ , cyclically .} \qquad (2\text{-}30)$$

The vector diagram of the angular momentum vectors is shown in Figure 2-3, page 13.

For general deformations, only I^2 and I_z will be constants of motion, but if there is axial symmetry, K and Ω will also be good quantum numbers. Now, in the total Hamiltonian for the system, H_{coll} (and associated eigenfunctions) must be given by the appropriate collective Hamiltonian for a deformed nucleus. Also, the potential that the extra particle sees is no longer spherical, but is that of a deformed core. The calculation of orbitals for a single particle in a deformed well (and hence energy levels and eigenfunctions) has been performed in the classic paper of Nilsson.[7] In his paper, Nilsson used a three dimensional anharmonic oscillator well and spin-orbit coupling (the equipotential surfaces being ellipsoids) to calculate the relative position of the orbitals as a function of deformation. Finally, there is a rotation-particle coupling term in the total Hamiltonian which, because it is of the form $\vec{\omega} \cdot \vec{j}$, is also called a Coriolis term. Generally speaking it possesses only off diagonal terms (for the H_{coll} and H_{sp} eigenfunctions) unless $K = \Omega = 1/2$.

For a particle tightly bound to a core, the particle spacings are large compared to rotational level spacings, so for an axially symmetric nucleus

$$E_{I,K} = (\hbar^2/2\mathcal{I})[I(I+1) - 2K^2] + E_{\Omega}, \qquad (2\text{-}31)$$

where E_{Ω} is the single-particle energy and the sequence of rotational bands is $I = K = \Omega$, K+1, K+2, etc...

If $K = \Omega = 1/2$, the Coriolis term must be included so the energy level spacing goes as

$$E_I = E_o + (\hbar^2/2\mathcal{I})[I(I+1) + a(-1)^{I+1/2}(I+1/2)], \qquad (2\text{-}34)$$

where a is called the decoupling parameter and is a measure of the rotation-particle coupling strength.

CHAPTER 3

THE COULOMB EXCITATION AND (HI,xn) REACTIONS

1. THE COULOMB EXCITATION REACTION

When two nuclei approach each other, it may be possible for their electromagnetic fields to interact and produce excitation of one or both of them. Coulomb excitation is this electromagnetic excitation of a nucleus, and is most practical when the two nuclei come close enough together so the probability of excitation is significant, but not so close that short range nuclear forces can have an effect. Because cross sections for this process can be directly related to electromagnetic nuclear properties, and because nuclear levels can be directly populated, Coulomb excitation has proved to be an extremely valuable research tool.

The theory of this reaction has been discussed many times. Perhaps the most complete article is the classic and amazingly enduring paper by Alder et al.[15] The discussion here will be a synopsis of this article emphasizing the basic concepts and the derivation of the cross section. The treatment follows that of Milner[16] and Sayer.[17] Basically it uses the classical description of a projectile moving in a hyperbolic orbit exciting the target via a time dependent electromagnetic field.

A useful parameter characterizing the Coulomb excitation reaction is the dimensionless quantity η defined by

$$\eta = Z_1 Z_2 e^2 / \hbar v . \qquad (3\text{-}1)$$

where Z_1e and Z_2e are the nuclear charges of the projectile and target respectively, and v is the projectile velocity. For a classical description to be valid, the projectile must not enter the nucleus (i.e. its energy must be below the nuclear Coulomb barrier). Also, the energy given off to excite the target nucleus must be small compared to the projectile energy in order that the projectile's orbit be described by the classic hyperbolic path. The quantity η can be rewritten

$$\eta = a/\lambda \,, \tag{3-2}$$

where

$$a = (Z_1 Z_2 e^2)/(M_o v^2) \,, \tag{3-3}$$

and where M_o is the reduced mass.

Noting that 2a is the distance of closest approach in a head on collision, and that λ is the deBroglie wavelength of the projectile, one sees that $\eta >> 1$ describes a classical system. This seems plausible because the wavelength of the projectile is short compared to the characteristic distances of the collision, and large a implies the projectile energy is below the Coulomb barrier.

Assuming this classical description, one can write the differential cross section

$$d\sigma = P_{i\to f}\, d\sigma_R \,, \tag{3-4}$$

where $d\sigma_R$ is the Rutherford scattering cross section and $P_{i \to f}$ is the probability of exciting the target nucleus from state i to state f. This probability can be expressed in terms of the amplitude b_{if} for a transition from the state i to state f. When considering excitation of a given energy level irrespective of the spin orientation of the initial and final states, an average over all initial magnetic substates M_i and final magnetic substates M_f must be taken so the probability $P_{i \to f}$ is written as

$$P_{i\to f} = (2I_i+1) \sum_{M_i M_f} |b_{if}|^2 \,. \tag{3-5}$$

In situations where $P_{i \to f} << 1$, first order perturbation theory is expected to be accurate, so that the expression for b_{if} becomes

$$b_{if} = \frac{1}{i\hbar} \int_{-\infty}^{+\infty} \langle f | \mathcal{H}(t) | i \rangle e^{i\omega t} dt \,, \tag{3-6}$$

where $\mathcal{H}(t)$ is the interaction energy, and $\omega = \Delta E/h = (E_f - E_i)/h$ is the frequency associated with the excitation energy ΔE.

Since for most projectiles $(v/c)^2 << 1$, magnetic excitations are relatively unimportant. Thus the interaction energy $\mathcal{H}(t)$ is the electric Coulomb interaction, and is expressed as

$$\mathcal{H}(t) = \mathcal{H}_E(t) = \int \rho_N(\vec{r})\, \phi(\vec{r},t)\, d\tau, \tag{3-7}$$

where $\rho_N(\vec{r})$ is the nuclear charge density operator and ϕ is the potential at a point $\vec{r}$ due to the projectile. The potential ϕ is given by

$$\phi(\vec{r},t) = \frac{Z_1 e}{|\vec{r} - \vec{r}_p(t)|} - \frac{Z_1 e}{r_p(t)}, \tag{3-8}$$

and the projectile is assumed to be a point charge whose position is specified by $\vec{r}_p(t)$, measured from the nuclear center of mass. Next, the potential $\phi(\vec{r},t)$ is written in the usual multipole expansion, and $\rho_N(\vec{r})$ is expressed in terms of proton point charges. Using these expressions in Equation (3-7) and substituting back, the differential cross section for a multipole of order Eλ becomes

$$d\sigma_{E\lambda} = \left(\frac{Z_1 e}{\hbar v}\right)^2 a^{-2\lambda-2}\, B(E\lambda)\, df_{E\lambda}(\theta,\xi). \tag{3-9}$$

Here B(Eλ) represents the reduced transition probability for an electric transition of multipole order λ, i.e.

$$B(E\lambda, J_i \to J_f) \equiv \sum_{\mu, m_f} |\langle J_i\, m_i | \mathcal{M}(E\lambda;\mu) | J_f\, m_f \rangle|^2$$

$$= (2J_i+1)^{-1} |\langle J_i \| \mathcal{M}(E\lambda) \| J_f \rangle|^2. \tag{3-10}$$

The quantity $df_{E\lambda}(\theta,\xi)$ (differential excitation function) is given by Equation II A.29 of Alder et al.,[15] where the dimensionless quantity ξ is defined by

$$\xi = a\,\Delta E/\hbar v = \frac{Z_1 Z_2 e^2}{\hbar v}\,\frac{\Delta E}{2E}\,, \tag{3-11}$$

in which E and ΔE represent the energies of the incident projectile and the nuclear excitation energy respectively. The quantity ξ is the ratio of collision time to nuclear period, and must be small if the probability for Coulomb excitation is to be optimum (sudden shock condition).

To more accurately account for the energy exchange in the collision, the symmetrized parameters

$$a = Z_1 Z_2 e^2 / M_0 v_i v_f\,, \tag{3-12}$$

and

$$\xi = \frac{Z_1 Z_2 e^2}{\hbar}\left(\frac{1}{v_i} - \frac{1}{v_f}\right) \tag{3-13}$$

are used. The resulting total cross section is then

$$\sigma_{E2} = \left(\frac{Z_1 e}{\hbar v_i}\right)^2 a^{-2}\, B(E2, I_i \rightarrow I_f)\, f_{E2}(\eta,\xi)\,, \tag{3-14}$$

where the "total excitation functions" $f_{E\lambda}(\eta,\xi)$ have been evaluated quantum mechanically to be used in situations for which $\eta \leq 8$. Evaluation of numerical factors in Equation (3-14) yields,

$$\sigma_{E2}(cm^2) = 4.782 \times 10^{24} \frac{A_1}{Z_2^2}\left(\frac{A_2}{A_1+A_2}\right)^2 (E-\Delta E')\frac{B(E2)}{e^2} f_{E2}(\eta,\xi), \quad (3\text{-}15)$$

where E is the energy of the projectile in the laboratory system in MeV, A_1 and A_2 are the masses of the projectile and target in amu, Z_1 and Z_2 are the atomic numbers of the projectile and target, $\Delta E' = (1 + A_1/A_2)\Delta E$ and ΔE is the excitation energy of the nucleus in MeV. The quantity $B(E2)/e^2$ is in units of cm^4.

If the probability for excitation becomes higher (as might be the case for heavy ion projectiles at sufficiently high energy) second order effects may become important. This also has been discussed by Alder et al.,[15] but is not pertinent to this work.

Finally, the perturbation theory approach may break down altogether. If, however, the assumption of classical orbits is used (thought to be well satisfied), the prescription of Winther and de Boer[18] may be used. Again, this is not pertinent to this work.

2. THE (HI,xn) REACTION

The (HI,xn) reaction refers to the process expressed as

$$^{A_1}_{Z_1}HI + ^{A_2}_{Z_2}T \rightarrow ^{A_1+A_2}_{Z_1+Z_2}CN^* \rightarrow ^{A_1+A_2-x}_{Z_1+Z_2}R + xn, \quad (3\text{-}15)$$

in which it is desired to study the nucleus R. This nucleus is formed in an excited state by the process indicated in Equation (3-15), which in words goes as follows. Bombard a target nucleus T with a heavy ion projectile HI in a manner causing the two nuclei to fuse and form a highly excited compound nucleus CN. The compound nucleus CN then loses most of its energy by emitting x number of neutrons n (provided the compound nucleus is not too near the proton drip line) leaving the somewhat excited nucleus R. The excited nucleus R then decays by γ-ray emission to its ground state. In this work it is the measurement of these γ rays which provides the structural information about R. The rest of this section will give a general overview of the details of the whole process following the treatments of Newton[19] and Smith.[20] The extraction of specific properties will be deferred to Section 3, but an idea of the type of structure seen in these reactions can be obtained from the following discussion.

Compound Nucleus Formation

The first thing to consider is the competiveness of the compound nuclear reaction with other reactions. This, quite naturally, depends upon the projectile energy. For bombarding energies below the nuclear Coulomb barrier, the nuclei are never close enough to fuse, so elastic scattering and Coulomb excitation are the dominant mechanisms. At somewhat higher bombarding energies, only the tails of the nuclear wavefunctions overlap. Complete fusion is improbable, but there may be several nucleons transferred or nuclear inelastic scattering may take place. For energies high enough that there is complete overlap

of nuclear wavefunctions, complete fusion as well as all of the previously mentioned processes may take place. Fortunately, except in special cases, the compound nucleus reaction is the dominent mechanism having a cross section on the order of one barn.

The excitation energy of the compound nucleus (E_{CN}) can be simply calculated. Conservation of energy yields

$$T_{HI} - B_{HI} - B_T + E_{HI} + E_T = T_{CN} - B_{CN} + E_{CN}, \qquad (3\text{-}16)$$

where the subscripts stand for the quantities in Equation (3-15), T represents the kinetic energy, B is the binding energy, and E is the excitation energy. Normally the target and projectile are in their ground states ($E_{HI} = 0 = E_T$) and in the center of mass system $T_{CN} = 0$, so Equation (3-16) becomes

$$E_{CN} = T_{HI} + (B_{CN} - B_{HI} - B_T) = T_{HI} + Q, \qquad (3\text{-}17)$$

where $Q = B_{CN} - B_{HI} - B_T$ is the Q value for compound nucleus formation.

Decay of the Compound Nucleus

When it is formed, the compound nucleus is in a highly excited state. If the time from absorption of the projectile to emission of a particle is long compared to the time required for a nucleon to cross the nucleus ($\sim 10^{-22}$ sec), then the compound nucleus samples all levels available to it and reaches statistical equilibrium. Because it is thought that statistical equilibrium is reached, and because the

number of final states and emitted particles is very large, a statistical description is usually used to describe the decay process. The results of this type of description will be discussed next.

There are several ways for the compound nucleus to deexcite, such as emission of γ rays, emission of charged particles, and emission of neutrons. Deferring for the moment γ-ray emission, the probability of a compound nucleus decaying to another nucleus by particle emission is roughly proportional to the product of the transmission coefficient for that particle times the density of states in the final nucleus. The shape of the spectrum of emitted particles (relative number versus energy) is roughly Maxwellian, going to zero at low energies because of the transmission coefficient, and going to zero at high energies because of the density of states function. The maximum energy attainable for the emitted particle is $E_{max} = E_{CN} - B_P$ where B_P is the binding energy of the particle emitted. The spectral shape for charged particles is roughly the same as for neutrons, but must be displaced up in energy becasue of the Coulomb barrier. It is because of this barrier that neutron emission is dominant over charged particle emission despite the fact that the energy available for charged particle emission can be greater than that for neutron emission. This analysis must be modified somewhat when the compound nucleus is substantially neutron deficient. In this region, the binding energy of protons and other charged particles changes so that charged particle emission is competitive or even dominent despite the Coulomb barrier.

If the compound nucleus formed is near enough to the valley of stability so that neutron emission is the dominant mechanism, then how clearly is a residual nucleus formed? That is, if we wish to observe a (HI,3n) reaction, how much of the (HI,2n) and (HI,4n) components are present? In practice, these reactions can be very selective if the projectile energy is chosen properly. The reasoning is as follows. The first neutron emitted leaves the residual nucleus at an energy $E_{A-1} = E_{CN} - B_A(n_1) - E_{n_1}$, where $B_A(n_1)$ is the binding energy of the first neutron emitted and E_{n_1} is its energy which follows a distribution function. After emitting three neutrons, the residual nucleus has an energy $E_{A-3} = E_{CN} - B_A(n_1) - B_{A-1}(n_2) - B_{A-2}(n_3) - En_1 - En_2 - En_3$. The first four terms are fixed by the reaction and the last three are variable, but governed by the distribution function. Roughly speaking $E_n = 2 \pm 1$ MeV for each neutron emitted, and if the compound nucleus is ^{116}In, $B_A(n_1) + B_{A-1}(n_2) + B_{A-2}(n_3) \tilde{=} 23$ MeV. Thus, $E(^{113}\text{In}) \tilde{=} E_{CN} - (29 \pm 3)$ MeV. If $E_{CN} \tilde{=} 32$ MeV, then the emission of another neutron is improbable because of the binding energy ($\sim$ 8 MeV) and $E(^{114}\text{In}) \tilde{=} 12 \pm 2$ MeV so it would likely not be competitive either.

A schematic diagram illustrating the formation and decay of a compound nuclear system is given in Figure 3-1.

Angular Momentum Effects

A principal feature of heavy ion induced reactions is that they bring in a large amount of angular momentum to the compound nucleus system. This can be demonstrated in a simple calculation. The angular

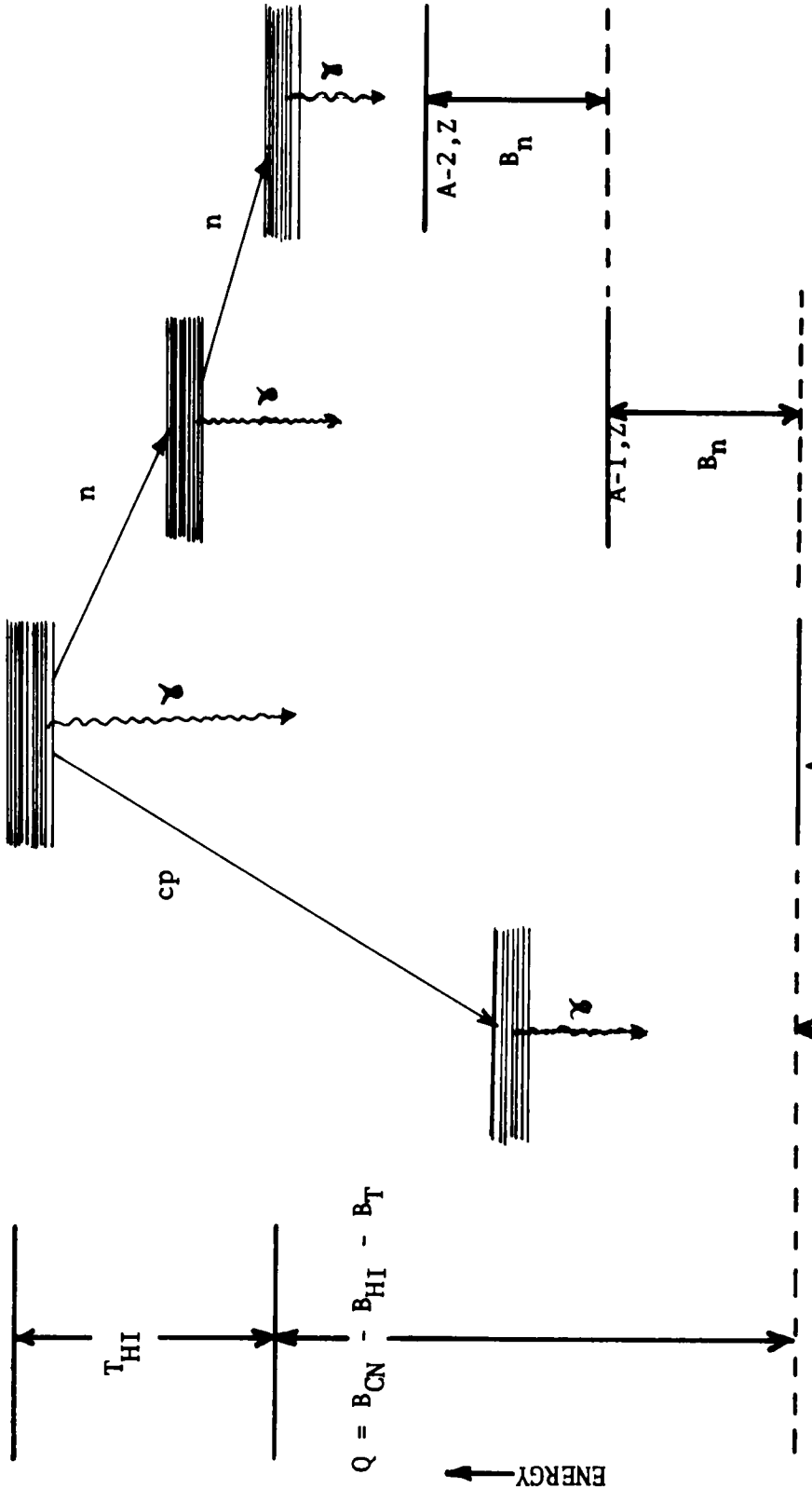


Figure 3-1. Schematic diagram illustrating the formation and subsequent decay of a compound nuclear system.

momentum $\vec{\ell}$ is defined by

$$\vec{\ell} = \vec{r} \times \vec{p} \quad . \tag{3-18}$$

The maximum value for ℓ occurs when $\vec{r}$ is perpendicular to $\vec{p}$. Lettering $r = R_1 + R_2$, where R_1 R_2 are the nuclear radii (given by $R = r_o A^{1/3} = 1.2 \times 10^{-13} A^{1/3}$ cm) of the projectile and target respectively, and recalling $p = (2mT)^{1/2}$, the maximum value for ℓ (in units of h) can be estimated from

$$\ell_{max} \cong (2mT)^{1/2} (A_1^{1/3} + A_2^{1/3}) (1.2 \times 10^{-13} cm)/\hbar \quad . \tag{3-19}$$

For a 24 MeV ^{6}Li projectile and a ^{110}Pd target, $\ell_{max} \cong 22$.

Since the compound nucleus is formed with such high angular momentum, the effect on its decay must be considered. A detailed study is complicated (see e.g. references given by Newton[19]) but the general features can be simply understood. Consider a plot of nuclear energy levels and their associated angular momentum. For each angular momenta, there is a minimum energy state. The locus of these states is called the yrast line and is displayed graphically in Figure 3-2. On or above the line are allowed nuclear states, and below the line no states are allowed. When the compound nucleus is formed, its initial state can be represented by a point on this diagram. Assuming that the yrast lines of the parent and residual nuclei are the same, the decay of five points will be discussed in a manner similar to Smith.[20] Two general features must be kept in mind. First, the nucleus will

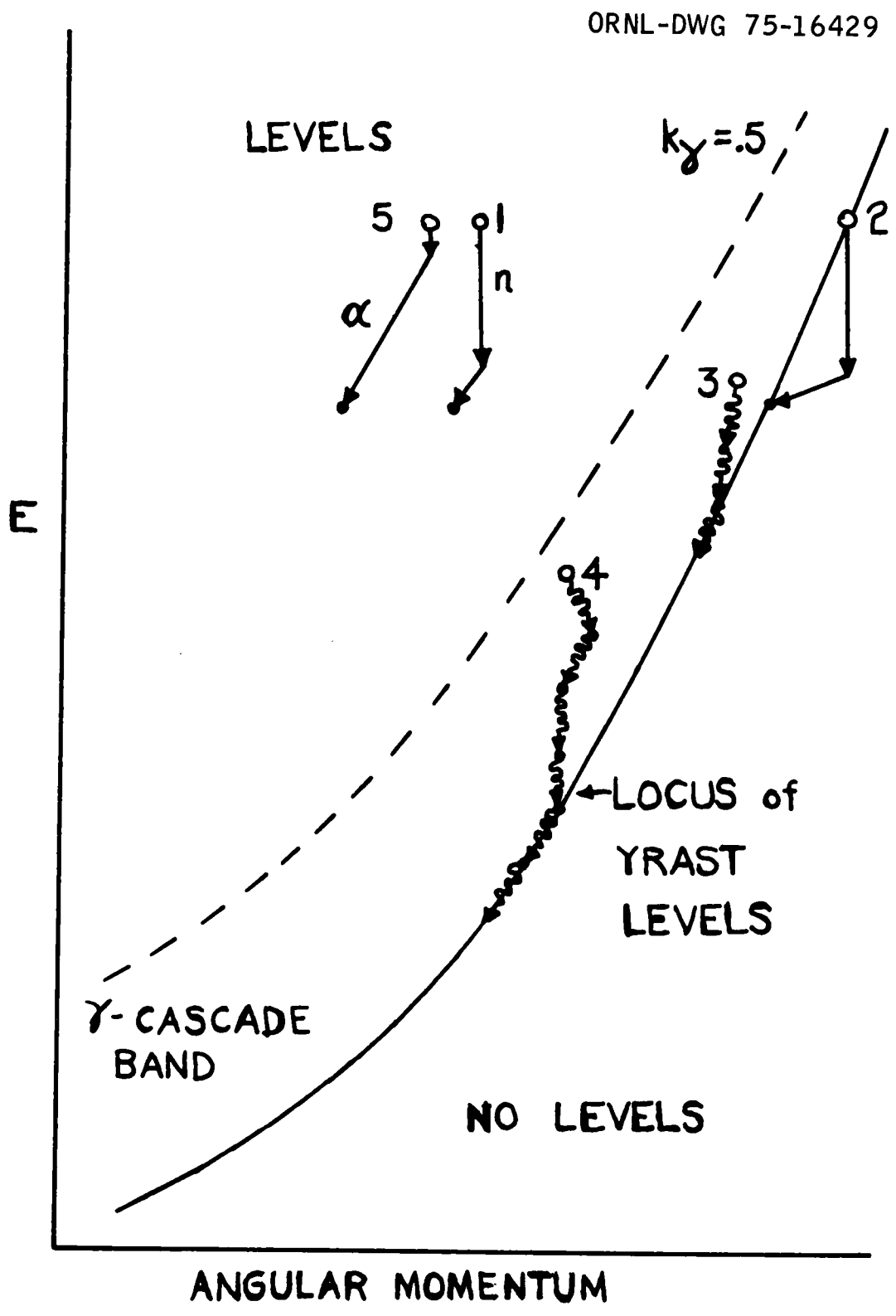


Figure 3-2. Diagram illustrating possible de-excitation modes of highly excited nuclei.

prefer to decay to an yrast level whenever possible, and once it has achieved an yrast level, it will decay from one yrast level to another. Secondly, in addition to the Coulomb barrier, there is an angular momentum barrier to consider. This is a consequence of the solution of the time independent Schroedinger equation for a spherically symmetric potential. With the usual separation of variables technique and spherical coordinates, the resulting equation is

$$-\frac{\hbar^2}{2m}\frac{d^2\rho}{dr^2} + \left[V(r) + \frac{\ell(\ell+1)}{2mr^2}\right]\rho = E\rho \ . \qquad (3\text{-}20)$$

Here $\rho(r) = rR(r)$, where $R(r)$ is the radial part of the total wavefunction Ψ ($\Psi \equiv R(r)T(\theta)F(\phi)$), and the $\ell(\ell + 1)/2mr^2$ term is the added potential.

Referring to Figure 3-2, the amount of energy lost by particle emission is the sum of the kinetic energy of the particle and its separation energy. In the diagram the vertical arrow represents the separation energy while the vertical component of the slashed arrow represents the kinetic energy. The horizontal component of the slashed arrow represents the angular momentum carried away. Points 1 and 5 represent states with high energy and angular momentum far above the yrast line. Although the angular momentum barrier is lower for α particle emission than for n emission, this is a small effect compared to the Coulomb barrier, and n emission tends to dominate for points like points 1 and 5. For points on or very near the yrast line like point 2, γ-ray emission dominates. If a neutron is emitted from

point 2, it must (as is indicated in the diagram) have a large angular momentum to get back to allowed levels. This is strongly inhibited by the angular momentum barrier. For this reason, the dashed line $K_\gamma = 0.5$ which represents the locus of points where the probability of γ-ray emission is 50% is drawn parallel to the yrast line and separated by a distance equal to the neutron binding energy. States between these two lines decay mostly by γ ray emission because of the angular momentum barrier for neutrons. Finally, according to Grover and Gilat,[21] states like point 4 (well above yrast curve) decay by cascades of dipole γ rays while states such as point 3 (near yrast curve) decay predominately by quadrupole γ ray emission.

3. THE EXTRACTION OF NUCLEAR PROPERTIES

Reduced Transition Probabilities

One of the most useful aspects of Coulomb excitation work is the ability to extract reduced transition probabilities. The basis for this is as follows. Consider a beam of charged particles impinging upon a thick target, where a thick target is one in which the incident beam is stopped. The number of excitations in target element thickness dx is $N\sigma(x)dx$ where x is the distance the projectile has penetrated into the target, N is the number of target nuclei per cm^3, and $\sigma(x)$ is the cross section for excitation. N is given by

$$N = \rho A_0 / A_N \qquad (3\text{-}21)$$

where ρ is the mass density of the target, A_N is the atomic weight of the normal target element and A_o is Avogadros' number, so if there are N_p total number of incident projectiles, the total number of nuclear excitations (N_{ex}) is

$$N_{ex} = (N_p)(\rho A_o/A_N) \int_o^x \sigma(x)\, dx \quad . \tag{3-22}$$

The stopping power of a projectile in a target is defined by

$$S(E) = -\frac{1}{\rho}\frac{dE}{dx} \quad , \tag{3-23}$$

so if a change of variable is made in (3-22), the result is

$$N_{ex} = (N_p)(A_o/A_N) \int_E^o \frac{\sigma(E)\, dE}{S(E)} \quad . \tag{3-24}$$

With the expression for the Coulomb excitation cross section, Equation (3-15), placed in Equation (3-24), evaluating numerical quantities and rearranging gives

$$\frac{B(E2, I_i \to I_f)}{e^2} = 5.556 \times 10^{-27} \frac{A_N Z_2^2}{3 A_1 K^2} \frac{I(\text{exc}/\mu\text{c})}{\int \frac{S_{E2}(\eta,\xi)(E-\Delta E')\, dE}{S(E)}} \tag{3-25}$$

Here $K = A_2/A_1 + A_2)$, I(exc/μC) is the number of excitations per microcoulomb of incident charge, $\mathfrak{Z}$ is the charge state of the projectile, and S(E) is in units of MeV·cm^2. The B(E2) value then comes out in units of $e^2 \cdot cm^4$.

In practice the procedure is as follows. Evaluate the thick target integral $[\int f_{E2}(\eta, \ )(E-\Delta E')dE/S(E)]$ for the nuclear levels and range of projectile energies of interest. To obtain the yield, determine the absolute number of decays from the level of interest and subtract from it the absolute number of transitions feeding this level. Divide this number by the total incident charge on the target (obtained from the live current integrator reading) and the appropriate thick target integral. The $B(E2)/e^2$ value is then obtained by multiplying this factor by the quantity $5.556 \times 10^{-59} A_N Z_2^2 / A_1 K^2$.

Angular Distributions

The angular distribution of a γ ray refers to the directional correlation of a transition from a nuclear level with the process that populated it. This process may be Coulomb excitation, radioactive decay, a (HI,xn) reaction, or a cascade from a higher level. The possibilities are illustrated in Figure (3-3). This directional correlation between the observed γ ray and the preceding process may be expressed as

$$W(\theta) = \sum_{k\,\text{even}} A_k^x A_k^{\gamma_1} P_k(\cos\theta), \qquad (3\text{-}26)$$

where the A_k^x (x refers to charged particle or γ) depend upon the spins, multipolarities, and substate populations of the levels involved.

For Coulomb excitation, the A_k^x can be calculated from theory. For thick targets the resultant angular distribution function is

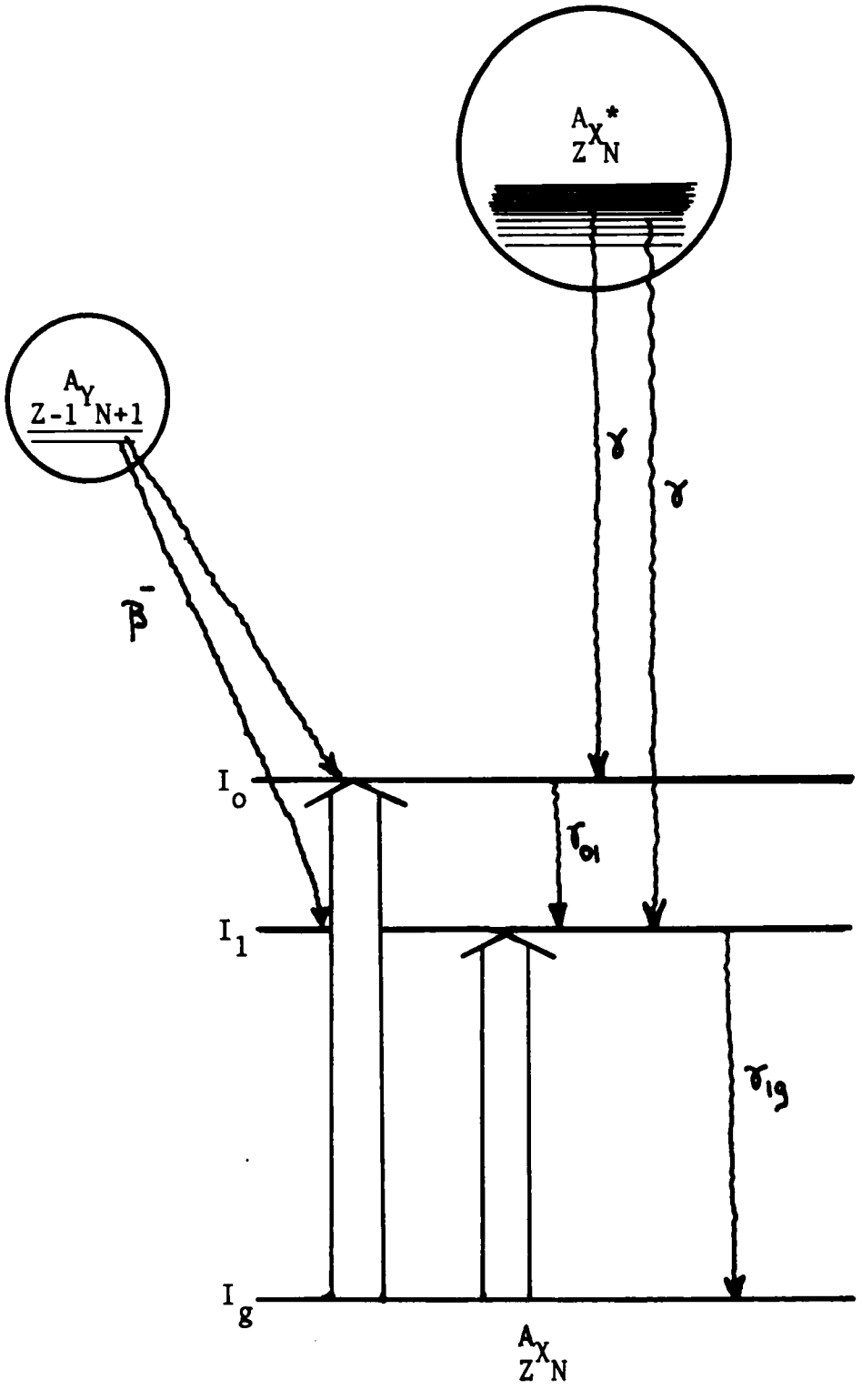


Figure 3-3. Energy level diagram illustrating various mechanisms for populating a level.

$$W(\theta) = 1 + a_2^t g_2 A_2 P_2(\cos\theta) + a_4^t g_4 A_4 P_4(\cos\theta) \,, \qquad (3\text{-}27)$$

where the $P_2(\cos\theta)$, $P_4(\cos\theta)$ are the Legendre polynomials, the g_2, g_4 are solid angle geometrical correction factors, the a_2^t, a_4^t are the particle parameters (a_2^t, a_4^t) of Alder et al.[15] averaged over a thick target, and the A_2, A_4 are the angular distribution coefficients. These coefficients are a function of the spin sequence and mixing ratio for the observed γ-ray transition, and are given by

$$A_2 = F_2(22 j_i j_e) \frac{[F_2(11 j_f j_e) + 2\delta F_2(12 j_f j_e) + \delta^2 F_2(22 j_f j_e)]}{1+\delta^2} \qquad (3\text{-}28)$$

and

$$A_4 = F_4(22 j_i j_e) \frac{\delta^2 F_4(22 j_f j_e)}{1+\delta^2} \,, \qquad (3\text{-}29)$$

where

$$\delta^2 \equiv \langle j_i \| L_1+1 \| j \rangle^2 / \langle j_i \| L_1 \| j \rangle^2 \qquad (3\text{-}30)$$

is the ratio of 2^{L_1+1} pole to 2^{L_1} pole intensity (usually E2 to M1) and the F_k are the standard F coefficients which can be expressed in terms of Clebsch-Gordan and 6j coefficients. The quantities j_i, j_e and j_f are the spins of the intial, excited and final states respectively.

The procedure for data analysis is as follows. Experimentally determine the anisotropy $R \equiv W(0°)/W(90°)$, and its associated error.

Because a_4^t is usually small, the second term in Equation (3-27) may be omitted. Thus, knowing a_2^+ and g_2, the experimental A_2 and associated error may be determined. This experimental A_2 can now be compared to the theoretical expression Equation (3-28). The overlap between theoretical and experimental values yields the experimentally allowed spin sequences and mixing ratios.

The angular distribution data from a (HI,xn) experiment is usually analyzed according to the procedure given by Yamazaki.[22] This has been discussed further by der Mateosian and Sunyar[23] and goes as follows.

According to Diamond et al.,[24] nuclei produced in heavy ion reactions are well-aligned relative to the beam axis. If the alignment is complete (m = 0 substates only) the angular distribution for a transition from a state $I = I_i$ to a state $I = I_f$ may be written

$$W(\Theta) = 1 + A_2^{max} P_2(\cos\Theta) + A_4^{max} P_4(\cos\Theta) , \tag{3-31}$$

where

$$A_k^{max}(I_i L_1 L_2 I_f) = \frac{1}{1+\delta^2}\left\{ f_k(I_f L_1 L_1 I_i) + 2\delta f_k(I_f L_1 L_2 I_i) \right.$$

$$\left. + \delta^2 f_k(I_f L_2 L_2 I_i) \right\} , \tag{3-32}$$

in which

$$f_k(I_f L_1 L_2 I_i) \equiv B_k(I_i) F_k(I_f L_1 L_2 I_i) . \tag{3-33}$$

In this last expression the F coefficients are defined as before and B_k is the orientation parameter for complete alignment of the initial spin state given by

$$B_k(J) = \begin{cases} (2J+1)^{1/2}(-1)^J (J0J0|k0) & \text{integral spin} \\ (2J+1)^{1/2}(-1)^{J-1/2}(J\tfrac{1}{2}J\tfrac{1}{2}|k0) & \text{half integral spin} \end{cases} \quad (3\text{-}34)$$

where the terms (JkLM|no) are Clebsch-Gordon coefficients.

In realistic cases where the alignment is partial, Equation (3-31) becomes

$$W(\theta) = 1 + \alpha_2 A_2^{max} P_2(\cos\theta) + \alpha_4 A_4^{max} P_4(\cos\theta), \quad (3\text{-}35)$$

where the α_k are the attenuation coefficients which are functions of the initial spin and m substate population. They are given by

$$\alpha_k(J_i) \equiv \rho_k(J_i) / B_k(J_i), \quad (3\text{-}36)$$

where

$$\rho_k(J) = (2J+1)^{1/2} \sum_m (-1)^{J-m} (JmJ-m|k0) P_m(J), \quad (3\text{-}37)$$

in which the $P_m(J)$ are population parameters for the various substates m of J. If these population parameters can be represented by a Gaussion distribution function of the form

$$P_m(J) = EXP\left(\frac{-m^2}{2\sigma^2}\right) \Big/ \sum_{m'=-J}^{+J} EXP\left(\frac{-m'^2}{2\sigma^2}\right), \tag{3-38}$$

the attenuation coefficients α_k can be expressed in terms of I and σ/J where σ is a measure of the width of the distribution ($\sigma = 0$ corresponding to complete alignment).

Now, experimentally, one determines the quantities A_2^{exp}, A_4^{exp} by fitting the data to

$$W(\theta) = 1 + g_2 A_2^{exp} P_2(\cos\theta) + g_4 A_4^{exp} P_4(\cos\theta). \tag{3-39}$$

Then quantities α_2, α_4 can be determined experimentally from

$$\alpha_k = (g_k A_k^{exp}) / A_k^{max}. \tag{3-40}$$

For each α_2 and α_4 a value of σ/J may be obtained. For a given transition, the value of σ/J obtained from α_2 should be consistent with that obtained for α_4 if the data is consistent. Another criteria is that $\alpha_K(I_f)$ can be calculated from $\alpha_k(I_i)$ if there is no side feeding (see Yamazaki[22] for details).

The above criteria work in the ideal case. For less ideal data the A_4^{exp} determination is pretty crude. The first criteria is then a reasonable α_2 such as $0.5 \leq \alpha_2 \leq 1.0$.

As a general rule of thumb, a negative A_2^{exp} and positive or small A_4^{exp} imply $\Delta\ell = 1$, where $\Delta\ell = |I_i - I_f|$ and a large positive A_2^{exp} and small negative A_4^{exp} imply $\Delta\ell = 2$. Usually some δ can be chosen so that the $\Delta\ell = 0$ assignment cannot be eliminated. If A_4^{exp} is positive, then the assignment $\Delta\ell = 1$ can be made uniquely. For $A_4^{exp} = 0$ the choice is $\Delta\ell = 0$ or $\Delta\ell = 1$ and for A_4^{exp} negative, the choice is $\Delta\ell = 0$ or $\Delta\ell = 2$.

Ratio of Directional Correlation Measurements from Oriented Nuclei

As a supplement to γ-ray angular distribution measurements, triple correlation measurements are sometimes performed. Such measurements can distinguish between values of the spin and/or mixing ratio allowed by the angular distribution data, but they are time consuming. Fortunately, a method using the limited correlation data obtained in a standard coincidence measurement can often serve just as well. This method is the measurement of the ratio of directional correlations emitted from oriented nuclei (DCO-ratio) as first proposed by Krane et al.[25] Its applicability to heavy ion induced reactions, where the beam axis provides the orientation axis, has been discussed in a number of articles. The treatment here will follow that of Graw et al.[26] and Kim et al.[27]

The measurement of the coincidence rates $W(X(\gamma_1),Y(\gamma_2))$ of two γ rays γ_1 and γ_2 that are emitted from an oriented ensemble of two nuclei and observed by two detectors X and Y forms the basis of the DCO-ratio method. If the role of the two detectors is reversed and the rate $W(X(\gamma_2),Y(\gamma_2))$ is also measured, the ratio $R(A,B) \equiv W(X(\gamma_1),Y(\gamma_2))/W(X(\gamma_2),Y(\gamma_1))$ is an observable which is quite sensitive

to the multipole mixing of, and to the spin changes involved in, the γ transitions. Quite naturally, the detectors must be located asymmetrically with respect to the beam axis.

Generally speaking, the quantities $W(X(\gamma_1),Y(\gamma_2))$ depend upon a number of variables including the angle of the detectors with respect to the beam axis, the spin sequences, the population parameters, and the mixing ratios. However, for "monotonic stretched" cascades (i.e. those with ΔI = constant and $L = |\Delta I|$ where $\Delta I = I_i - I_f$ and I_i, I_f are the spins of the initial and final states, respectively) the DCO-ratio is unity for any two γ rays in the cascade.[26,28] Additionally, the DCO-ratio for two γ rays, one of which is a member of a stretched L = 1 cascade, the other of which is a member of a stretched L = 2 cascade is either 0.5 or 2.0, dependent on which way the ratio is taken.[28] In both of these circumstances the value of the population parameter and the value of the angle the detectors form with respect to the beam axis do not affect the result. In order to attain a DCO-ratio of 0.5, 1,0 or 2.0 under circumstances other than those stated requires an unusual set of conditions.[28] That is to say, it is difficult to have reasonable values for all of the variables and still obtain a value for the DCO-ratio of 0.5, 1.0 or 2.0.

With these things in mind, it was decided to use the DCO-ratios obtainable from the coincidence data as a guideline for spin and parity assignments. It was felt that these measurements should be used only as a guideline because a calibration run with the detectors at symmetric angles was not made, because an exact statistical treatment of the error was not made, and because no theoretical calculations

with assiciated corrections for the solid angle subtended by the detector were performed.

Doppler Broadened Peak Shape Lifetimes

The direct determination of the lifetime of a nuclear state can often be useful in distinguishing between spins and/or mixing ratios allowed by other data. One means of accomplishing this is to utilize the Doppler shift of electromagnetic radiation emitted from a moving source. There are two different techniques based on this effect, the recoil distance method (RDM) and the Doppler shift attenuation method (DSAM). The DSAM technique was applied to Coulomb excitation data in this work, and this technique will be discussed in a manner similar to the treatment of Fossan and Warburton.[29]

In the DSAM technique, the time scale is derived from the slowing down time of a recoiling nucleus in a stopping medium. That is to say, using the stopping power of the medium for a particular nucleus, a relationship between time and velocity can be established. For Coulomb excitation, at t = 0 various levels are directly populated and the initial recoil velocity can be determined. Now the velocity of a recoiling nucleus when it emitted a particular γ ray can be deduced from the amount of Doppler shift of this γ ray as given by

$$E = E_0(1 + \beta\cos\Theta). \qquad (3\text{-}39)$$

Here E_0 is the unshifted γ ray energy, θ is the angle between the velocity vector of the recoiling nucleus, $\vec{v}$, and the direction of γ

ray emission, $\vec{k}_\gamma$, and $\beta \equiv v/c$. Knowing this "slowing down" velocity, the time versus velocity relationship can then be used to deduce the lifetime of the level if it is directly populated and not fed significantly from above. Obviously it is desired to have the recoiling excited nuclei as monoenergetic and unidirectional as possible because any spread in θ or v will ultimately be reflected as a spread in time.

The actual lifetime determination is made by comparing the observed peak shape with those "theoretically" predicted for different lifetimes. In this work, the "theoretical" shapes were generated by using two computer programs, DOPCO[30] and TUTTLAID[30]. First, DOPCO generated a "raw" spectra of relative number of counts versus energy for each lifetime of interest. This was done in the following manner. Choose the beam energies E_B, (maximum beam energy which is the projectile energy to a minimum beam energy at which levels of interest are not significantly populated) and the recoil angles of the projectile θ_R, to consider. With each set of E_B, θ_R there is an associated probability of excitation $P_e = P(E_B)P(\theta_R)$ which can be calculated from Coulomb excitation theory. Now, as indicated earlier, with each "slowing down" velocity v, there is an associated time, t. For each v,t pair, there is a E_{obs}, $P_d \cdot P_y(t)$ pair. Here E_{obs} is the energy of the observed γ ray, $P_y(t)$ is the probability of the nuclear level decaying, and P_d is the probability of detecting this γ ray. Starting at v_{max} and going to $v = 0$ in a uniform number of steps, put a number $P = P(E_B) \cdot P(\theta_R) \cdot P_y(t) \cdot P_d$, where P is the relative number of counts, in the assiciated energy increment. Repeat this whole process for the

range of θ_R to be considered. Finally, all of the preceding must be repeated for each energy E_B.

Program TUTTLAID[30] takes this "raw" spectra, and generates one to compare to the data. To do this, one needs to input the full width at half maximum, the centroid, and number of counts for the peak of interest, as well as the keV/channel for the data. Then, the peak of interest (with background stripped out) can be compared to "theoretically" predicted peaks in order to determine the lifetime.

CHAPTER 4

EXPERIMENTAL ARRANGEMENT AND PROCEDURE

1. GENERAL

Two basic types of experiments, γ-ray singles and γ-γ coincidences were performed in this research. The γ-ray singles experiments included yields, angular anisotropies and Doppler shifted peak shape lifetimes for the Coulomb excitation study, and angular distributions for the (HI,xn) study. The γ-γ coincidences were taken for both Coulomb excitation and (HI,xn) studies. The apparatus common to all experiments is as follows: (1) The ORNL EN Tandem Van de Graaff accelerator and associated ion source. (2) Lithium drifted germanium (Ge(Li)) gamma ray detectors mounted on an angular correlation table, with associated electronics for signal processing. (3) A data acquisition, storage, and analysis system consisting of a PDP-11/20 based Tennecomp data acquisition system and a CDC 3200 computer. Items (1) and (2) are shown schematically in Figure 4-1. The rest of this section will discuss selection and operation of the apparatus in general terms, while sections 2 and 3 will discuss aspects and details particular to the two basic types of experiments. In the last two sections, Ge(Li) detector efficiency and reduction of γ-ray spectra will be discussed.

The projectile ion beam is first formed by extracting positive ions of a suitable type from a duoplasmatron-type[31] ion source. Upon extraction, these ions are injected into a charge exchange canal

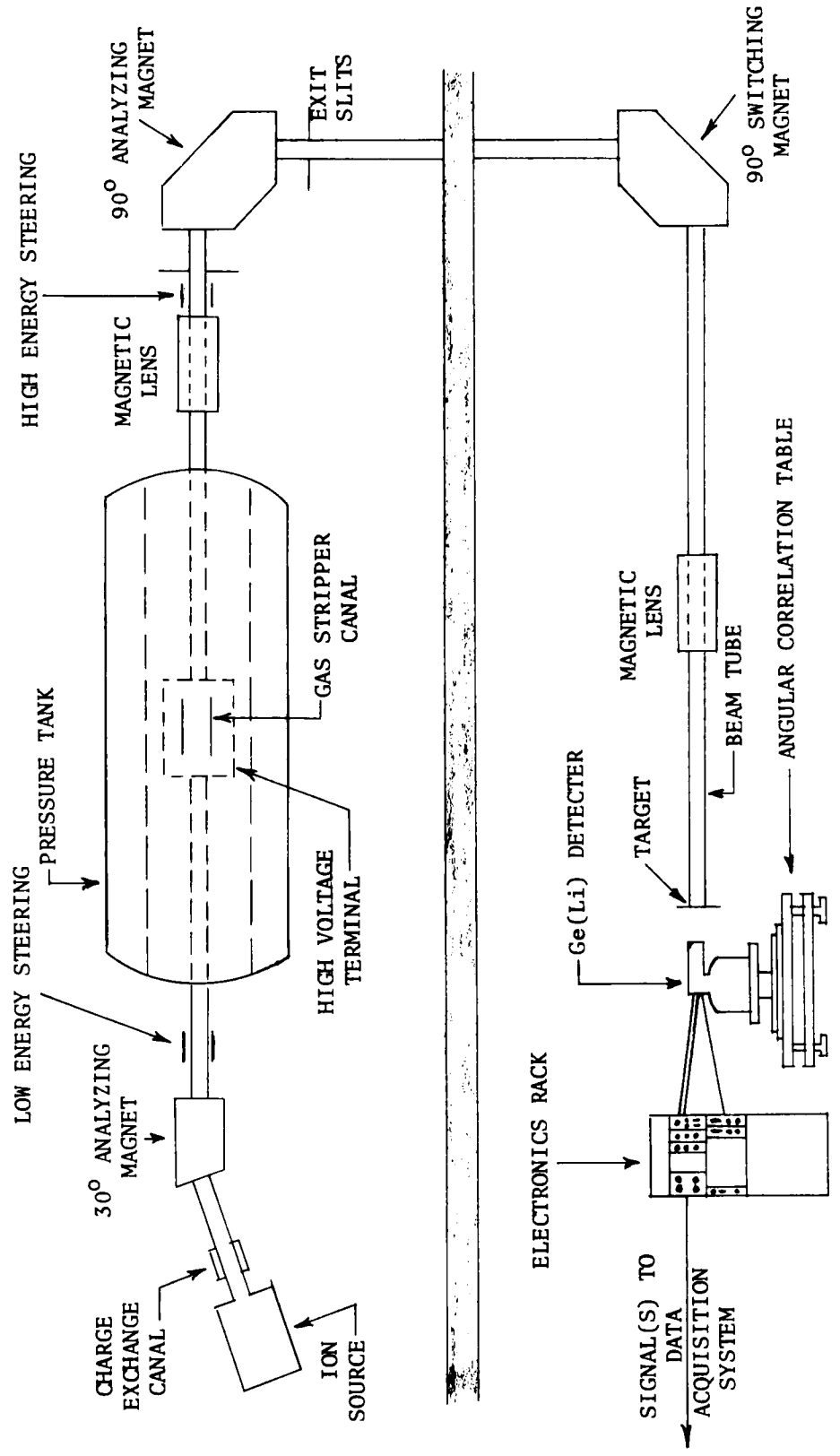


Figure 4-1. Schematic illustration of the arrangement for performance of Coulomb excitation and (HI,xn) experiments with the ORNL EN tandem Van de Graaff accelerator.

where a usable fraction of them acquire a single negative charge. From here they are then accelerated for analysis by a 30° magnet, which injects the proper component into the low energy end of the accelerator. At this point, the ions are attracted to the high positive potential of the terminal where a gas filled stripper canal removes electrons from the beam in a manner causing it to have a distribution of charge states. The resultant multicomponent beam is then pushed out the high energy end of the accelerator by the positive terminal voltage and is momentum analyzed by the 90° analyzing magnet to obtain the proper species and energy. Finally, the beam is directed towards the target by the 90° switching magnet. Focusing of the beam on target is facilitated by two magnetic quadrupole lenses, while positioning is aided by two sets of electrostatic deflectors. In all experiments, the beam spot was less than 7 mm square, and typically was a rectangle 5 mm by 1.5 mm.

Beam stability is enhanced by a system in which the differential current to the exit slits following the 90° analyzing magnet is fed back to a device which adjusts the terminal voltage (via the corona current) to maintain the same current on both slits. The 90° analyzing magnet was previously calibrated using known reaction thresholds, and its magnetic field is monitered continuously with a nuclear magnetic resonance probe. The uncertainty in beam energy has been previously reported[17] to be 0.2%.

Three detectors were used in this work, all of the true coaxial Ge(Li) type, in which the crystal is cooled by a cold finger immersed in a liquid nitrogen dewar. They were rated at 10%, 13% and 23%

the efficiency of a 3 inch by 3 inch NaI crystal, when both are located 25 cm from the target, and had a full width half maximum for the 1332 keV transition from ^{60}Co of 2.20, 2.15 and 2.40 keV, respectively. Because x-rays generated by the beam stopping in the target would increase counting rates substantially, graded shields of 0.0035 inches Mo and 0.005 inches Cu were placed in front of the detectors to supress them. All detectors were securely shock mounted on the angular correlation table. An alignment procedure was then carefully followed to insure that the beam axis was the same as the Ge(Li) crystal axis when the detector was located at 0°, that the crystal rotated in a plane perpendicular to the plane of the target, and the center of rotation was the spot where the beam hit the target.

Three targets were used in this research, all utilizing 0.005 inch nickel spinnings as backings. The ^{115}In target was a natural indium foil of 0.004 inches and 74 mg cm^2 thickness spot welded onto the backing. An isotopically enriched (96.4%)^{113}In target was obtained from the AEC loan pool in the form of a foil. However, it proved to have too many low Z contaminants, so a refabricated thick ($\sim$ 76 mg/cm^2) target was obtained by electrodeposition onto a spinning. The ^{110}Pd target was also an electrodeposition onto a spinning. It was isotopically enriched to 91.4% and was approximately 52 mg/cm^2 thick.

The data acquisition, storage, and analysis system is described in Reference 30.

2. THE γ-RAY SINGLES EXPERIMENTS

A block diagram of the electronics and data acquisition system set-up utilized for the γ-ray singles experiments is shown in Figure 4-2. After the electronics were set up and the detector turned on, a set of radioactive sources was placed near the detector. Gain settings in the electronics were set to obtain the desired energy range. Adjustments were then made in the pole-zero potentiometer, differential and integral filter time constants, and base line restoration settings to obtain the best peak shape and minimum full width half maximum for the anticipated count rate.

Because of relatively small cross sections, the most efficient Ge(Li) detector available was used for the Coulomb excitation yield and angular anisotropy experiments. For equivalent counting rates in determining angular anisotropies this means that one can operate further from the target so as to minimize geometrical effects. Despite relatively small cross sections, a better resolution, less efficient detector was used for the Coulomb excitation Doppler broadened peak shape lifetime studies because of the obvious importance of peak shape. Since the cross section was relatively large for the $^{110}Pd(^{6}Li,3n)^{113}In$ reaction, a better resolution, less efficient detector was used here also.

Projectile selection was based on several factors, including availability, maximum current attainable, and maximum energy attainable. For Coulomb excitation yields and angular anisotropies, these considerations in addition to a desire to maximize yield, to minimize unknown contaminants, and to minimize Doppler broadening led

ORNL-DWG 75-15721

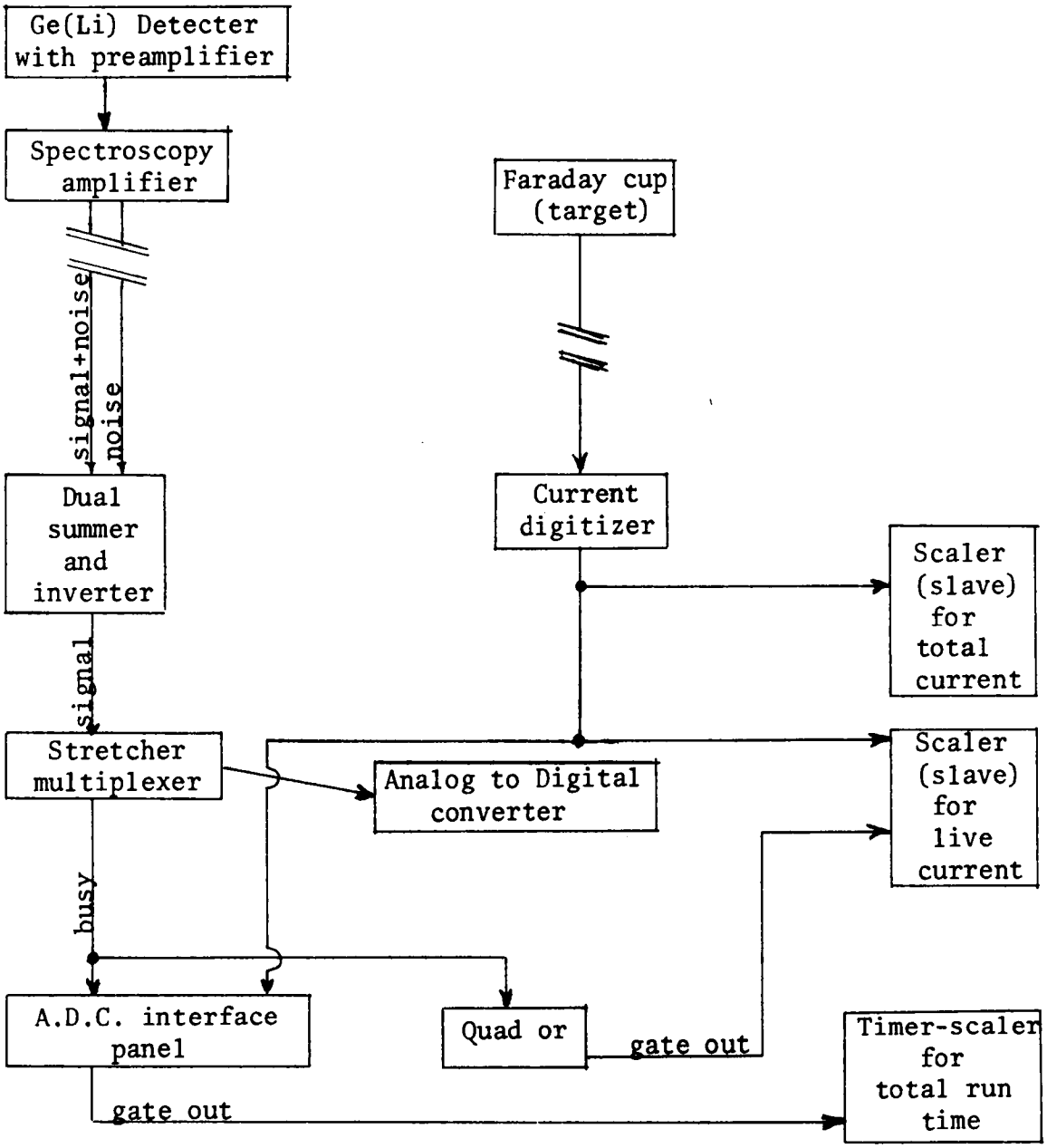


Figure 4-2. Block diagram of the electronics setup for γ-ray singles experiments.

to the use of ^{4}He. For the Coulomb excitation Doppler broadened peak shape lifetime study, it was desired to maximize target ion recoil velocity while still obtaining appreciable yield. Hence, an ^{16}O beam was used. To reach a compound nucleus of ^{116}In for the (HI,xn) studies, target and machine considerations limited the choice to Li.

Detector efficiency measurements were performed as soon as convenient after each singles run in order to reproduce actual running conditions as nearly as possible. In all cases, this provided an energy calibration for the spectra. For the Coulomb excitation yields, detector efficiency is necessary for calculation of B(E2)'s. For the angular anisotropies and angular distributions, such measurements can be used to estimate and correct for geometrical effects. This is especially important in the absence of internal calibrations. For Doppler broadened peak shape lifetimes, it is important to know the full width half maximum as a function of energy as well as to have a good energy calibration.

The angle of the detector with respect to the beam was 55° for the yield measurements. This was chosen because $P_2(\cos(\theta)) \tilde{=} 0$ so that angular distribution effects are minimized. The anisotropy measurements were performed by definition at 0° and 90°. This is also the position where the Doppler broadened peak shape lifetime measurements were performed. For the (HI,xn) angular distributions, yields were taken at 0°, 22.5°, 55°, and 90°. A schematic showing of these detector positions is shown in Figure 4-3.

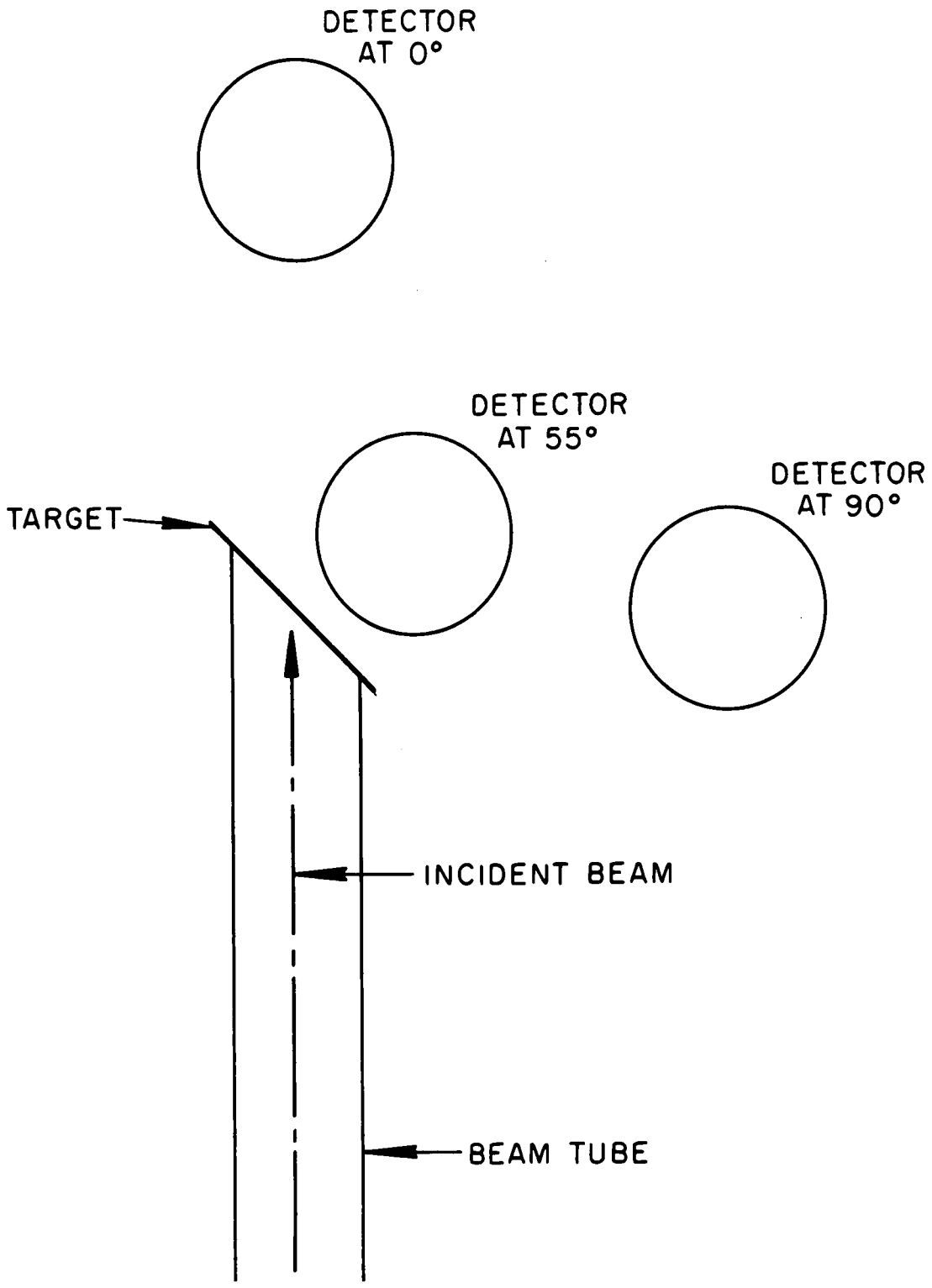


Figure 4-3. Ge(Li) detector positions for Coulomb excitation and (HI,xn) studies, top view.

3. THE γ-γ COINCIDENCE EXPERIMENTS

The electronics and data acquisition set-up for the γ-γ coincidence experiments is shown in Figure 4-4, 4-5. The procedure is as follows: (1) Set up as you would to take 4096 channels of singles data for both detector "0" and "1". The data will initially be stored in the PDP-11/20 in a two dimensional 4K X 4K event by event format. (2) Put up some sources and adjust the gain on the timing filter amplifiers consistent with the energy range desired (typically 3 MeV $\leftrightarrow$ 10 volts). (3) Put up a ^{241}Am source and adjust the levels on the constant fraction discriminators to allow the 60 keV γ ray to pass. The objective here is to set the level as low as possible, but above the noise. (4) Position the two detectors so they face one another and put up a ^{22}Na and/or a ^{60}Co source. Open the leading edge single channel all the way, putting its output into a stretcher multiplexer. Take "singles spectra" for two different delay settings to obtain a time per channel calibration. Now, put in the desired delay (typically 100 nsec) and adjust the leading edge single channel to obtain the window width. (5) Adjust the two regular single channels feeding the triple coincidence box to pass the γ-ray energy range of interest. This part of the apparatus is optional, but if used, one must check for overlap at the triple coincidence box. (6) Adjust the system so the event pulse comes before the linear energy signal leaves the baseline and so that the gate pulse continues past the peak of the linear energy signal. (7) Position the detectors at the desired angles. The distances from the target are determined by such things as individual efficiencys, singles counting

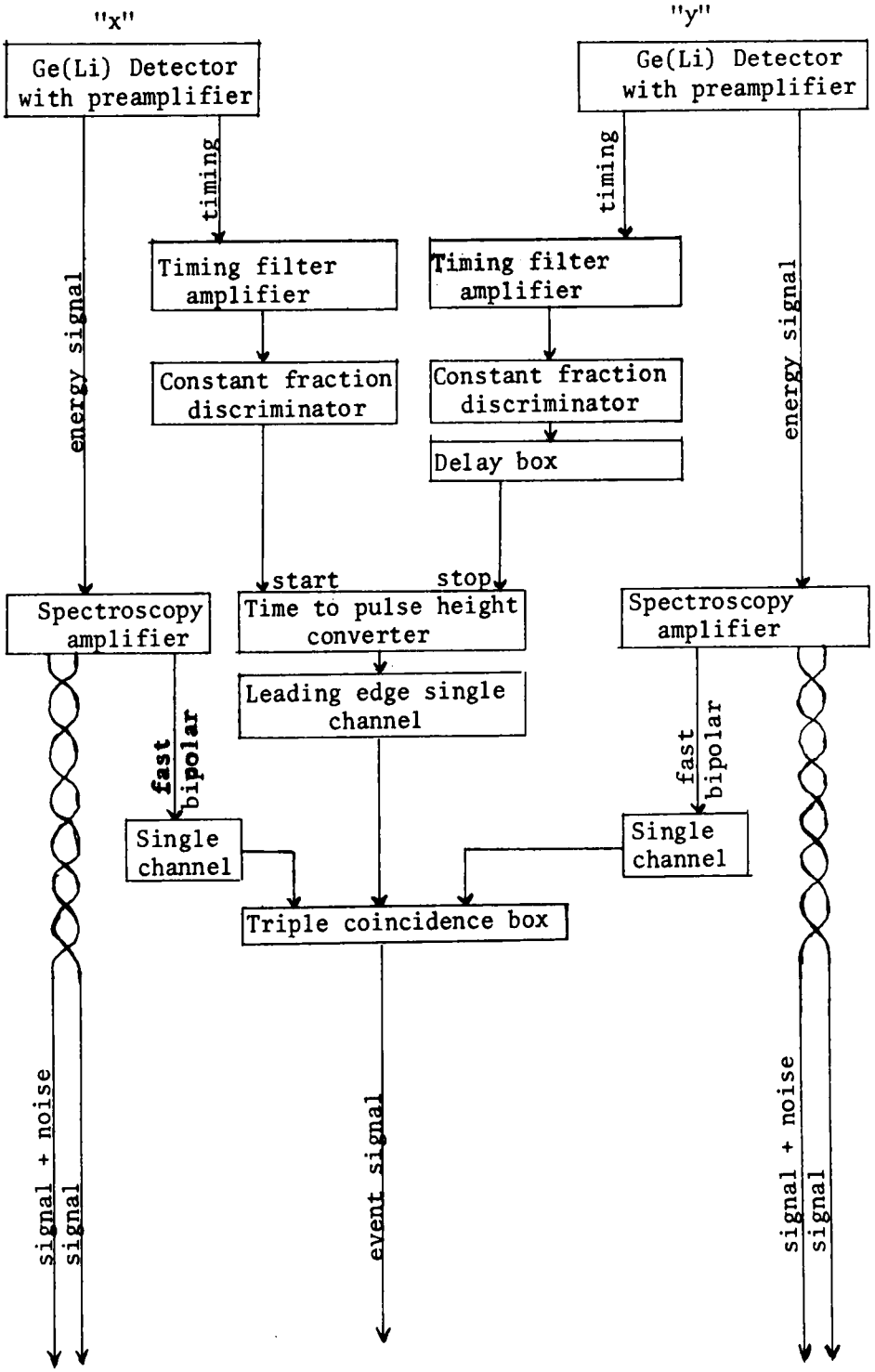


Figure 4-4. Block diagram of electronics setup adjacent to the target for γ-γ coincidence measurements.

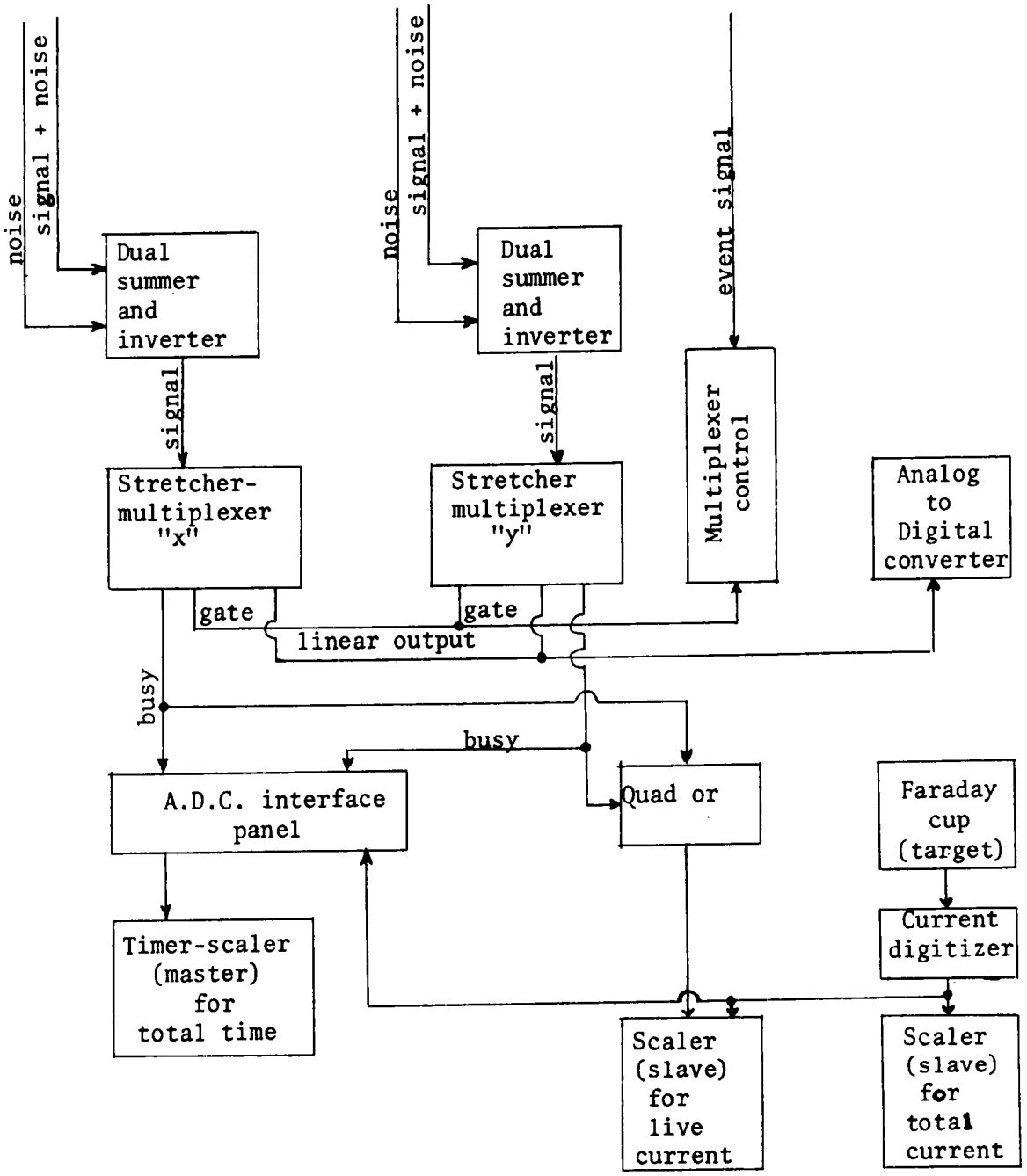


Figure 4-5. Block diagram of the electronics setup adjacent to the data acquisition system for γ-γ coincidence measurements.

rates, coincidence counting rates, and the desire for triple correlation data. Also, if possible, put shielding between the two detectors to reduce false coincidences arising from Compton scattering between detectors.

When the system is taking data, the PDP-11/20 will take 1024 4K X 4K events then dump them on a special file on the CDC 3200 computer. When this file is full, it is processed by program PUSSE[30] into a set of gate by 4K channel spectra and/or a two dimensional 1K X 1K spectra. Reference 30 tells how to implement PUSSE and how to obtain copy of the final form of the data. At the conclusion of each run, one might dump and save the summed "X" and "Y" gates to assist in setting γ-ray and background gates in the 1K X 1K data. Also, one should make efficiency measurements before repositioning the detectors. This should be done in the "gated" mode using the output of the constant fraction discriminator to generate an event signal.

For the Coulomb excitation experiments, a ^{4}He beam of 10.6 MeV was used, while a ^{6}Li beam of 24.0 MeV was used for the (HI,xn) experiment. The choices were made for reasons given in Section 2.

4. Ge(Li) DETECTOR EFFICIENCY

Determination of absolute or relative detector efficiency is a crucial part of many γ-ray experiments. Often the uncertainty in detector efficiency is one of the main sources of error in the experiment. The method used for determining Ge(Li) detector

efficiency in this research is as follows: After finishing a run, replace the target with one of six available ^{226}Ra γ-ray sources. These vary in strength, so use the one which suitably approximates the counting rate of the experiment. Take a singles spectrum long enough (typically fifteen to thirty minutes) to obtain good statistics. Reduce the resultant γ-ray spectra.

For each γ ray in the spectrum, calculate the absolute efficiency $\varepsilon(E)$ and an error at that particular energy. The absolute efficiency is given by $\varepsilon(E) = N_C \frac{EXP(A \cdot \mu_m(E))}{T_L \cdot N_e}$ where N_C is the number of counts in the peak, A is an absorption constant, $\mu_m(E)$ is the mass attenuation coefficient, T_L is the live counting time in seconds, and N_e is the number of γ rays of energy E emitted per second. For the sources used in this work, A = 0.103. After calculating these efficiencies, there are two ways to proceed. For more critical applications, obtain a least squares fit to the data and generate a table of energy versus efficiency. It is usually preferable to do this in two energy ranges such as 100 to 1000 keV and 600 to 2000 keV. For less critical applications, a plot of a curve drawn through the data points will do.

Two obvious questions arise when ascertaining the accuracy of this method. First, how close is the source to the position where the beam strikes the target? The answer is very close. The source is fabricated to fit the beam "snout" in the same manner as a nickel spinning, including a 1 mm recess to simulate the "suck in" of the spinning under vacuum. Secondly, how accurately is the source strength known? This is determined by calibrating the radium sources

against an N.B.S. source. This source is one whose absolute γ-ray intensities are certified by the National Bureau of Standards to an accuracy of 1.2% to 3.0% depending upon the γ ray in question.

Perhaps the remaining uncertainty concerns the attenuation of γ-ray intensity in the experiment due to its travel through such things as the target, snout and spinning. With good statistics, the uncertainty in efficiency is approximately 5% overall. It is perhaps a bit better a energies greater than 250 keV, and much worse below 100 keV or so. This latter result is due to lack of calibration points and greater attenuation of γ rays in this energy range.

5. REDUCTION OF SPECTRA

The reduction or "stripping" of a γ-ray spectra is the determination of the true or net number of counts in the peak of interest. When this number is divided by the detector efficiency at that energy, the γ-ray intensity is determined. The discussion in the section will be done in two parts, reduction of singles and reduction of coincidence data. Since γ-ray intensity was not of interest in the Doppler line shape data, it was not stripped out.

Singles data, whenever possible, was reduced by three different methods. These were by "hand calculations," with a light pen, and with in-house computer programs TIZZY[30] and NASTY.[30] By "hand calculations" it is meant that a number of channels above and below are summed and normalized for a background calculation which is then subtracted from the total counts in the peak. In this procedure,

$$\text{Gross Counts } (N_G) = N_1 \pm \sqrt{N_1} \quad , \tag{4-1}$$

where N_1 is the total number of counts in the peak,

$$\text{Background Counts } (N_B) = f(N_2 \pm \sqrt{N_2}) \quad , \tag{4-2}$$

where N_2 is the total number of counts in the background and f = (number of channels in the peak)/(number of channels in the background) so that

$$\text{Net Counts } (N_N) = (N_1 - fN_2) \pm \sqrt{N_1 + f^2 N_2} = N \pm \varepsilon_N \; . \tag{4-3}$$

The expression for the error, ε_N, comes from statistical considerations, and corresponds to the one standard deviation. The procedure for reduction via light pen or in-house programs in described in Reference 30. With the light pen, each peak was stripped several times, and a best estimate obtained with an associated error which was due to inconsistency in background determination and/or resolution of a doublet or triplet. The in-house programs were run until a satisfactory fit was obtained. The error quoted in them is also statistical. The final number taken for use in calculations was a judicious average of the values obtained by the three methods. More specifically, if a peak was isolated, and of reasonable strength, the values were weighted equally, and the associated error quoted was only statistical unless circumstances dictated otherwise. For peaks

which were weak and/or part of a multiplet, the values obtained were weighted by confidence in the particular method. Errors quoted for such peaks not only contained the error due to statistics, but also included a factor which represented error due to uncertainty in background and/or resolution of a multiplet. Generally speaking, the light pen was best at resolving a multiplet, while the "hand calculations" did the best with weak peaks.

In this research, only the 1K X 1K, event by event, form of coincidence data was taken. The first step in reducing these data was to establish the γ-ray gates. Then, the summed "X" and "Y" spectra were examined to determine channels to include in the γ gate, and in upper and lower background gates. Background gates were set as close as practical to the γ-ray gate, avoiding if possible setting them on other γ rays. With program GATOR,[30] a minimum of four singles type spectra (main gate in X,Y direction with upper and lower background gates) were generated by subtracting the weighted background gate from the γ gate. These were then stripped out as one would a singles spectra, using the light pen only. For each γ ray, the number of counts and associated error was determined in a qualitative manner. This was to obtain a "best" estimate of the area, along with an upper and lower limit which was a sort of one standard deviation error. These numbers were then averaged in a statistical manner to obtain the number of counts in each direction. The coincidence intensity in each direction could then be determined by use of appropriate efficiencies.

To deduce the level structure, the results were put in a matrix showing coincidences and intensities with the γ ray in both "X" and "Y" directions. Coincident γ rays in this table were placed in two categories, possible and definite. After this, a new set of gates were set on the basis of what was found previously. The whole process is repeated until all fruitful gates were exhausted.

CHAPTER 5

EXPERIMENTAL RESULTS

In this chapter results from the Coulomb excitation and (HI,xn) experiments will be presented. Comments and discussion will be made on the analysis of the data and deduction of the final form of the data when appropriate. However, implications of the data and structure with regards to models will be deferred until CHAPTER 6.

1. COULOMB EXCITATION RESULTS

Level Diagrams

Level diagrams constructed from the information obtained in the Coulomb excitation of ^{113,115}In are shown in Figures 5-1 and 5-2. The vertical arrows represent γ rays. A dot on the top of an arrow indicates a coincidence was observed with γ rays feeding the level from which it decays. A dot on the bottom of an arrow indicates a coincidence was seen with γ rays decaying from the level the γ ray feeds. The number in parentheses at the top of arrows are the branching ratios in percent from that level. In the ^{115}In level scheme, the dashed horizontal lines indicate levels observed[32] in the decay of ^{115,115m}Cd but not seen in this Coulomb excitation study. In the ^{113}In level scheme, the analogous low spin positive parity states are also indicated by dashed lines. The rest of this section will present the results which led to the construction of the diagram along with a summary table of results.

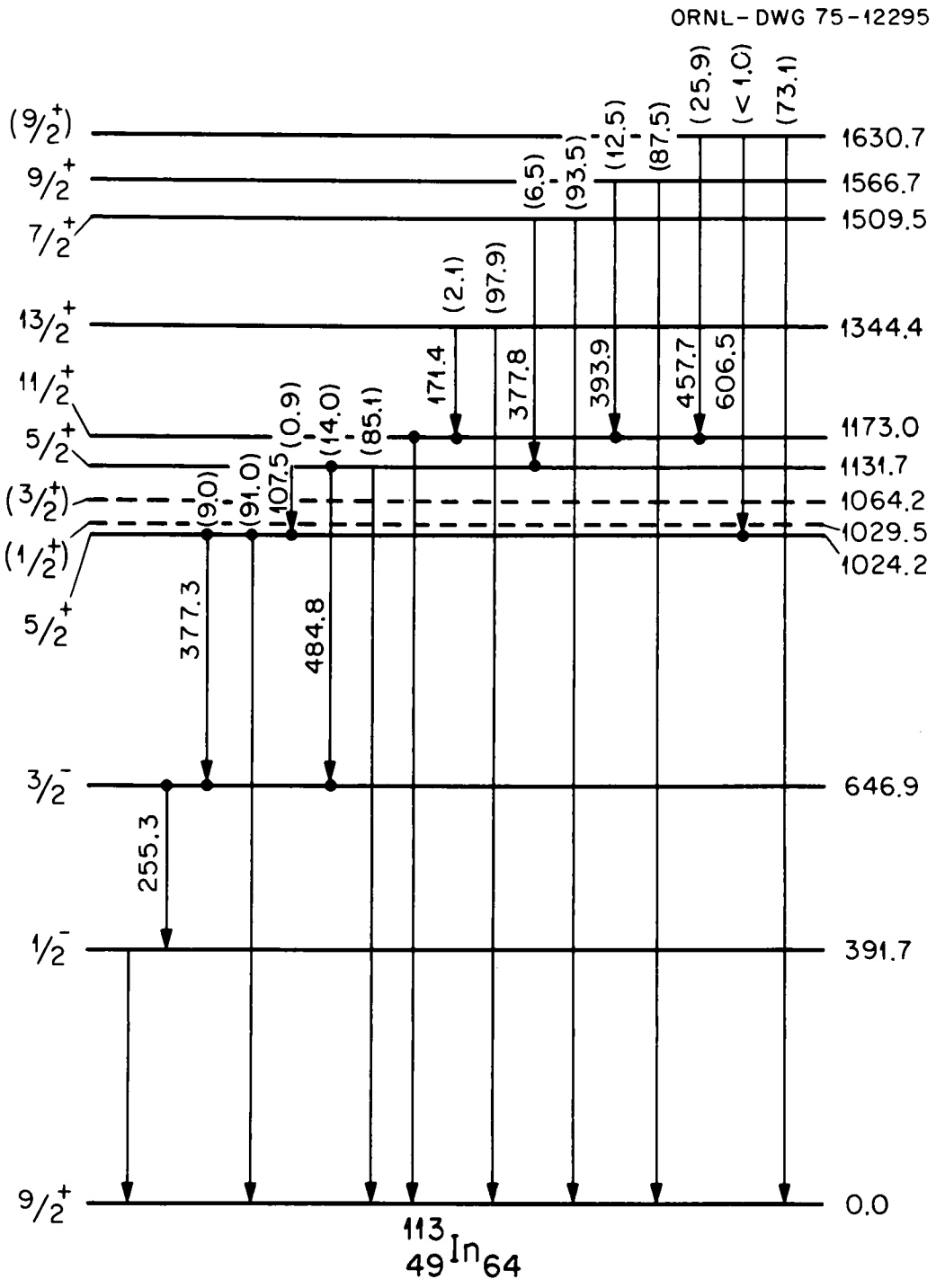


Figure 5-1. Energy levels observed in the Coulomb excitation of ^{113}In. Coincidences and branching ratios are displayed according to the convention of the Nuclear Data Sheets. Dashed lines indicate low-spin positive parity states analogous to those in ^{115}In, but not seen in this work.

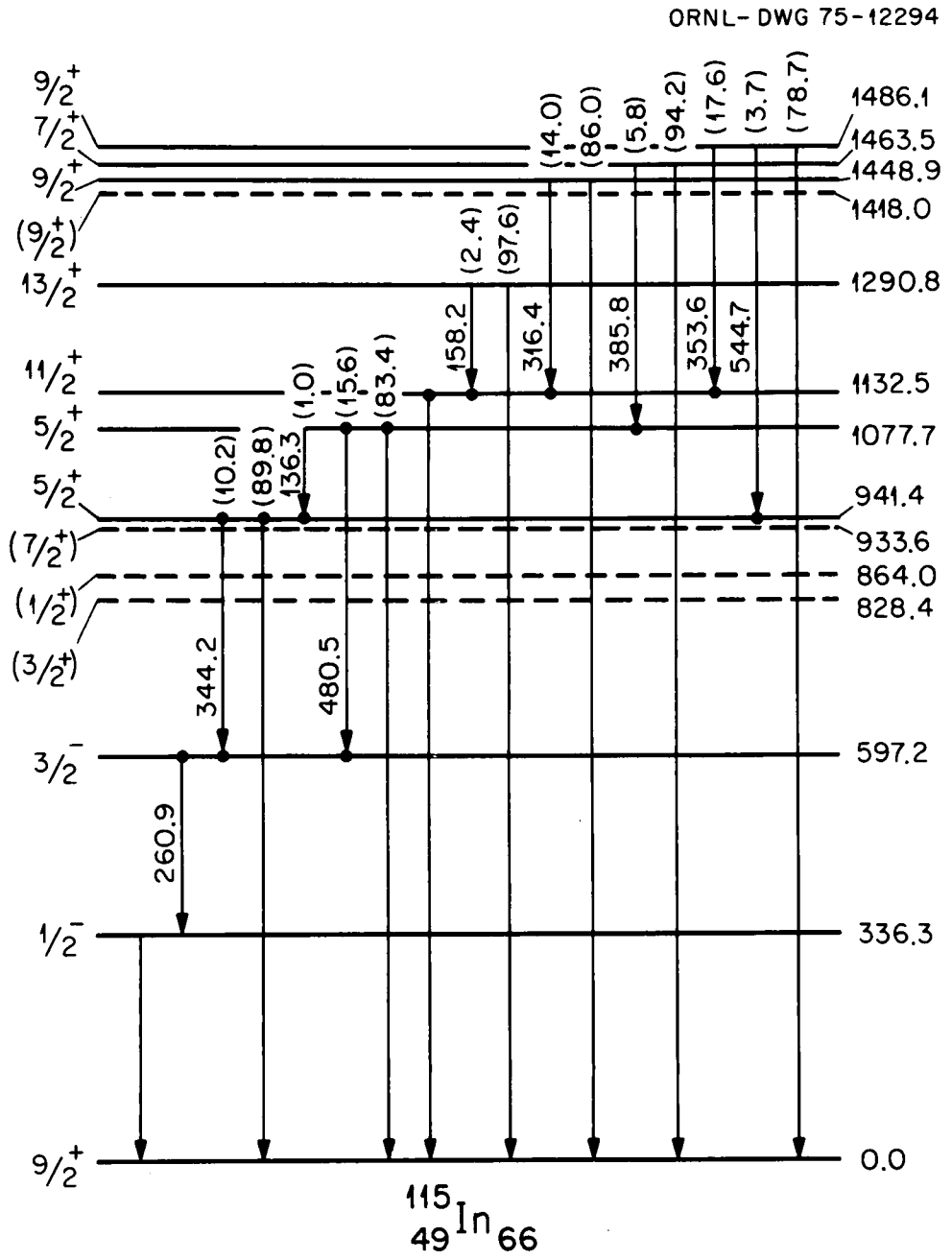


Figure 5-2. Energy levels, observed in the Coulomb excitation of ^{115}In. Coincidences and branching ratios are displayed according to the convention of the Nuclear Data Sheets. Dashed lines indicate low spin positive parity states seen in the decay of ^{115,115m}Cd, but not seen in this work.

Coincidence Information

A summary of the coincidence information deduced is displayed in Table 5-1. This information was used in constructing level diagrams. Since, unfortunately, no gated efficiency curves were run, there is no intensity associated with the coincidence information. However, the intensities in a particular gate (for which single efficiencies could be utilized) were consistent with the yield measurements.

The γ-ray Yields

Typical spectra resulting from the Coulomb excitation of ^{113,115}In are shown in Figures 5-3, 5-4, 5-5 and 5-6. The spectra observed were fairly clean, showing typical Coulomb excitation contaminant γ rays, and some γ rays due to the presence of Fe and Zn in the ^{113}In target.

The $B_{ex}(E2)$ values were extracted from the measured yields by the procedure discussed earlier. Results for ^{113,115}In are presented in Table 5-2, and are displayed graphically in Figures 5-7 and 5-8. These values are the average of the results obtained with the Ge(Li) detector located at 55° with respect to the beam, and α-particle beam energies of 9.4, 10.0, and 10.6 MeV. The assigned errors for the absolute $B_{ex}(E2)$ values result from uncertainties in peak area, in the calibrated efficiency of the Ge(Li) detector, and in the stopping power of α-particles in In. When appropriate, corrections for internal conversion have been made.

TABLE 5-1

Summary of coincidence information obtained from the Coulomb excitation of $^{113,115}In$

Transition Energy (keV)	Coincident γ-Rays (keV) Definite	Possible
	^{113}In	
107.5	377.4, 1024.2	
171.4	1173.0	
255.3	377.4, 484.8	107, 607
377.4	255.3, 484.8, 1131.7	607
393.9	1173.0	
457.7	1173.0	
484.8	255.3, 377.4	1024.2
606.5		377.4, 1024.2
1024.2	107, 607	
1131.7	377.7	
1173.0	171.4, 393.9, 457.7	
	^{115}In	
136.3	260.9, 344.2, 941.4	
158.2	1132.5	
260.9	136.3, 344.2, 385.8, 480.5	
316.4	1132.5	
344.2	260.9, 136.3	
353.6	1132.5	357.7
385.8	260.9, 480.5, 1077.7	136.3
480.5	260.9, 385.8	
544.7	941.4	273.6
941.4	136.3, 544.7	
1077.7	385.8	
1132.5	158.2, 316.4, 353.6	105.8

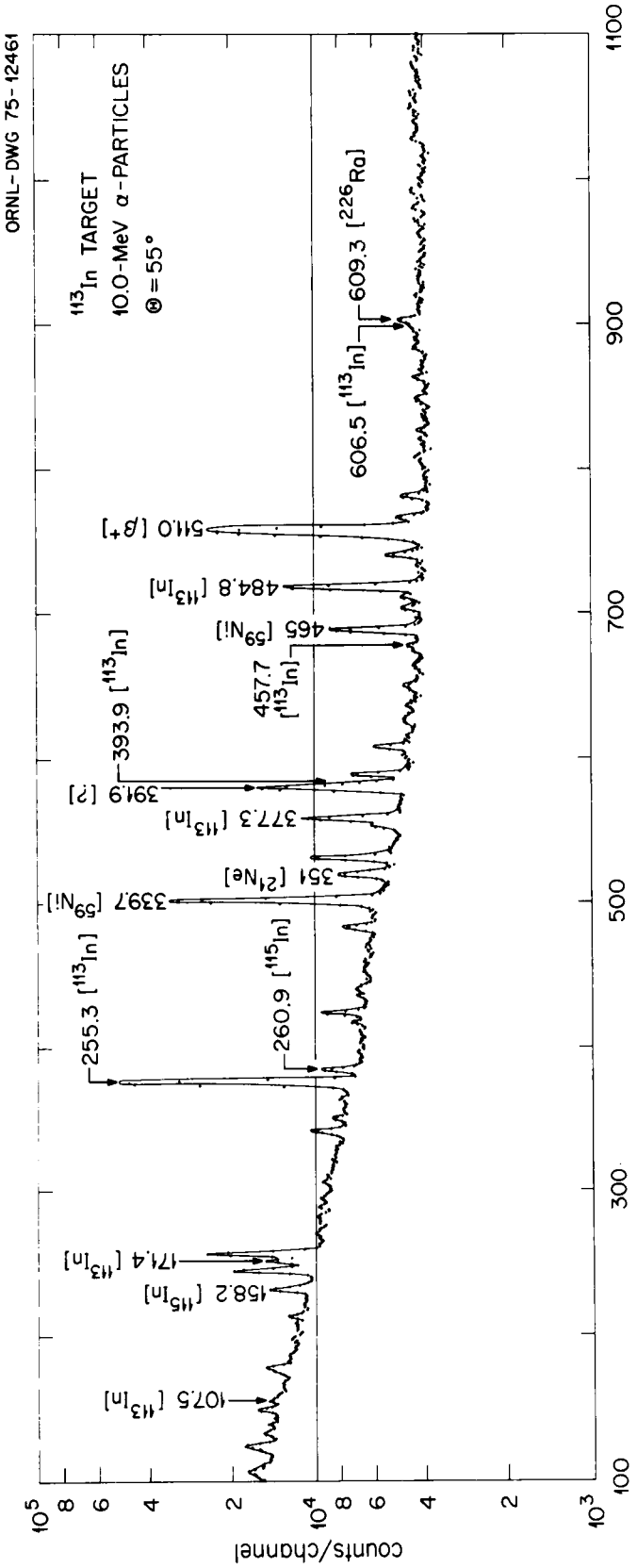


Figure 5-3. Ge(Li) pulse-height spectrum of the low energy γ-rays from an enriched ^{113}In target bombarded with 10.0 MeV ^{4}He ions.

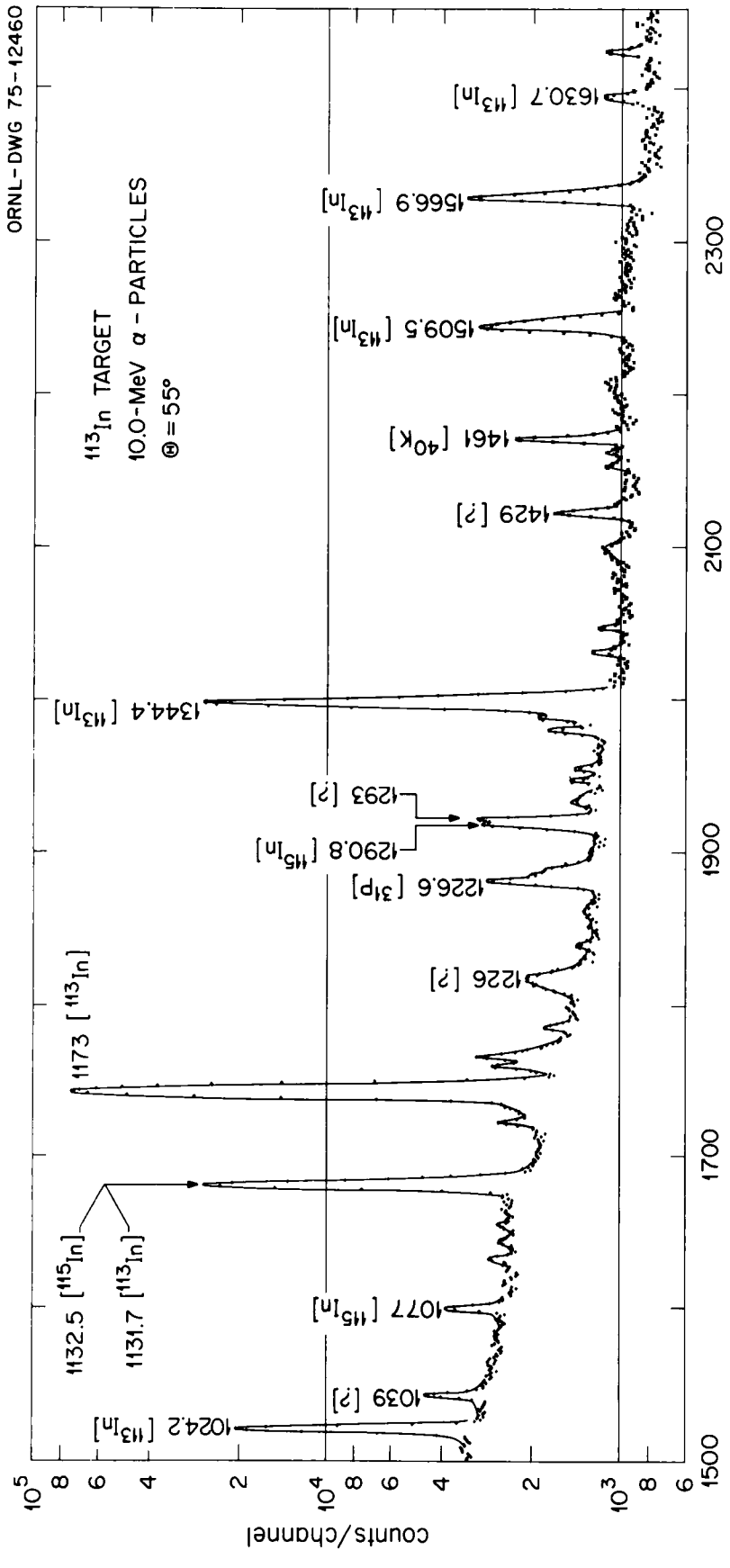


Figure 5-4. Ge(Li) pulse-height spectrum of the high energy γ-rays from an enriched ^{113}In target bombarded with 10.0 MeV ^{4}He ions.

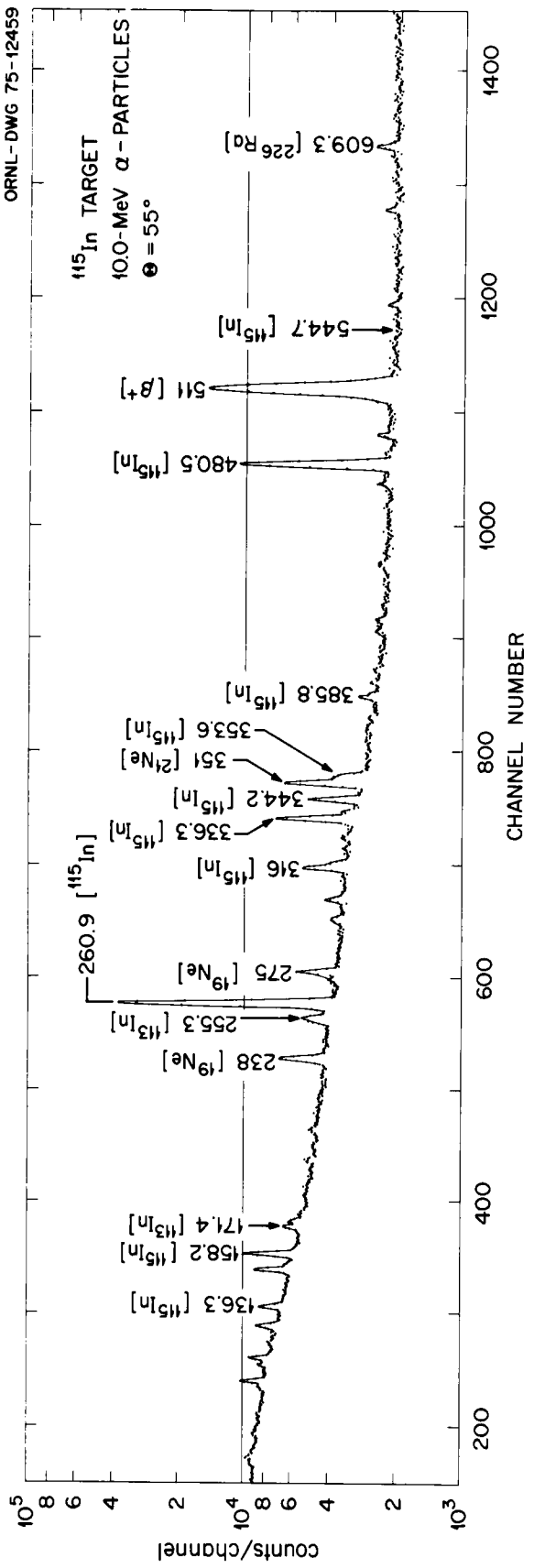


Figure 5-5. Ge(Li) pulse-height spectrum of the low energy γ-rays from a natural indium target bombarded with 10.0 MeV ^{4}He ions.

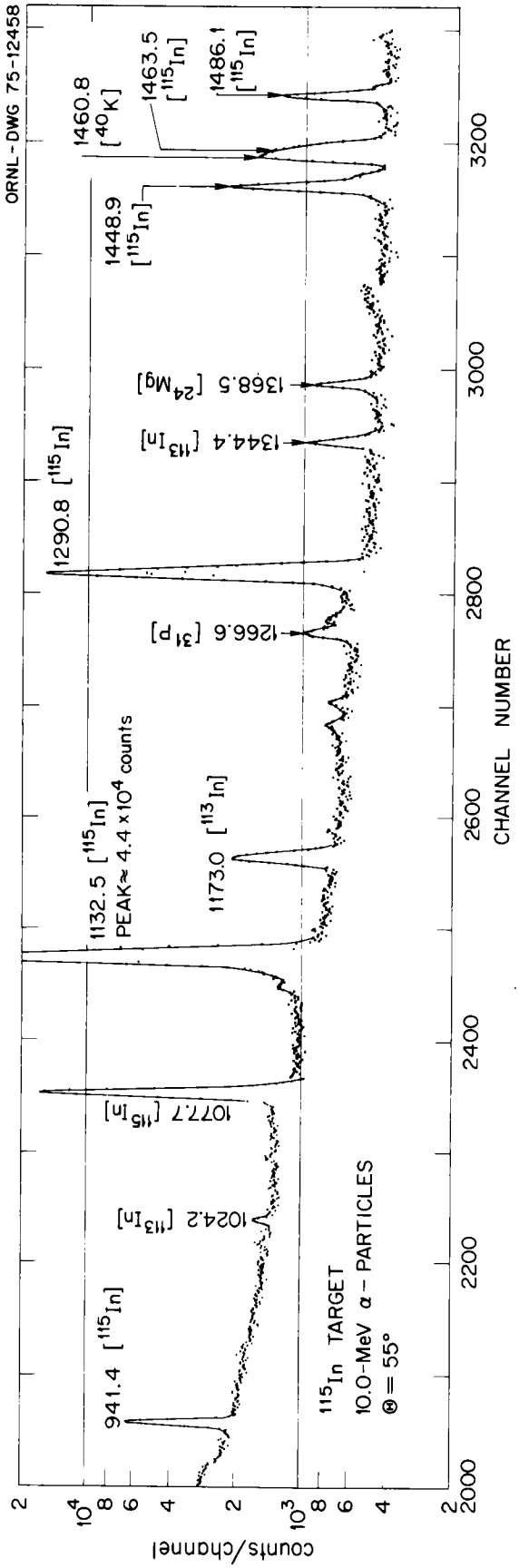


Figure 5-6. Ge(Li) pulse-height spectrum of the high energy γ-rays from a natural indium target bombarded with 10.0 MeV ^{4}He ions.

TABLE 5-2

Summary of $B_{ex}(E2)$, $B_{ex}(E3)$ values obtained from the Coulomb excitation of $^{113,115}In$

^{113}In		^{115}In	
Level energy (keV)	$B_{ex}(E2)$ ($10^{-50}e^2cm^4$)	Level energy (keV)	$B_{ex}(E2)$ ($10^{-50}e^2cm^4$)
1024.2	0.754 ± 0.062	933.6	<0.006
1131.7	1.60 ± 0.10	941.4	0.272 ± 0.018
1173.0	9.29 ± 0.56	1077.7	2.27 ± 0.12
1344.4	5.30 ± 0.32	1132.5	10.02 ± 0.52
1509.5	1.45 ± 0.10	1290.8	5.65 ± 0.30
1566.9	1.78 ± 0.12	1418.	<0.034
1630.7	0.316 ± 0.123	1448.9	1.51 ± 0.10
		1463.5	0.959 ± 0.132
		1486.1	0.871 ± 0.094
Level energy (keV)	$B_{ex}(E3)$ ($10^{-75}e^2cm^6$)	Level energy (keV)	$B_{ex}(E3)$ ($10^{-75}e^2cm^6$)
646.9	4.82 ± 0.50	597.2	5.73 ± 0.35

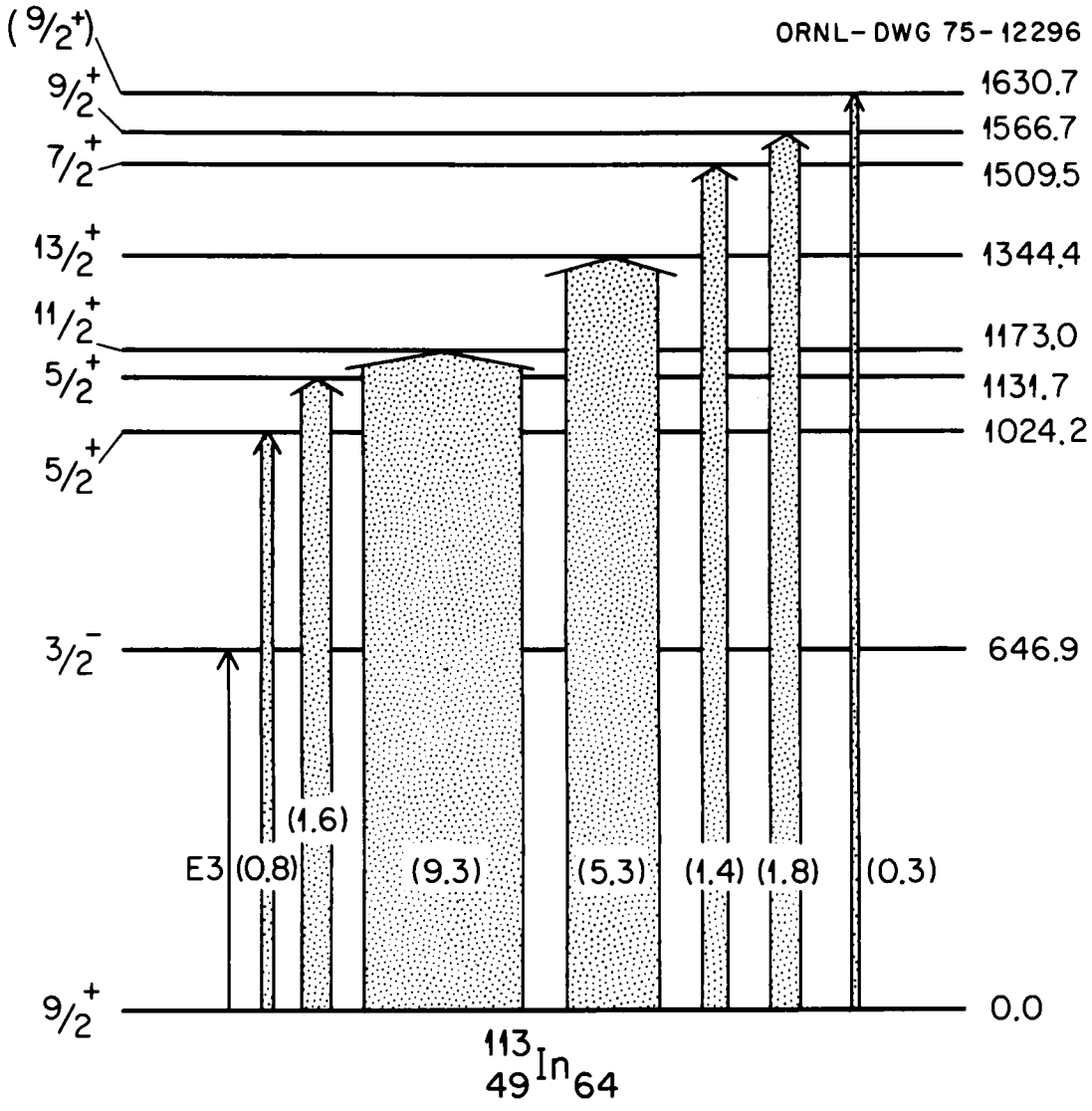


Figure 5-7. Level diagram of ^{113}In displaying excitation strengths to the various states of ^{113}In. Widths of arrows are proportional to the $B_{ex}(E2)$. The number in parenthesis associated with each arrow is the $B_{ex}(E2)$ in units of $10^{-50}e^2cm^4$.

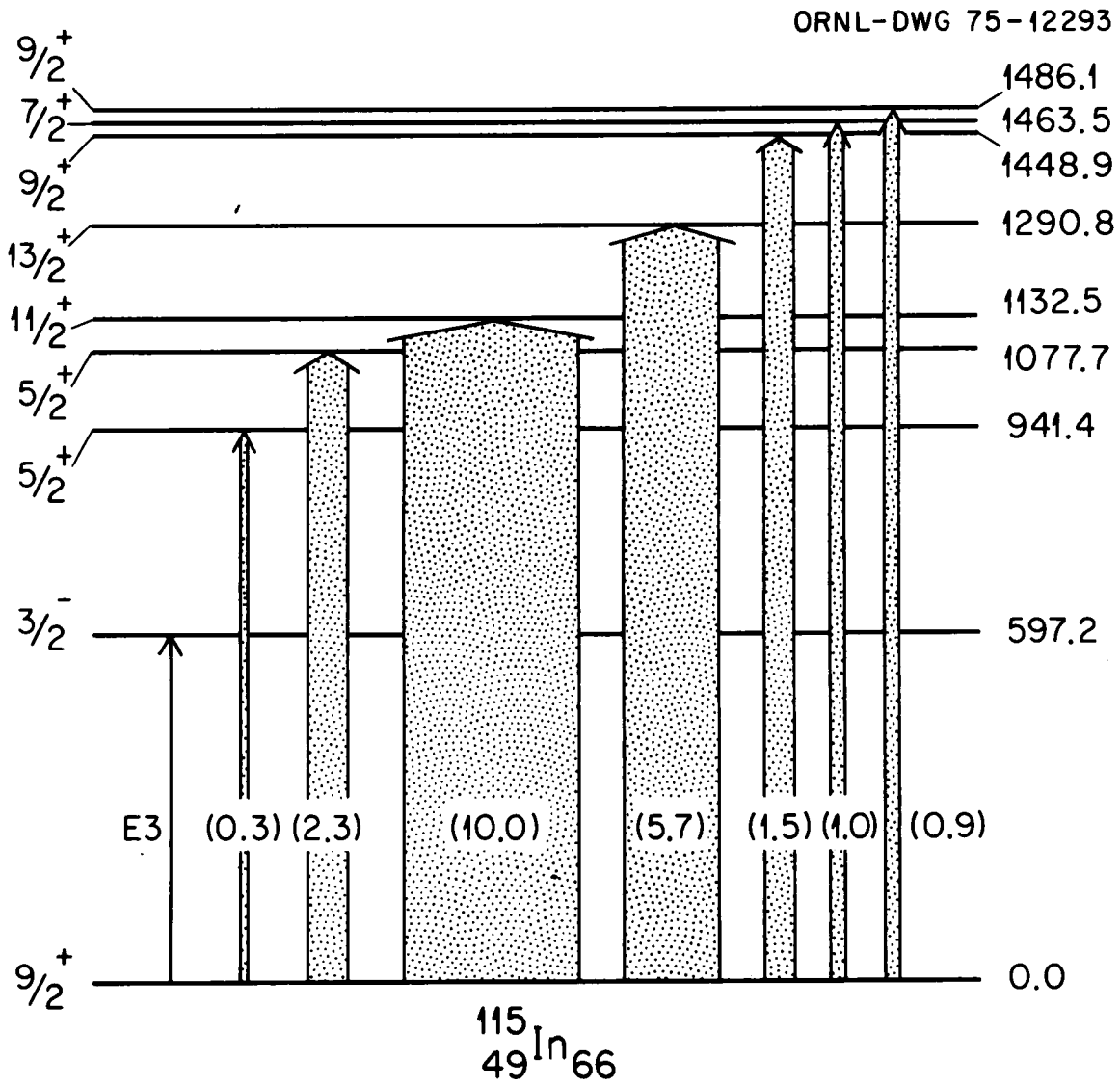


Figure 5-8. Level diagram of ^{115}In displaying excitation strengths to the various states of ^{115}In. Widths of arrows are proportional to the $B_{ex}(E2)$. The number in parenthesis associated with each arrow is the $B_{ex}(E2)$ in units of $10^{-50}e^2cm^4$.

Angular Distributions

Results from the angular distribution measurements are presented in Table 5-3. These were obtained by the method discussed earlier. The data were normalized to give the theoretical A_2 for the pure E2 transitions in both nuclei. Except for low energy γ-rays ($\leq$ 350 keV) the g_2 and g_4 values were essentially constant, being 0.945 and 0.828 respectively for the ^{113}In measurements, and 0.968 and 0.899 respectively for the ^{115}In measurements.

Doppler Broadened Peak Shape Lifetimes

Results of the lifetime determinations are presented in Table 5-4. Typical experimental spectra and calculated shapes which give rise to these determinations are shown in Figures 5-9, 5-10, and 5-11. One means of obtaining better results is to modify the stopping power function for In ions recoiling in In in a manner similar to Stokstad et al.[33] As calibration points, the calibrated lifetimes of two unique transitions (τ(1291) = 1.27 ps, τ(1078) = 0.55 ps) in ^{115}In were used to accomplish this. Also, in examining the fits, greater consideration was given to the high energy tail because of greater confidence in the stopping power at higher recoil energies.

Summary of Results

In Tables 5-5 and 5-6 are presented a summary of the results which includes the B(M1)s calculated for the directly measured data. The basis for assignments is discussed in the next section.

TABLE 5-3

Summary of γ-ray anisotropy results from the Coulomb excitation of $^{113,115}In$

Level (keV)	E_γ (keV)	R = W(0°)/W(90°)	$(a_2)_t$	A_2
		^{113}In		
1024.2	1024.2	1.05 ± 0.02	0.861	+0.04 ± 0.01
1131.7	1131.7	1.01 ± 0.07	0.892	+0.01 ± 0.05
	484.8	0.90 ± 0.03	0.892	-0.08 ± 0.02
1173.0	1173.0	0.98 ± 0.01	0.903	-0.02 ± 0.01
1344.4	1344.4	1.22 ± 0.03	0.945	+0.15 ± 0.02
	171.4	0.89 ± 0.04	0.945	-0.09 ± 0.03
1509.5	1509.5	0.83 ± 0.03	0.979	-0.13 ± 0.02
1566.9	1566.9	1.13 ± 0.04	0.990	+0.08 ± 0.02
1630.7	1630.7	1.06 ± 0.12	1.001	+0.04 ± 0.09
		^{115}In		
941.4	941.4	1.04 ± 0.05	0.833	+0.03 ± 0.04
	344.2	0.80 ± 0.08	0.833	-0.18 ± 0.07
1077.7	1077.7	1.04 ± 0.02	0.877	+0.03 ± 0.02
	480.5	0.90 ± 0.02	0.877	-0.08 ± 0.02
	136.3	1.13 ± 0.12	0.877	+0.10 ± 0.09
1132.5	1132.5	0.97 ± 0.02	0.892	-0.02 ± 0.01
1290.8	1290.8	1.24 ± 0.02	0.933	+0.16 ± 0.02
	158.2	0.88 ± 0.05	0.933	-0.09 ± 0.04
1448.9	1448.9	1.15 ± 0.07	0.967	+0.10 ± 0.05
	316.4	1.14 ± 0.11	0.967	+0.10 ± 0.08
1463.5	1463.5	0.90 ± 0.09	0.970	-0.08 ± 0.07
1486.1	1486.1	1.09 ± 0.09	0.974	+0.06 ± 0.06
	353.6	1.42 ± 0.21	0.974	+0.26 ± 0.13

TABLE 5-4

Mean lives of Coulomb excited states in $^{113,115}In$ obtained by Doppler line shape analysis

Nucleus	Level (keV)	τ(ps)
^{113}In	1024.2	5.5 ± 1.0
	1173.0	0.10 ± 0.06
	1344.4	0.4 ± 0.1
	1509.5	≤ 0.3
	1566.9	0.35 ± 0.15
^{115}In	941.4	$\geq 5.$
	1077.7	1.3 ± 0.2
	1132.5	0.10 ± 0.06
	1290.8	0.55 ± 0.10
	1448.9	$0.15 \begin{smallmatrix} + 0.10 \\ - 0.05 \end{smallmatrix}$ [a]
	1486.1	0.3 ± 0.2 [a]

a) Obtained from yield at $\theta_L = +55°$ with 10.0 MeV α-particles effecting Coulomb excitation.

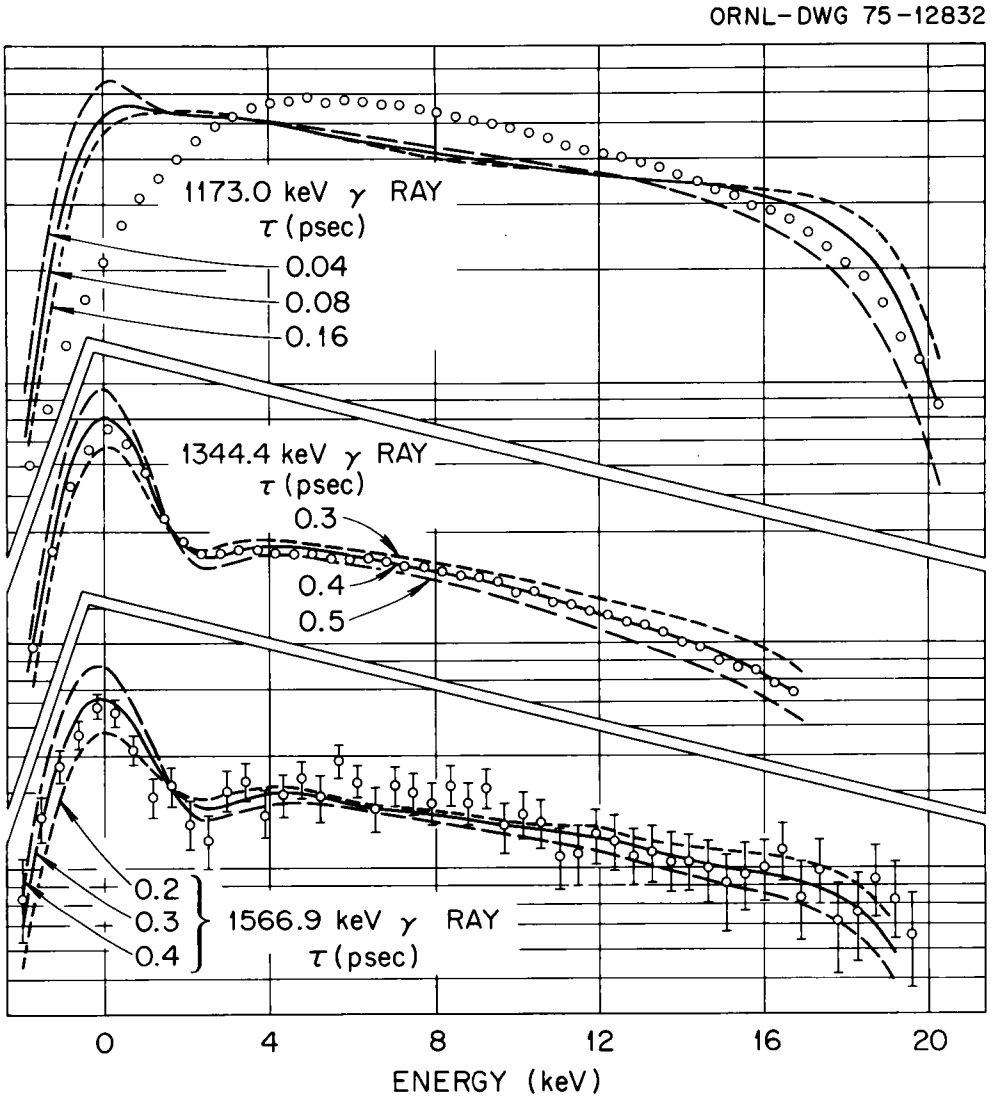


Figure 5-9. Doppler-broadened γ-ray peaks observed when ^{113}In was Coulomb excited with ^{16}O projectiles. The detector was located at 0° to the beam direction. The curves are calculated for different values for the mean-life, τ, in ps.

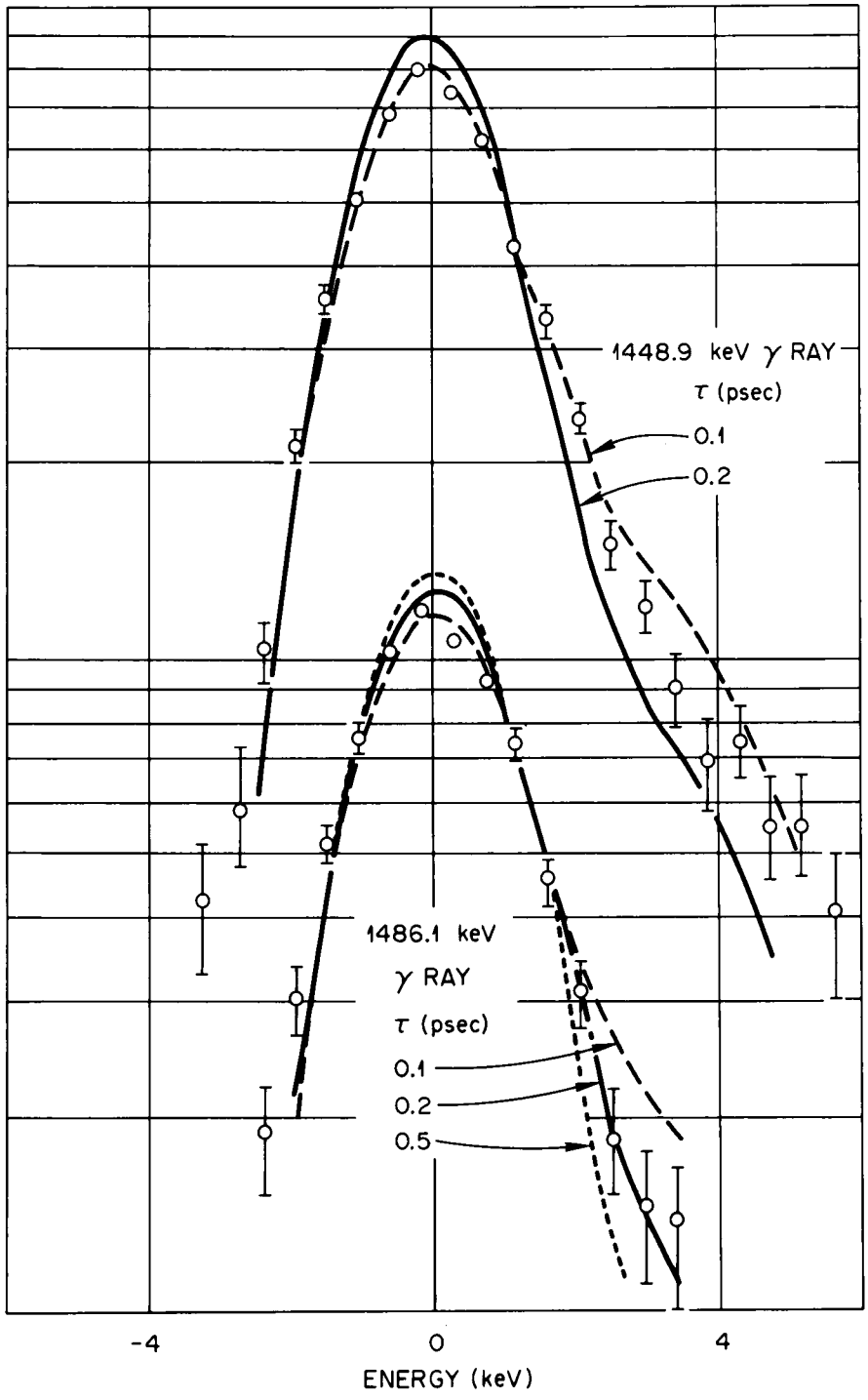


Figure 5-10. Doppler-broadened γ-ray peaks observed when ^{115}In was Coulomb excited with ^{4}He projectiles. The detector was located at 55° to the beam direction. The curves are calculated for different values for the mean-life, τ, in ps.

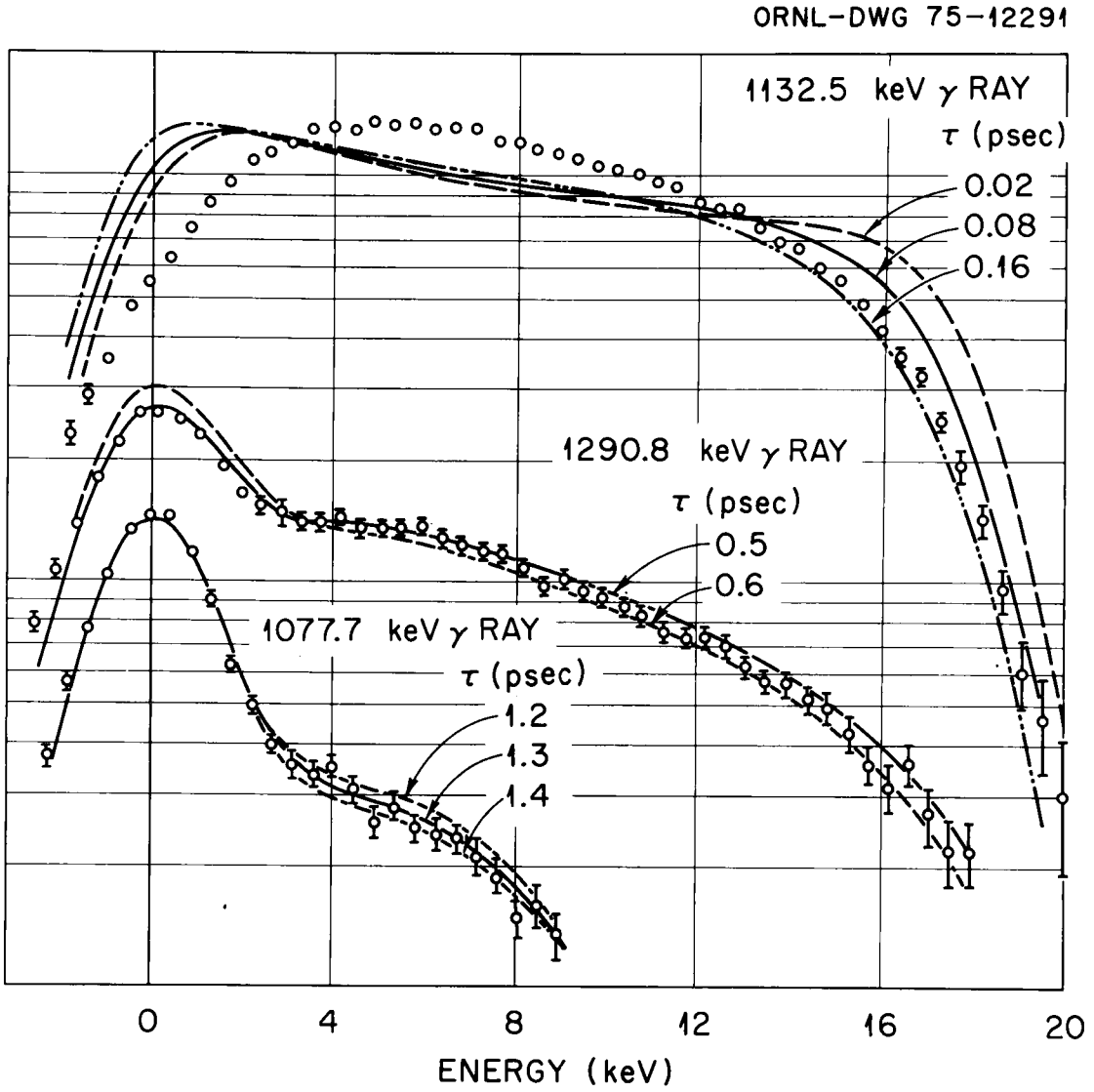


Figure 5-11. Doppler-broadened γ-ray peaks observed when ^{115}In was Coulomb excited with ^{16}O projectiles. The detector was located at 0° to the beam direction. The curves are calculated for different values for the mean-life, τ, in ps.

TABLE 5-5

Summary of information obtained from the Coulomb excitation of ^{113}In

Level (keV)	E_γ (keV)	Branching Ratio (%)	$(I^\pi)_i$	$(I^\pi)_f$	$B_d(E2)$ ($\times 10^{-50} e^2cm^4$)	$\frac{B_d(E2)}{B_{sp}(E2)^a}$	δ	$\frac{B_d(M1)}{(10^{-2}(\frac{e\hbar}{2Mc})^2)}$	$(\tau_{cal})_{mean}$ (psec)
1024.2	1024.2	91.0 ± 0.6	$5/2^+$	$9/2^+$	1.26 ± 0.10	3.9	∞	---	5.23 ± 0.42
	377.3	9.0 ± 0.6[b]	$5/2^+$	$3/2^-$	c	c	d	c	---
1131.7	1131.7	85.1 ± 0.5	$5/2^+$	$9/2^+$	2.67 ± 0.17	8.2	∞	---	1.40 ± 0.10
	484.8	14.0 ± 0.3	$5/2^+$	$3/2^-$	c	c	-0.03 ± 0.05[c]	c	---
						c	-3.0 ± 0.5[c]	c	---
	107.5	0.9 ± 0.2	$5/2^+$	$5/2^+$	d	d	$\lvert\delta\rvert \leq 0.3$[e]	d	---
1173.0	1173.0	100.	$11/2^+$	$9/2^+$	7.74 ± 0.47	23.8	+0.5 ± 0.2[f]	28 $^{+42}_{-13}$[f]	0.10 ± 0.06
1344.4	1344.4	97.9 ± 0.1	$13/2^+$	$9/2^+$	3.79 ± 0.23	11.7	∞	---	0.48 ± 0.04
	171.4	2.1 ± 0.1	$13/2^+$	$11/2^+$	2.89 ± 2.89	8.9	+0.03 ± 0.03	48 ± 3	---
1509.5	1509.5	93.5 ± 3.2	$7/2^+$[g]	$9/2^+$	1.81 ± 0.13	5.6	$-0.5\ ^{+0.2}_{-0.1}$	$12\ ^{+5}_{-3}$	$0.11\ ^{+0.04}_{-0.02}$
					---	---	-1.5 ± 0.1	1 ± 0.1	0.37 ± 0.04
	377.8	6.5 ± 3.2[b]	$7/2^+$[g]	$5/2^+$	d	d	d	d	---
1566.9	1566.9	87.5 ± 0.9	$9/2^+$[g]	$9/2^+$	1.78 ± 0.12	5.5	-1.5 ± 0.5	1.5 ± 0.5	0.29 ± 0.06
					---	---	$\lvert\delta\rvert \geq 5$	≤ 0.1	0.42 ± 0.03
	393.9	12.5 ± 0.9	$9/2^+$[g]	$11/2^+$	d	d	d	d	---
1630.7	1630.7	73.1 ± 4.8	$(9/2^+)$[g]	$9/2^+$	0.32 ± 0.12	1.0	$\geq +2.0$	≤ 1.4	$1.3\ ^{+0.4}_{-0.1}$
					---	---	$-0.8\ ^{-\infty}_{+0.4}$	$0.9\ ^{+2.8}_{-0.9}$	$0.65\ ^{+1.0}_{-0.4}$
	606.5	≤ 1.0	$(9/2^+)$[g]	$5/2^+$	d	d	d	---	---
	457.7	25.9 ± 4.8	$(9/2^+)$[g]	$11/2^+$	d	d	d	d	---

a) $B(E2)_{sp} = (e^2/4\pi)\ (3/5)^2(1.2\ fm)^4\ A^{4/3} = 32.5\ e^2fm^4$.

b) Result of taking $I_\gamma(377.8)/I_\gamma(1509.5) = 0.070 \pm 0.035$ based on ^{113}In coincidence data and ^{115}In analog state.

c) Spin-parity assignments require transition to be E1, M2, E3, or M4, and thus $\delta^2 = \lambda(M2)/\lambda(E1)$.

d) Not measured.

e) Requirement for $B_d(E2,107) \leq 100\ B_d(E2,1132)$.

f) Calculated using $\tau = 0.10 \pm 0.06$ psec.

g) Other spin-parity assignments allowed, see text for discussion.

TABLE 5-6

Summary of information obtained from the Coulomb excitation of ^{115}In

Level (keV)	E_γ (keV)	Branching Ratio (%)	$(I^\pi)_i$	$(I^\pi)_f$	$B_d(E2)$ ($\times 10^{-50} e^2cm^4$)	$\frac{B_d(E2)}{B_{sp}(E2)}$[a]	δ	$\frac{B_d(M1) \times 10^2}{(e\hbar/2Mc)^2}$	$(\tau_{cal})_{mean}$ (psec)
941.4	941.4	89.8 ± 0.4	$5/2^+$	$9/2^+$	0.45 ± 0.03	1.4 ± 0.1	∞	---	21.8 ± 2.0
	344.2	10.2 ± 0.4	$5/2^+$	$3/2^+$	b	b	-0.45 ± 0.30[b]	b	---
					b	b	-1.5 ± 0.8[b]	b	---
1077.7	1077.7	83.4 ± 0.4	$5/2^+$	$9/2^+$	3.78 ± 0.20	11.4 ± 0.6	∞	---	1.23 ± 0.07
	480.5	15.6 ± 0.2	$5/2^+$	$3/2^-$	b	b	-0.03 ± 0.05[b]	b	---
					b	b	-3.0 ± 0.5[b]	b	---
	136.3	1.0 ± 0.2	$5/2^+$	$5/2^+$	7^{+264}_{-7}	21^{+795}_{-21}	+0.07 ± 0.42	15^{+2}_{-4}	---
					≥ 271	≥ 816	$+1.5^{+3.0}_{-1.0}$	4^{+7}_{-4}	---
1132.5	1132.5	100	$11/2^+$	$9/2^+$	8.35 ± 0.43	25.2 ± 1.3	+0.50 ± 0.15[c]	30^{+53}_{-15}	0.10 ± 0.05
1290.8	1290.8	97.6 ± 0.1	$13/2^+$	$9/2^+$	4.04 ± 0.22	12.2 ± 0.7	∞	---	0.55 ± 0.04
	158.2	2.4 ± 0.1	$13/2^+$	$11/2^+$	$2.3^{+18.1}_{-2.3}$	$6.9^{+54.5}_{-6.9}$	+0.03 ± 0.05	64 ± 4	---
1448.9	1448.9	86.0 ± 0.3	$9/2^+$	$9/2^+$	1.51 ± 0.10	4.5 ± 0.3	$-8.0^{-\infty}_{+7.1}$	$0.03^{+2.7}_{-0.03}$	0.52 ± 0.20
	316.4	14.0 ± 0.3	$9/2^+$	$11/2^+$	5^{+158}_{-5}	15^{+476}_{-15}	$+0.1^{+0.2}_{-0.8}$	37^{+50}_{-12}	---
1463.5	1463.5	94.2 ± 0.4	$7/2^+$[d]	$9/2^+$	1.20 ± 0.17	3.6 ± 0.5	$-0.30^{-0.35}_{+0.15}$	20^{+60}_{-16}	$0.08^{+0.20}_{-0.06}$
							$-2.5^{-1.5}_{+1.0}$	0.5 ± 0.3	0.81 ± 0.15
	385.8	5.8 ± 0.4	$7/2^+$[d]	$5/2^+$	$1.7^{+356.0}_{-1.7}$	5^{+1072}_{-5}	-0.05 ± 0.40	70^{+193}_{-55}	---
1486.1	1486.1	78.7 ± 3.2	$9/2^+$	$9/2^+$	0.87 ± 0.09	2.6 ± 0.3	$-0.8^{-0.6}_{+0.5}$[e]	4^{+12}_{-2}[e]	0.4 ± 0.3
	544.7	3.7 ± 0.6	$9/2^+$	$5/2^+$	16^{+59}_{-7}	48^{+178}_{-21}	∞	---	---
	353.6	17.6 ± 1.2	$9/2^+$	$11/2^+$	289^{+2034}_{-272}	871^{+6127}_{-819}	+0.8 ± 0.6	26^{+236}_{-20}	---

a) $B_{sp}(E2) = e^2/4\pi)(315)^2(1.2\ fm)^4\ (A^{4\ 3}) = 33.2\ e^2fm^4$.

b) Spin-parity assignments require transition to be E1, M2, E3 or M4, and thus $\delta^2 = \lambda(M2)/\lambda(E1)$.

c) Obtained from $\tau_{meas.} = 0.10 \pm 0.05$ psec, see text for discussion.

d) Angular distributions also allow $I^\pi = 9/2^+$; see text for discussion.

e) Calculated from $\tau_{meas.} = 0.3 \pm 0.2$ psec.

2. DISCUSSION OF LEVEL PROPERTIES (COULOMB EXCITATION)

The 941.4 and 1077.7 keV Levels (^{115}In)

The observed branching to the 597.5 keV $3/2^-$ level and the fact that these states are populated by the E2 Coulomb excitation process strongly suggests they have $I^\pi = 5/2^+$. The angular distribution and lifetime measurements are consistent with these assignments, including the angular distribution of an observed 136.3 keV transition between the two. Unfortunately, the angular distribution measurement did not accurately determine the mixing ratio for this transition, but the value $\delta_{136} = +1.5^{+3.0}_{-1.0}$ can be eliminated because it would require $B_d(E2,\ 1078 \rightarrow 941) \geq 816$ single particle units (s.p.u.).

The 1132.5 and 1290.8 keV Levels (^{115}In)

For the 1290.8 keV level, the angular distributions allow $I^\pi = 7/2^+$ or $13/2^+$. However, for the $I^\pi = 7/2^+$ assignment, $\tau_{cal} = 0.31 \pm 0.02$ or 0.026 ± 0.011 psec which does not agree with the measured value of 0.55 ± 0.15 psec. Because for $I^\pi = 13/2^+$ $\tau_{cal} = 0.55 \pm 0.04$ psec, the spin-parity of the 1290.8 keV level is taken to be $13/2^+$.

From energy considerations, the 158.2 keV γ ray could be placed between the 1448.9 and 1290.8 keV levels, or between the 1290.8 and 1132.5 keV levels. The coincidence measurements rule out the former possibility. The angular distribution measurements for this transition yield a $\delta_{158} = 0.025 \pm 0.050$ or $-(10^{+10}_{-4})$. The latter assignment is rejected on the basis it requires $B_d(E2,\ 1291 \rightarrow 1132) \geq 10^4$ s.p.u.

The angular distribution measurements establish the spin-parity of the 1132.5 keV level as $7/2^+$, $9/2^+$ or $11/2^+$. An assignment of

$11/2^+$ is made because it is the only one consistent with the angular distribution of the 158.2 keV γ-ray feeding this level from the $13/2^+$ 1290.8 keV level. Since the $9/2^+$(E2) $11/2^+$(E2/M1) $9/2^+$ angular distribution is especially flat, the mixing ratio $\delta_{1132} = 0.5 \pm 0.2$ is determined from our lifetime measurement. This value is consistent with the angular distribution measurement where one standard deviation implies $+0.40 \leq \delta_{1132} \leq +5.0$.

The 1448.9 and 1486.1 keV Levels (^{115}In)

For the 1448.9 keV level, the angular distributions of the 1448.9 and 316.3 keV γ-rays favor a $I^\pi = 9/2^+$ assignment. The lifetime determination excludes a $\delta \geq +6.5$ for the 1448.9 keV γ ray because it requires $\tau_{1449} \tilde{=} 0.71 \pm 0.05$ psec in contrast to the measured value of $0.15^{+0.10}_{-0.05}$ psec. Unfortunately, the other δ allowed does not quite agree with the lifetime determination. However, because of a contaminent γ-ray, this lifetime had to be deduced from 55° data using α-particles to effect Coulomb excitation, making the determination somewhat tenuous. The other alternative is a $13/2^+$ fit to the angular distribution of the 1448.9 keV γ ray which is off by 1.2 standard deviations. However, this spin assignment can be eliminated since the τ value of 1.0 ± 0.1 psec deduced from the B_{ex}(E2) disagrees significantly from the measured value.

For the 1486.1 keV level, our angular distributions of the 1486.1 and 353.6 keV γ rays allow only $I^\pi = 9/2^+$, and give a δ_{1486} of $-(0.95^{+\infty}_{-0.35})$ or $+7.5^{+\infty}_{-5.0}$. The latter assignment is eliminated by the lifetime determination of 0.3 ± 0.2 psec. In the summary table a mixing ratio and B_d(M1) was calculated on the basis of this lifetime.

The 1463.5 keV Level (^{115}In)

The angular distributions of the ground state transition give $I^{\pi} = 7/2^{+}$ or $9/2^{+}$. The $7/2^{+}$ assignment is suggested because of the angular distribution of the branching 385.8 keV γ ray from this level and because there is no observed branching to the $11/2^{+}$ 1132.5 keV level in contrast to two other $9/2^{+}$ states in this energy region. Furthermore, a $9/2^{+}$ assignment to the 1463.5 keV level would require $B_d(E2, 1464 \rightarrow 1078) \geq 500$ s.p.u. A direct lifetime determination could not be made.

The 1024.2 and 1131.7 keV Levels (^{113}In)

The observed branching to the 646.9 keV $3/2^{-}$ level, and the fact these states are populated by the E2 Coulomb excitation process strongly suggests that these levels have $I^{\pi} = 5/2^{+}$. For the 1024.2 keV, the angular distribution and lifetime measurements are consistent only with this assignment. The 377.3 keV branch from this level cannot be directly resolved from the 377.8 keV branch of the 1509.5 keV level. To determine the strength of the 377.8 keV transition, a branching of (6.5 ± 3.2)% for the 377.8 keV γ ray from the 1509.5 keV level was first deduced from the ^{113}In coincidence measurements. This is similar to the analogous one in ^{115}In. Next, from the intensity of the 1509.5 keV γ ray, the content of the 377.8 keV transition in the 377 keV peak was determined to be 21 ± 10%. This information was then used in calculating the $B_{ex}(E2)$ for the 1024.2 and 1509.5 keV levels.

Since about 23% of the counts in the 1132 keV peak are due to the 1132.5 keV $11/2^{+}$ state in ^{115}In, the angular distribution measurement was difficult, and the lifetime measurement impossible. The result

of the angular distribution measurement was, however, consistent with the $5/2^+$ assignment of this level.

The observation of a 105.7 keV γ-ray transition between the levels is also consistent with the spin-parity assignments.

The 1173.0 and 1344.4 keV Levels (^{113}In)

For the 1344.4 keV level, the angular distributions give $I^\pi = 7/2^+$ or $13/2^+$, and the lifetime measurement eliminates the $7/2^+$ assignment. For the 1173.0 keV level, our angular distributions are consistent with an $I^\pi = 7/2^+$, $9/2^+$, or $11/2^+$ assignment. However, the angular distribution of the 171.4 keV γ-ray connecting the two levels permits only an $11/2^+$ assignment for the 1173.0 keV level. Like the ^{115}In analog, the mixing ratio must be taken from the lifetime measurement because of the flatness of the $9/2^+(E2)11/2^+$ $(E2/M1)9/2^+$ distribution.

The 1509.5, 1566.9 and 1630.7 keV Levels (^{113}In)

The angular distribution measurements for the 1509.5 and 1566.9 keV γ rays allow spin-parity assignments of $7/2^+$ or $9/2^+$ for both levels. These assignments cannot be resolved by the lifetime determination. Furthermore, experimental difficulties precluded angular distribution measurements for branching γ rays from these levels. Thus, the assignment of $I^\pi = 7/2^+$ for the 1509.5 keV level is based on the observation of the 377.8 keV branch to the $5/2^+$ 1132.5 keV level and on the analogy with ^{115}In. Similarly, the assignment of $I^\pi = 9/2^+$ for the 1566.9 keV level is based on the observation of a 393.9 keV branch to the $11/2^+$ 1173.0 keV level and on the analogy with ^{115}In.

The assignment $I^{\pi}(1630.7\ keV) = 9/2^{+}$ is based on analogy with ^{115}In.

3. RESULTS FROM $^{110}Pd(^{6}Li,3n)^{113}In$

Level Diagram

The level diagram of states in ^{113}In that are observed in the $^{110}Pd(^{6}Li,3n)^{113}In$ reaction is displayed in Figures 5-12, 5-13 and 5-14. This diagram was constructed from the yield, angular distribution, and coincidence information. The widths of arrows are proportional to the intensity (I) of the transitions. The numbers in parentheses associated with each arrow are the intensities at 55° normalized to I(1344.4 keV) = 100.0. Not shown are known transitions from levels at 1024.2, 1131.7, 1566.7, and 1630.7 keV for which no definite coincident γ rays could be found. The rationale for the spin assignments given will be discussed in Section 4.

Coincidence Information

The coincidence information obtained in the $^{110}Pd(^{6}Li,3n)^{113}In$ experiment is displayed in Table 5-7. The intensity information is the average of that seen in both the "X" and "Y" directions. The error associated with the intensity is qualitative only as discussed in Chapter 4, Section 5. There is, in some cases, an additional error which reflects pronounced angular distribution effects resulting from coincidences between stretched $\ell = 1$ and $\ell = 2$ transitions.

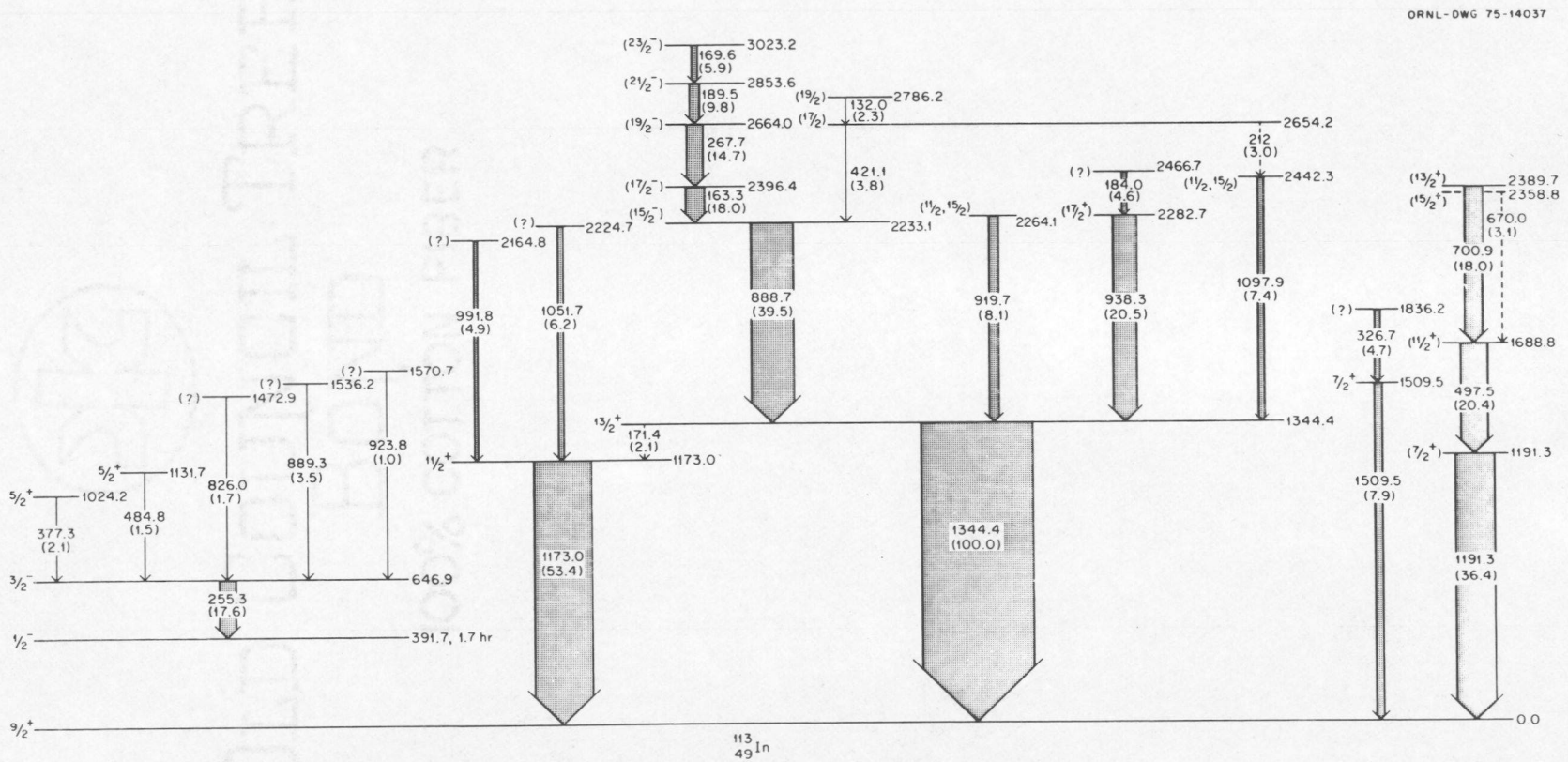


Figure 5-12. Level diagram of all states in ^{113}In as observed in the ^{110}Pd(^{6}Li,3n)^{113}In reaction except these known levels for which no feeding could be established. Widths of arrows are proportional to the yield at 55° normalized to that of the 1344.4 keV transition.

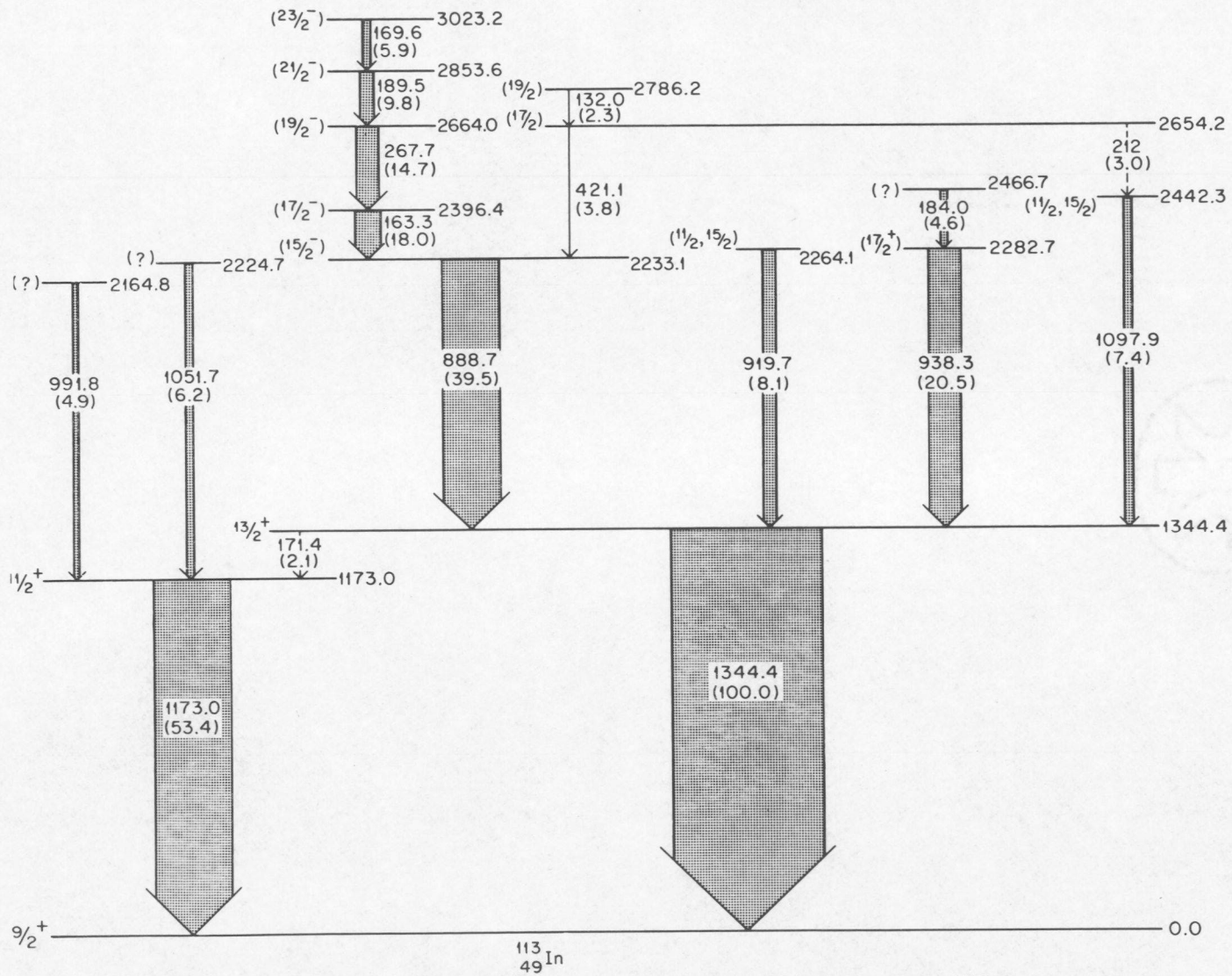


Figure 5-13. Level diagram of states observed in the $^{110}Pd(^{6}Li,3n)^{113}In$ reaction to feed the $11/2^{+}$ 1173.0 keV and $13/2^{+}$ 1344.4 keV levels. The notation is the same as for Figure 5-12.

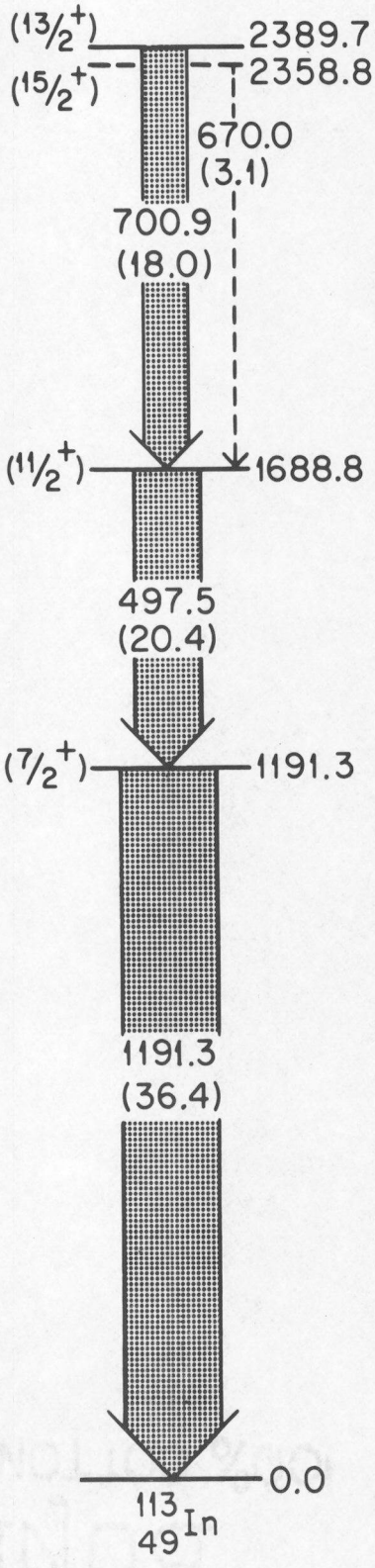


Figure 5-14. Level diagram of states in ^{113}In observed in the ^{110}Pd(^{6}Li,3n)^{113}In reaction which do not feed any of the states observed in the Coulomb excitation reaction.

TABLE 5-7

Summary of coincidence information obtained from the $^{110}Pd(^{6}Li,3n)^{113}In$ Reaction

Transition Energy (keV)	Coincident γ-Rays (keV) and Relative Intensities: Definite	Possible
91	184.0 (0.6 ± 0.1), 189.5 (0.8 ± 0.2)[a], 191.7 (1.0 ± 0.1)[b]	81 (0.4 ± 0.4)[a], 267.7 (0.6 ± 0.6)[a], 919.7 (0.4 ± 0.4)[b] 923.8 (0.6 ± 0.6)[b], 938.3 (0.8 ± 0.2)[a]
123.0	374 (0.6 ± 0.3)	189.5 (0.6 ± 0.3), 255.3 (0.4 ± 0.1)[a]. 547.5 (0.3± 0.1) 1401 (0.9 ± 0.2)[a]
132.0	81 (0.5 ± 0.1)[a], 169.6 (0.5 ± 0.1)[b], 191.7 (0.4 ± 0.2), 421.1 (0.7 ± 0.1), 888.7 (0.8 ± 0.2), 1344.4 (1.2 ± 0.8)	70 (0.4 ± 0.1)[b], 212 (0.1 ± 0.1), 938.3 (0.2 ± 0.1)[b]
163.3	169.6 (3.3 ± 0.5), 189.5 (5.0 ± 1.0), 198.7 (2.6 ± 1.0), 267.7 (13.5 ± 1.5) 389.1 (3.3 ± 1.0), 888.7 (22.1 ± 2.5), 1344.4 (26.3 ± 8.2)	212 (0.7 ± 0.2), 255.3 (1.1 ± 0.3)
169.6	105.5 (1.2 ± 0.2)[b], 142.6 (0.5 ± 0.2)[b], 163.3 (3.0 ± 1.0), 189.5 (1.9 ± 0.9) 198.7 (1.3 ± 0.4)[b], 245.4 (3.7 ± 2.4), 255.3 (1.5 ± 0.5), 267.7 (2.5 ± 0.7) 377.4 (4.0 ± 1.5), 389.1 (0.6 ± 0.1)[a], 414 (1.3 ± 0.5), 888.7 (3.7 ± 2.0), 1344.4 (3.4 ± 1.0)	70 (0.6 ± 0.3)[b], 132.0 (0.1 ± 0.1)[a], 169.6 (0.3 ± 0.3)[a] 374 (0.5 ± 0.1)[a]
184.0	91 (0.5 ± 0.3), 938.3 (2.4 ± 0.5), 1344.4 (1.2 ± 0.6)	70 (0.3 ± 0.3), 169.6 (0.2 ± 0.2)[a], 374 (0.2 ± 0.2)[a] 391.9 (0.6 ± 0.4)
189.5	81 (4.0 ± 1.5), 91 (0.8 ± 0.3), 123.0 (1.2 ± 0.4), 163.3 (4.4 ± 0.5), 169.6 (1.8 ± 0.3), 178.5 (0.8 ± 0.2)[a], 258 (1.7 ± 0.5), 267.6 (4.6 ± 0.5), 474 (1.4 ± 0.7), 888.7 (4.3 ± 0.5), 1344.4 (5.0 ± 2.3)	110.3 (0.8 ± 0.4), 132.0 (0.7 ± 0.3), 374 (0.6 ± 0.2)[a] 397 (0.9 ± 0.3)[a], 617.7 (0.9 ± 0.3)[a]
198.7	105.5 (4.7 ± 1.4), 163.3 (1.0 ± 0.3), 166 (3.0 ± 0.5), 236.0 (1.4 ± 0.7) 267.7 (1.8 ± 0.6), 287 (1.0 ± 0.2)	70 (0.7 ± 0.3)[b], 123.0 (0.4 ± 0.4)[b], 222 (0.6 ± 0.2) 377.4 (0.8 ± 0.8)[b], 421.1 (0.5 ± 0.3)[b], 1344.4 (1.0 ± 0.6)[b]
255.3	169.6 (1.7 ± 0.2), 189.5 (1.2 ± 0.4), 267.7 (1.5 ± 0.3), 332 (1.7 ± 0.8), 377.4 (1.6 ± 0.2), 459 (1.3 ± 0.5), 484.8 (0.9 ± 0.3), 825 (2.2 ± 0.3), 888.7 (2.4 ± 0.3), 924 (1.1 ± 0.2)	123.0 (0.5 ± 0.3)[b], 163.3 (0.9 ± 0.3), 196 (0.4 ± 0.2)[a]

TABLE 5-7 (continued)

Transition Energy (keV)	Coincident γ-Rays (keV) and Relative Intensities	
	Definite	Possible
267.6	163.3 (13.5 ± 1.5), 169.6 (2.7 ± 0.2), 189.5 (5.2 ± 0.3), 198.7 (1.4 ± 0.2) 255.3 (1.1 ± 0.2), 267.7 (0.8 ± 0.2)[b], 387 (1.3 ± 0.5), 888.7 (14.5 ± 1.0) 1344.4 (14.0 ± 1.6)	153.0 (0.5 ± 0.4), 236.0 (0.7 ± 0.3)[b], 526.3 (1.4 ± 0.4)[b] 94 (0.6 ± 0.2)[b]
326	1509.5 (2.3 ± 0.7)	110.3 (0.3 ± 0.3)[b], 184.0 (0.2 ± 0.2)[b], 191.7 (0.4 ± 0.2) 212 (0.3 ± 0.1), 1228 (1.0 ± 1.0)[a]
377.4	169.6 (4.0 ± 0.5), 236.0 (1.3 ± 0.2), 255.3 (2.1 ± 0.3), 710 (1.3 ± 0.3)	110.3 (0.3 ± 0.3)[a], 146.5 (0.4 ± 0.2), 163.3 (0.4 ± 0.1)[b] 374 (0.6 ± 0.6), 414 (0.9 ± 0.4)
414	70 (2.0 ± 0.7), 169.6 (1.5 ± 0.3), 377.4 (1.2 ± 1.0), 414 (7.0 ± 0.7)	391.9 (1.4 ± 0.6)
421.1	132.0 (0.8 ± 0.1), 888.7 (2.2 ± 0.3), 1344.4 (2.8 ± 1.2)	171.4 (0.2 ± 0.1), 198.7 (0.3 ± 0.2)[a], 227 (0.5 ± 0.2) 391.4 (0.6 ± 0.5)[a], 991.8 (0.5 ± 0.2)[b], 1068 (1.0 ± 1.0)[b]
497.5	670.0 (2.2 ± 1.1), 700.9 (6.0 ± 0.6), 1191.3 (19.3 ± 1.3)	673.5 (0.5 ± 0.2)[a]
670.0	497.5 (1.5 ± 0.9), 1191.3 (2.6 ± 1.2)	258 (0.3 ± 0.2)[b], 391.4 (0.6 ± 0.1)[b], 421.1 (0.4 ± 0.3)
673.5	1191.3 (2.8 ± 0.7)	163.3 (0.4 ± 0.4)[b], 258 (0.3 ± 0.3)[b], 492 (1.2 ± 0.4)[a] 654 (0.5 ± 0.5)[a]
700.9	497.5 (5.3 ± 0.9), 1191.3 (5.8 ± 1.8)	166 (0.1 ± 0.1)[a], 391.4 (0.4 ± 0.2)[a]
825	255.3 (0.9 ± 0.1)	
888.7	163.3 (26.0 ± 4.0), 169.6 (5.3 ± 0.4), 189.5 (5.8 ± 1.0), 255.3 (2.5 ± 0.5) 267.7 (16.0 ± 2.0), 389.1 (4.0 ± 0.6), 421.1 (2.9 ± 0.5), 1344.4 (43.0 ± 7.0)	132.0 (1.3 ± 0.2)[b], 198.7 (0.8 ± 0.8)[b], 1068 (3.0 ± 1.0)[a] 1356 (4.0 ± 2.0)[b]
919.7	1344.4 (6.7 ± 2.9)	163.3 (0.3 ± 0.3)[a], 169.6 (0.3 ± 0.3)[b], 251 (0.3 ± 0.3)[b] 317 (0.4 ± 0.4)[a], 1004 (1.0 ± 0.7)[b]
924	255.3 (1.1 ± 0.3)	391.4 (0.4 ± 0.4)[a]

TABLE 5-7 (continued)

Transition Energy (keV)	Coincident γ-Rays (keV) and Relative Intensities: Definite	Possible
938.3	90 (0.5 ± 0.1)[b], 184.0 (2.8 ± 0.5), 548 (1.0 ± 0.5)[a], 787 (2.0 ± 1.0)[b] 1344.4 (12.0 ± 2.0)	129 (0.2 ± 0.1)[b], 191.7 (0.2 ± 0.2)[a], 359 (0.6 ± 0.6)[b] 391.4 (0.6 ± 0.6)[a], 476 (0.7 ± 0.7)[b], 502 (1.4 ± 0.4)[a] 1024.2 (0.8 ± 0.8), 1191.3 (0.9 ± 0.9)[a]
991.8	1173.0 (3.9 ± 1.8)	284 (0.2 ± 0.2)[b], 787 (0.9 ± 0.6)[b]
1051.7	1173.0 (4.2 ± 0.7)	596 (0.6 ± 0.6)[a]
1098.0	1344.4 (6.8 ± 3.6)	212 (0.6 ± 0.4)
1173.0	163.3 (1.2 ± 0.5)[b], 171.4 (1.1 ± 0.6), 991.8 (3.9 ± 1.8), 1051.7 (6.7 ± 0.7)	267.7 (1.3 ± 0.3)[b], 391.4 (1.4 ± 0.4)[b], 455 (2.7 ± 0.2)[b] 1173.0 (5.9 ± 1.0), 1191.3 (3.0 ± 1.0)[b]
1191.3	497.5 (19.0 ± 1.5), 700.9 (5.8 ± 1.1)	374 (1.5 ± 0.6)[b], 492 (1.5 ± 0.9), 670.0 (2.2 ± 0.9) 673.5 (2.6 ± 0.6)
1344.4	132.0 (0.9 ± 0.5), 163.3 (14.0 ± 4.2), 169.6 (2.6 ± 0.8), 189.5 (4.6 ± 0.2)[b] 191.7 (1.9 ± 0.3)[a], 267.7 (13.0 ± 1.5), 888.7 (38.8 ± 11.4), 919.7 (6.1± 3.4) 938.3 (10.8 ± 1.3), 1098.0 (6.6 ± 3.4)	70 (0.6 ± 0.3)[a], 90 (0.4 ± 0.1)[b], 184.0 (0.9 ± 0.3)[b] 421.1 (3.0 ± 0.9), 526 (2.0 ± 1.0)[b]
1509.5	326 (2.9 ± 0.3)	

Relative Intensities are given in parenthesis. Unless otherwise noted, they are the average of the results obtained with gates in both the "x" and "y" directions.

[a]Coincidence observed with gate in "x" direction only.

[b]Coincidence observed with gate in "y" direction only.

Angular Distributions

The results of the angular distribution measurements are displayed in Table 5-8. The errors associated with the data are for the most part qualitative, except for those isolated peaks which could be stripped by hand. Only those γ-rays for which meaningful data could be extracted are displayed.

The γ-Ray Yields

In order to place transitions in the level diagram, the angular distribution measurement at 55° was used to obtain the relative yields of the γ rays of interest. The γ rays of 1024.2, 1131.7, 1566.7 and 1630.7 keV had yields of 21%, 10%, 9% and 8% relative to the 1344.4 keV transition, but were not placed in the level diagram as discussed earlier. The spectra observed is shown in Figures 5-15, 5-16, 5-17, and 5-18. This spectra is the sum of all four angular distributions.

DCO Information

The DCO information obtained for the main cascade is displayed in Table 5-9, while this information for other γ-rays of interest is displayed in Table 5-10. As with the coincidence information, the error associated with each number is qualitative only. This information is intended as a qualitative supplement to the angular distribution data.

TABLE 5-8

Angular distribution coefficients obtained from the $^{110}Pd(^{6}Li,3n)^{113}In$ reaction

E_γ(keV)	A_2^{ex}	A_4^{ex}
132.0	-0.052 ± 0.034	-0.109 ± 0.040
163.3	-0.259 ± 0.044	+0.027 ± 0.051
169.5	-0.142 ± 0.128	-0.010 ± 0.107
184.0	+0.095 ± 0.129	-0.115 ± 0.156
189.5	-0.024 ± 0.049	-0.052 ± 0.059
267.7	-0.065 ± 0.061	-0.075 ± 0.081
421.1	-0.129 ± 0.152	-0.043 ± 0.179
497.5	+0.143 ± 0.022	-0.078 ± 0.027
700.9	+0.159 ± 0.047	+0.154 ± 0.059
888.7	-0.228 ± 0.064	+0.002 ± 0.078
938.3	+0.267 ± 0.068	-0.071 ± 0.090
1024.2	+0.106 ± 0.071	-0.078 ± 0.090
1097.9	-0.264 ± 0.104	-0.040 ± 0.137
1131.7	+0.114 ± 0.070	-0.104 ± 0.086
1173.0	+0.266 ± 0.053	-0.018 ± 0.063
1191.3	-0.016 ± 0.040	+0.017 ± 0.053
1344.4	+0.191 ± 0.015	-0.010 ± 0.019

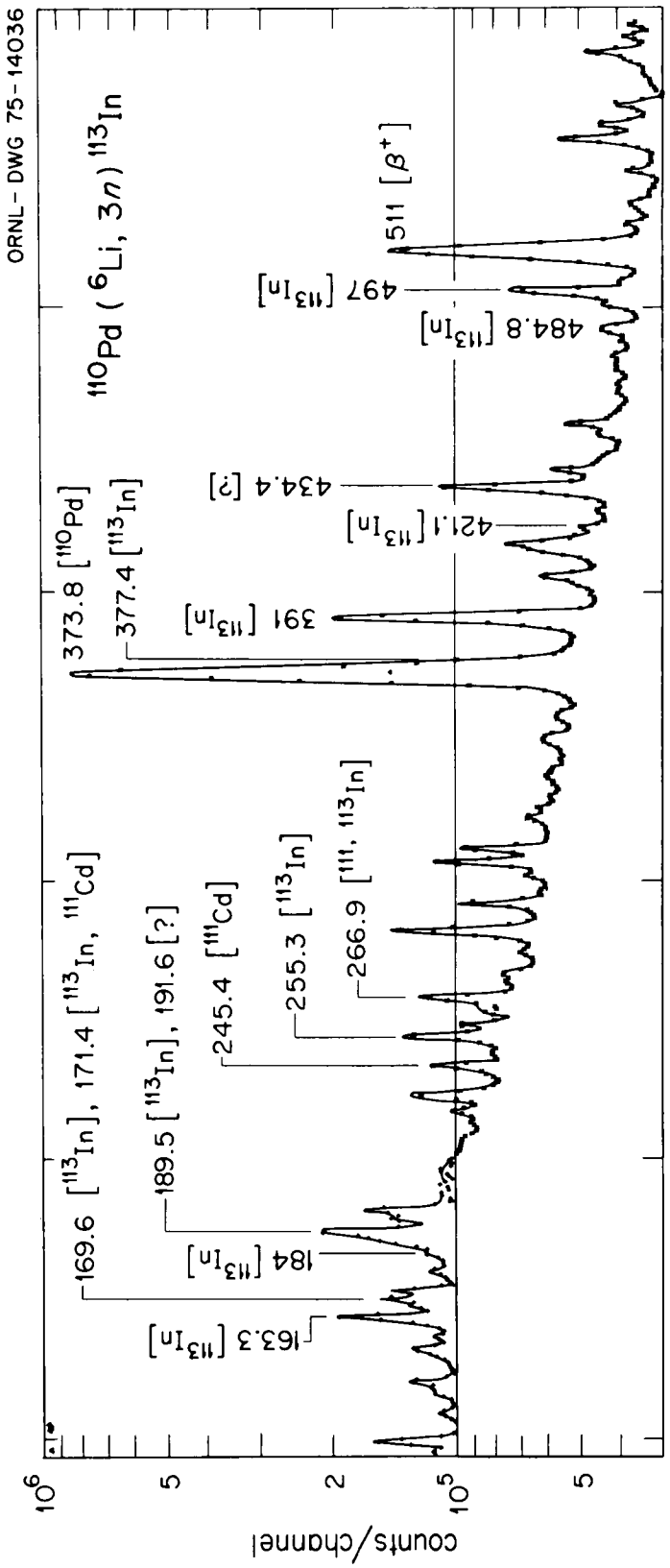


Figure 5-15. Ge(Li) pulse-height spectrum of the 121 to 583 keV γ rays from an enriched ^{110}Pd target bombarded with 24 MeV ^{6}Li ions.

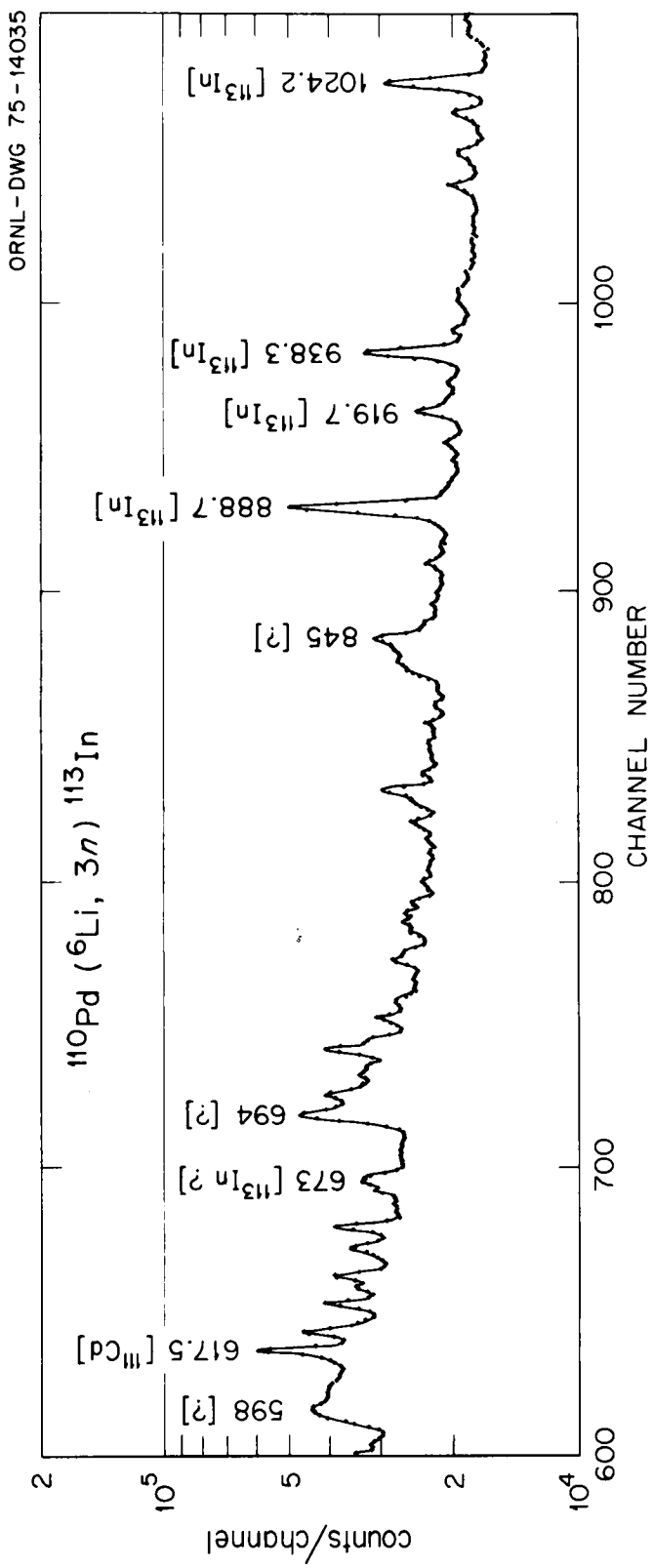


Figure 5-16. Ge(Li) pulse-height spectrum of the 583 to 1046 keV γ rays from an enriched ^{110}Pd target bombarded with 24 MeV ^{6}Li ions.

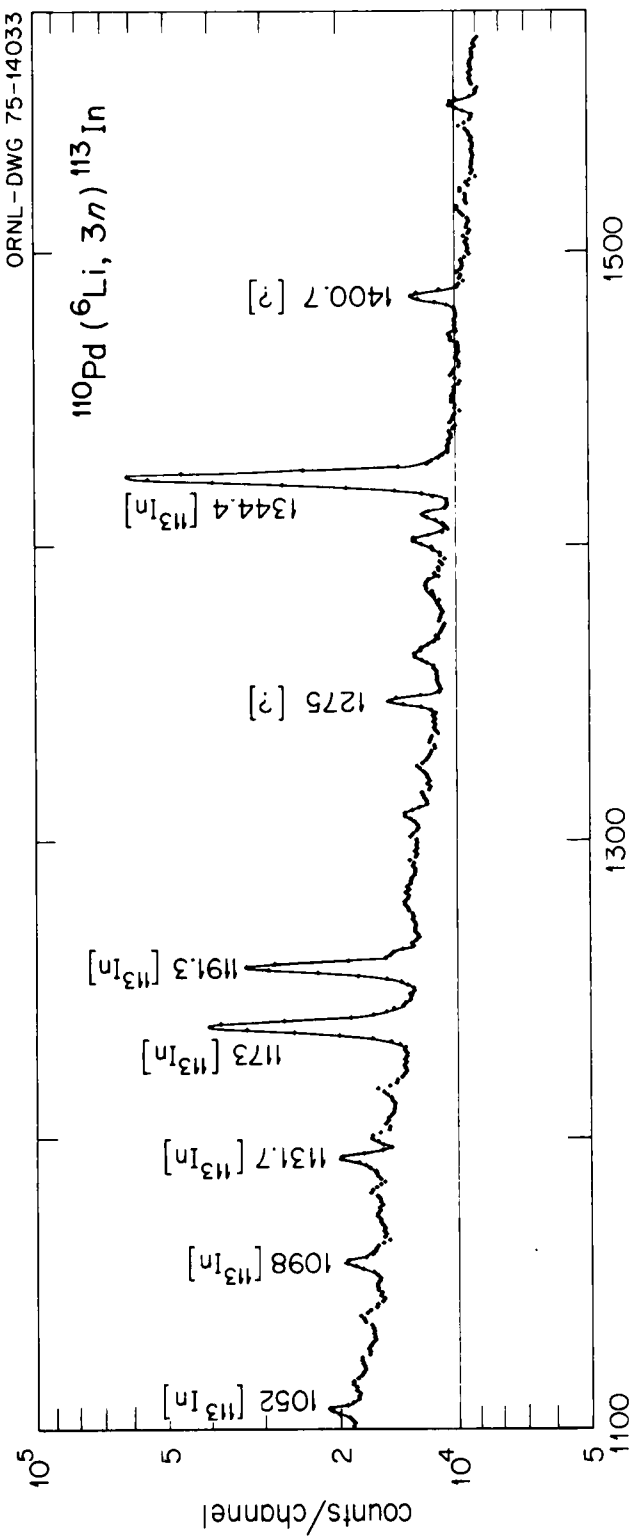


Figure 5-17. Ge(Li) pulse-height spectrum of the 1046 to 1483 keV γ rays from an enriched ^{110}Pd target bombarded with 24 MeV ^{6}Li ions.

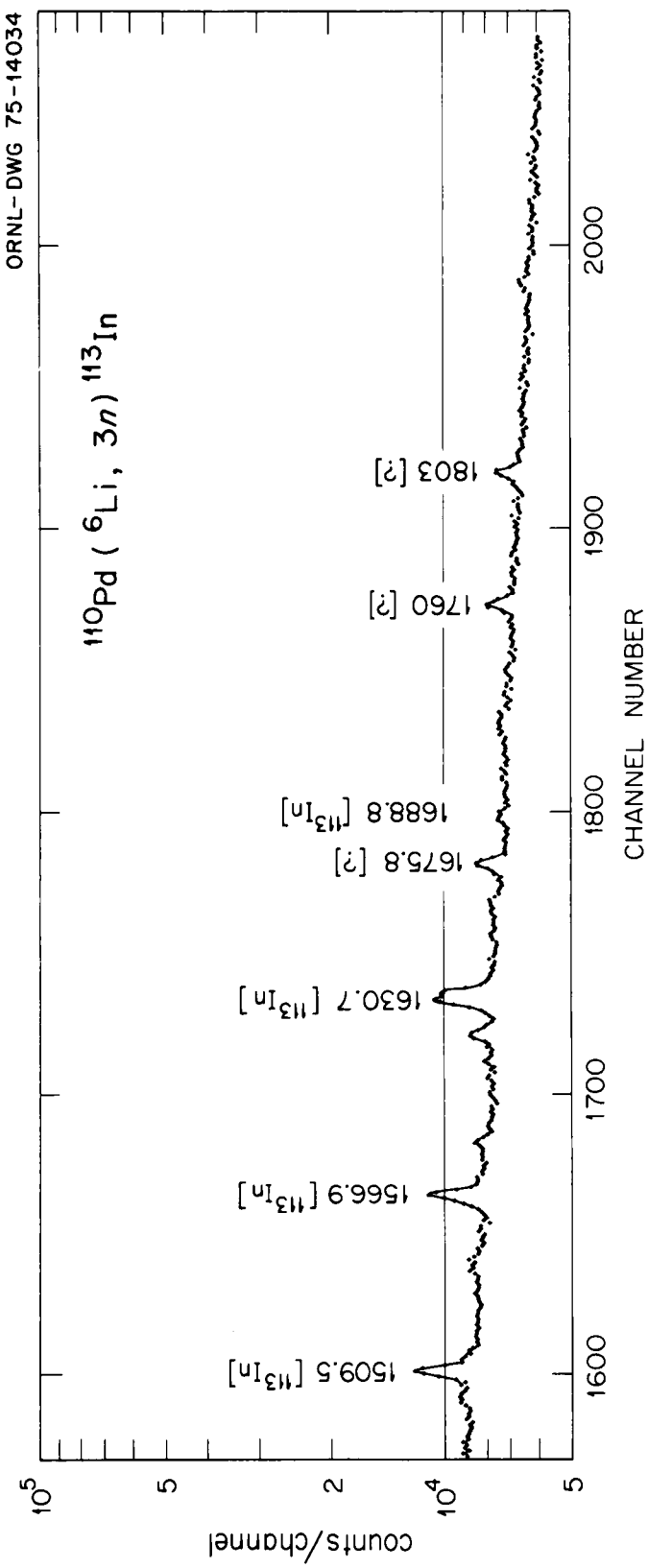


Figure 5-18. Ge(Li) pulse-height spectrum of the 1483 to 1954 keV γ rays from an enriched ^{110}Pd target bombarded with 24 MeV ^{6}Li ions.

TABLE 5-9

Table of $R_{\gamma_1-\gamma_2}$ (90°,22°) for the strongest cascade observed in the $^{110}Pd(^{6}Li,3n)^{113}In$ reaction

γ_1 (keV) \ γ_2 (keV)	1344.4	888.7	163.3	267.7	189.5
888.7	1.6 ± 0.1				
163.3	1.9 ± 0.2	1.2 ± 0.1			
267.7	1.6 ± 0.2	1.1 ± 0.1	0.8 ± 0.1		
189.5	2.5 ± 0.4	1.0 ± 0.2	0.8 ± 0.2	1.1 ± 0.1	
169.6	2.0 ± 0.7	0.6 ± 0.1	0.8 ± 0.1	0.8 ± 0.1	0.8 ± 0.3

TABLE 5-10

Table of $R_{\gamma_1-\gamma_2}$ (90°,22°) for the $^{110}Pd(^{6}Li,3n)^{113}In$ Reaction

γ_1 (keV)	γ_2 (keV)	$R_{\gamma_1-\gamma_2}$ (90°,22°)
132.0	421.1	1.3 ± 0.3
132.0	1344.4	3.8 ± 3.8
184.0	938.3	0.8 ± 0.2
421.1	888.7	1.3 ± 0.3
421.1	1344.4	2.6 ± 0.8
497.5	670.0	3.6 ± 1.8
497.5	700.9	1.2 ± 0.2
497.5	1191.3	0.9 ± 0.1
670.0	1191.3	2.4 ± 0.9
700.9	1191.3	0.6 ± 0.1
919.7	1344.4	2.1 ± 1.1
938.3	1344.4	0.8 ± 0.1
1097.9	1344.4	3.2 ± 2.1

4. DISCUSSION OF LEVEL PROPERTIES (^{110}Pd(^{6}Li,3n)^{113}In)

States also Observed in Coulomb Excitation

All the states seen in the Coulomb excitation reaction were also observed in the ^{110}Pd(^{6}Li,3n)^{113}In reaction.

1024.2 keV level. The spin-parity of this level is known to be $5/2^+$. The angular distribution measurements are consistent with this assignment, yielding the values $\alpha_2 = +0.53 \pm 0.36$ and $\alpha_4 = +5.7 \pm 6.5$ which are a consistent set. Because of the relatively weak population of states known to feed this level, transitions from them to this level were not observed in the coincidence measurements.

1131.7 keV level. The spin-parity of this level is known to be $5/2^+$. The angular distribution measurement of the ground-state transition is, to first order, consistent with this assignment yielding the values $\alpha_2 = +0.57 \pm 0.35$ and $\alpha_4 = +7.9 \pm 6.5$. The α_4 value is not consistent due to a large negative A_4^{ex} value. However, A_4^{ex} values are more difficult than A_2^{ex} values to determine precisely, and considering the large error, the agreement is reasonable. For reasons as given in the 1024.2 keV level discussion, no known transitions feeding this level were observed in the coincidence measurement.

1173.0 keV level. The spin-parity of this level is known to be $11/2^+$ (with the ground-state transition having a $\delta_{1173} = +0.5 \pm 0.2$). The angular distribution measurement of this ground-state transition was consistent with this assignment, yielding the values $\alpha_2 = +0.48^{+0.48}_{-0.12}$ and $\alpha_4 = -0.15 \pm 0.56$, which are a consistent set. The known 171.4 keV

keV transition feeding this level from the $13/2^+$ 1344.4 keV level was observed in the coincidence measurement. At 0°, the 1173.0 keV γ ray showed some Doppler broadening which is consistent with the known lifetime of the level ($\tau = +0.10 \pm 0.06$ ps).

1344.4 keV level. The spin-parity of this level is known to be $13/2^+$. The angular distribution measurement of the ground-state transition was consistent with this assignment, yielding the values $\alpha_2 = +0.44 \pm 0.04$ and $\alpha_4 = +0.05 \pm 0.10$ which are a consistent set.

1509.5, 1566.9, and 1630.7 keV levels. Experimental difficulties precluded the measurement of angular distributions of ground-state transitions from these levels. A ray of 326.7 keV was found to feed the 1509.5 keV level. Looking back at the Coulomb excitation data, there is evidence for a 327 keV γ ray and a possible 1836 keV γ ray. The γ ray at 1630.7 keV is part of a doublet for which there is some evidence in the Coulomb excitation coincidence data.

States Feeding the $13/2^+$ 1344.4 keV Level

2233.1 keV level. The 888.7 keV γ ray from this level is the strongest transition feeding the 1344.4 keV level. The angular distribution of this γ ray supports $\Delta\ell = 1$ although $\Delta\ell = 0$ is allowed, and there is a 7% contamination due to a transition of the same energy to the $3/2^-$ 646.9 keV level. The preferred assignment of $1^\pi = 15/2^-$ is made on the basis of the DCO ratio and the lack of an observed transition to the $11/2^+$ 1173.0 keV level.

3296.4 keV level. The strongest γ ray feeding the 2233.1 keV level is a 163.3 keV transition from the 2396.4 keV level. Angular distribution measurements support only $\Delta\ell = 1$. An assignment of $1^{\pi} = 17/2^{-}$ is preferred on the basis of this and the DCO measurements.

2664.0 keV level. A transition of 267.7 keV connects this level to the 2396.4 keV level. The angular distribution measurement was not definitive. Additionally, it is contaminated by 5% with the 267 keV $3/2^{-}$ to $1/2^{-}$ transition in ^{111}In. The preferred assignment is $19/2^{-}$ based upon DCO ratios and systematics of the cascade.

2853.6 keV level. A transition of 189.5 keV connects this level to the 2664.0 keV level. The angular distribution measurement of this γ ray was also not definitive, but the DCO measurements suggest a stretched $\Delta\ell = 1$ transition. Thus the preferred assignment of $I^{\pi} = 21/2^{-}$.

3023.2 keV level. A transition of 169.6 keV connects this level with the 2853.6 keV level. The angular distribution and yield measurements are complicated by the presence of a 171.4 keV transition in ^{113}In and in ^{111}Cd. However these distributions do support a $\Delta\ell = 1$ assignment which is also consistent with the DCO measurements. Thus the tentative $I^{\pi} = 23/2^{-}$ assignment.

2654.1 keV level. A γ ray of 421.1 keV connects this level with the 2233.1 keV level. The angular distributions suggest $\Delta\ell = 1$, but the errors are too great to rule out other possibilities. DCO measurements suggest a stretched $\Delta\ell = 1$, so $I = 17/2$ is preferred for this level.

2786.2 keV level. A γ ray of 132.0 keV connects this level with the 2654.1 keV level. Angular distribution and DCO measurements suggest $\Delta\ell = 1$, but other possibilities are not ruled out. An assignment of I = 19/2 is preferred.

2264.1 keV level. Experimental difficulties precluded the measurement of angular distributions for the 919.7 keV γ-ray connecting this level to the 1344.4 keV level. The DCO ratio suggests $\Delta\ell = 1$, but this is highly tenative.

2282.7 keV level. A γ ray of 938.3 keV connects this level with the 1344.4 keV level. It is the second strongest γ ray feeding that level. The angular distribution of this γ ray is consistent with $\Delta\ell = 2$. Since the DCO ratio is 0.8 ± 0.1, an assignment of $I^{\pi} = 17/2^{+}$ is preferred for this level. Using this assignment, the angular distribution of the 938.3 keV γ-ray yields the consistent values $\alpha_2 = 0.65 \pm 0.18$ and $\alpha_4 = 0.41 \pm 0.51$.

2466.7 keV level. A 184.0 keV γ ray connects this level with the 2282.7 keV level. Because of large errors, the angular distributions fit any assignment, although $\Delta\ell = 2$ is the best fit. This is in contrast to the DCO values which slightly suggest a stretched $\Delta\ell = 1$. Thus no assignment can be made.

2442.3 keV level. The 1097.9 keV γ ray which connects this level with the 1344.4 keV level has an angular distribution which suggests $\Delta\ell = 1$, although $\Delta\ell = 0$ cannot be eliminated. However, the DCO value

of 3.2 ± 2.1 suggests that $\Delta\ell = 1$ is the proper assignment. Thus an assignment $I = 15/2^+$ is suggested.

The 700.9, 497.5, 1191.3 keV Cascade

A strong cascade of γ rays proceeding (weakest to strongest) from 700.9 keV to 497.5 keV to 1191.3 keV was observed in this work. There were no coincident γ rays found between this cascade and γ rays seen in the Coulomb excitation study.

1191.3 keV level. A state of this energy has been assigned to ^{113}In from two experiments. Markham and Fulbright[34] observe a level here in their transfer study work, and prefer the assignment $I^\pi = 7/2^+$. Dietrich,[35] using the ^{113}Cd(p,n)^{113}In reaction, assigns $I^\pi = 5/2^+$ or $7/2^+$. A possible 166 keV transition to the $5/2^+$ 1024.2 keV level seen by Dietrich is not observed in this work. The angular distribution measurement of the 1191.3 keV γ ray is taken to be a transition from a level of that energy with $I^\pi = 7/2^+$. In order to best fit the angular distribution data, a small mixing ratio (mostly M1 radiation) must be chosen.

1688.8 keV level. A γ ray of 497.5 keV connects this level with the 1191.3 keV level. The angular distribution measurements for this γ ray supports $\Delta\ell = 2$ or $\Delta\ell = 0$. For a transition from $I = 11/2$ to $I = 7/2$ ($\Delta\ell = +2$) these measurements yield $\alpha_2 = 0.32 \pm 0.05$ and $\alpha_4 = 0.34 \pm 0.12$. The α_2 value is a bit low, and is also not consistent with the α_4 value. A better fit ($\alpha_2 \sim 0.67$, $\alpha_4 \sim 0.21$) can be obtained for a transition from $I = 7/2$ to $I = 7/2$ ($\Delta\ell = 0$), but

this seems an unlikely assignment because no 1688.8 keV γ ray was observed. Thus, with some reservation, the 1688.8 keV level is assigned $I^{\pi} = 11/2^{+}$.

2389.7 keV level. A γ ray of 700.9 keV connects this level with the 1688.8 keV level. The angular distribution measurements for this γ ray support only $\Delta\ell = 1$ with a large δ. By using a $\delta_{701} = +7.0$ for a $13/2^{+} \rightarrow 11/2^{+}$ transition, the consistent set of values $\alpha_2 = +0.68 \pm 0.20$ and $\alpha_4 = 0.29 \pm 0.11$ may be obtained. The large δ indicates the parity is the same as that of the 1688.8 keV level, so the assignment $I^{\pi} = 13/2^{+}$ is preferred.

2358.8 keV level. Because a 670.0 keV γ ray is seen in coincidence with the 497.5 and 1191.3 keV γ rays but is not seen in coincidence with the 700.9 keV γ-ray, a level at 2358.8 keV has been proposed. The proximity of this level to the previous one, and the DCO measurements suggest $I^{\pi} = 15/2^{+}$.

CHAPTER 6

DISCUSSION AND CONCLUSIONS

In this chapter the results of this work will be discussed within the framework of applicable nuclear models. The first section discusses the Coulomb excitation results and compares them to theoretical predictions. The second section discusses the (HI,xn) results, and because of the lack of theoretical predictions, only speculates on the character of states observed. The final section briefly states the conclusions which can be drawn.

1. DISCUSSION OF STRUCTURE (COULOMB EXCITATION)

The level structures deduced from the Coulomb excitation experiment are summarized in Tables 6-1 and 6-2 and are displayed graphically in Figures 6-1 and 6-2.

Generally speaking, Coulomb excitation emphasizes collective features which, in a particle-core coupling model for the odd In nuclei, are expected to be dominated by a quintet of states with $I^{\pi} = 5/2^{+}$ to $13/2^{+}$ resulting from the coupling of a hole in the $g_{9/2}$ proton shell to the one phonon vibrational level (2_1^{+}) of the adjacent even Sn nucleus ($g_{9/2}^{-1} \otimes 2_1^{+}$). If the coupling strength is weak (weak coupling model) the sum of the $B_{ex}(E2)$'s for the multiplet should be the same as $B_{ex}(E2,0^{+} \rightarrow 2^{+})$ for the adjacent even Sn core, and the $B_d(E2)$ for each member of the multiplet should be the same as $B_d(E2,2^{+} \rightarrow 0^{+})$ of the adjacent Sn core. Furthermore, the center of gravity of the multiplet should be the energy of the first 2_1^{+} state of

TABLE 6-1

Comparison of calculated and experimental $B_d(E2)$ values of ^{115}In

$I_i^\pi \rightarrow I_f^\pi$	$B_d(E2)$ ($\times 10^{-50} e^2 cm^4$)				
	Experiment (this work)	Dietrich[a] (Ref. 45)	Sen (Ref. 47)	Covello (Ref. 46)	Abecasis (Ref. 49)
$5/2_1^+ \rightarrow 9/2_g^+$	0.45 ± 0.03		0.5[b]		1.4
$5/2_2^+ \rightarrow 9/2_g^+$	3.78 ± 0.20	6.6 ± 0.7[d]	4.1[b]	5.2[d]	1.7
$5/2_2^+ \rightarrow 5/2_1^+$	$7\ ^{+\ 264}_{-\ 7}$				
$11/2^+ \rightarrow 9/2_g^+$	8.35 ± 0.43	8.1 ± 0.8	6.3[c]	7.8	8.2
$13/2^+ \rightarrow 9/2_g^+$	4.04 ± 0.22	5.0 ± 0.5	4.4[c]	5.0	5.0
$13/2^+ \rightarrow 11/2^+$	$2.3\ ^{+\ 18.1}_{-\ 2.3}$		1.0[b]	1.8	2.3
$9/2_1^+ \rightarrow 9/2_g^+$	1.5 ± 0.1	1.8 ± 0.2[d]	1.4[b]	2.1[d]	2.3
$9/2_1^+ \rightarrow 11/2^+$	$5\ ^{+\ 158}_{-\ 5}$		0.5[b]	1.6[d]	2.7
$7/2^+ \rightarrow 9/2_g^+$	1.20 ± 0.17	1.5 ± 0.2	1.9[c]	1.5	1.0
$7/2^+ \rightarrow 5/2_2^+$	$1.7\ ^{+\ 256}_{-\ 1.7}$		0.3[b]	3.4[d]	
$9/2_2^+ \rightarrow 9/2_g^+$	0.87 ± 0.09		0.8[b]		0.0
$9/2_2^+ \rightarrow 5/2_1^+$	$16\ ^{+\ 59}_{-\ 7}$				
$9/2_2^+ \rightarrow 11/2^+$	$289\ ^{+\ 2034}_{-\ 272}$				

a. Interpolated from plot using A = 3.0 MeV; assume 10% interpolation error.
b. Result from extended hole-core model, see text for discussion.
c. Result from hole-core model, see text for discussion.
d. Based upon assumption that $5/2_2^+$ and $9/2_1^+$ carry all the strength of the $5/2^+$ and $9/2^+$ members of the $g_{9/2}^{-1} \otimes 2_1^+$ multiplet.

TABLE 6-2

Comparison of calculated and experimental $B_d(M1)$ values for ^{115}In

$I_i^\pi \rightarrow I_f^\pi$	$B_d(M1) \times 10^2/(e\hbar/2Mc)^2$				
	Experiment (this work)	Dietrich[a] (Ref. 45)	Sen (Ref. 47)	Covello (Ref. 46)	Abecasis (Ref. 49)
$11/2^+ \rightarrow 9/2^+_g$	30^{+53}_{-15}	23 ± 5	18	21	15.9
$13/2^+ \rightarrow 11/2^+$	64 ± 4	34 ± 7	39	30	30.2
$9/2^+_1 \rightarrow 9/2^+_g$	$0.03^{+2.7}_{-0.03}$	1.2 ± 0.3[b]		2[b]	1.7
$9/2^+_1 \rightarrow 11/2^+$	37^{+50}_{-12}	48 ± 10[b]	66	35[b]	37.5
$7/2^+ \rightarrow 9/2^+_g$	20^{+60}_{-16}	33 ± 7	25	26	18.2
	0.5 ± 0.3				
$7/2^+ \rightarrow 5/2^+_2$	70^{+193}_{-55}	51 ± 11[b]	56	42[b]	30.5
$9/2^+_2 \rightarrow 9/2^+_g$	3^{+12}_{-2}				0.6
$9/2^+_2 \rightarrow 11/2^+$	26^{+236}_{-20}				

a. Interpolated from plot with $g_R = 0.2$, $A = 3.0$ MeV; assume 20% error from interpolation.

b. Based upon assumption $5/2^+_2$ and $9/2^+_1$ carry all of the core-coupled strength of the $5/2^+$, $9/2^+$ members of the $g^{-1}_{9/2} \otimes 2^+_1$ multiplet.

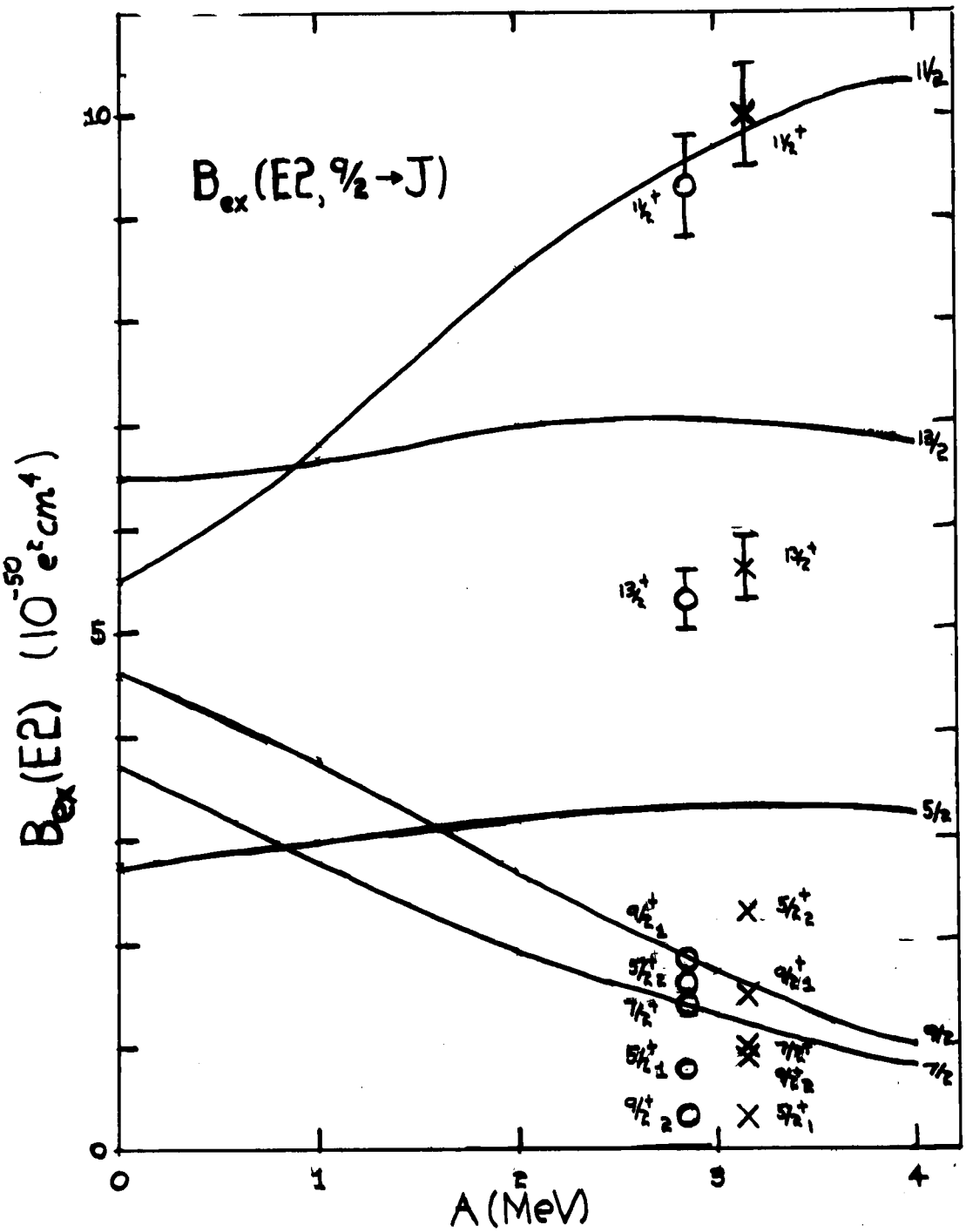


Figure 6-1. Plot obtained by Dietrich of $B_{ex}(E2,9/2 \rightarrow J)$ versus coupling strength for the $g_{9/2}^{-1} \otimes 2_1^+(Sn)$ multiplet in ^{115}In. Data points are this work; the 0 are ^{113}In values, the X are ^{115}In values.

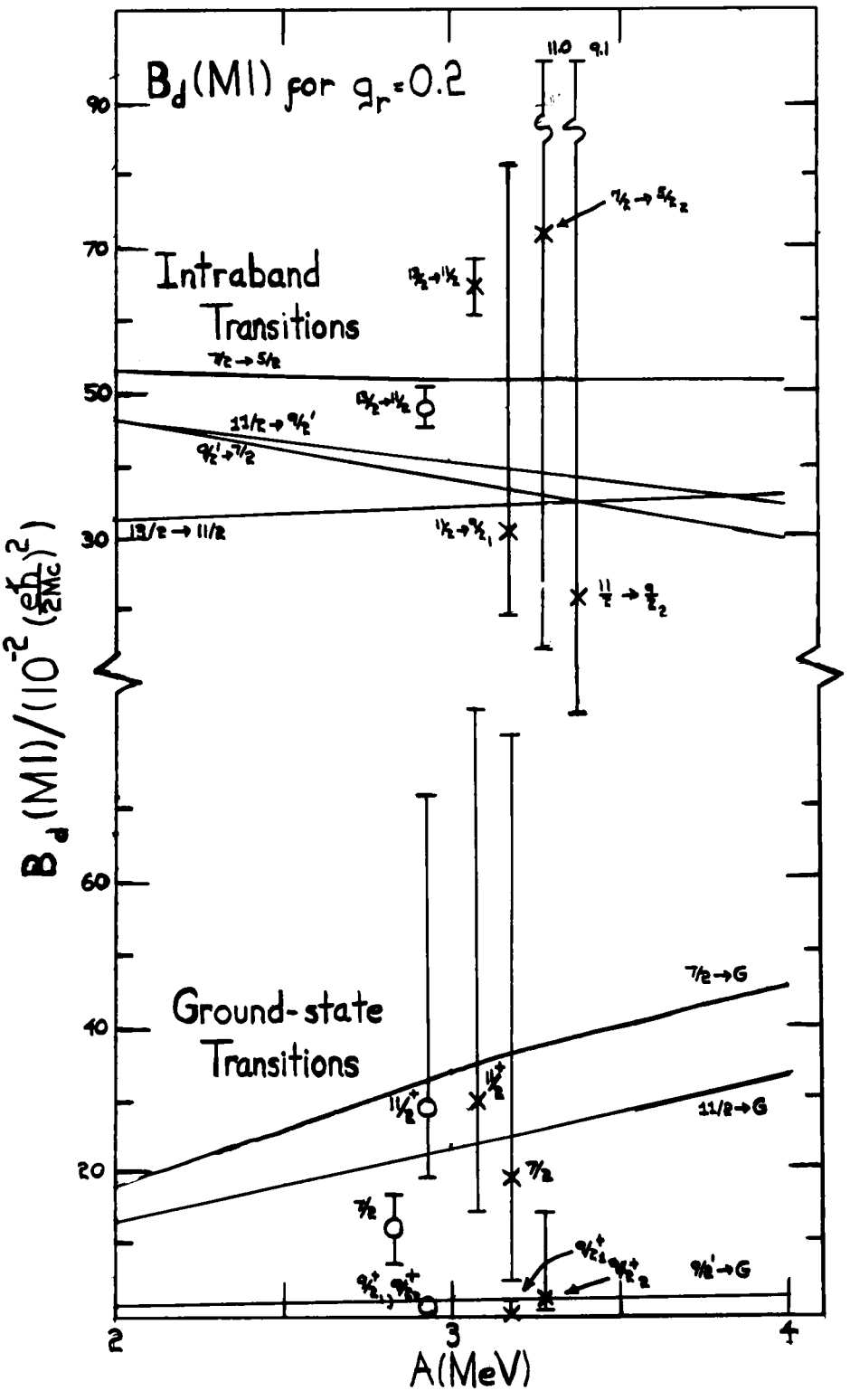


Figure 6-2. Plot calculated by Dietrich of B(M1) values versus coupling strength for the $g_{9/2}^{-1} \otimes 2_1^+$(Sn) multiplet in ^{115}In. Data points are this work; the O are ^{113}In values, the X are ^{115}In values.

the adjacent even Sn core, and there can be no M1 component in the ground-state transitions.

Ground State and First Two Excited States

Consideration of the spherical shell model levels leads one to expect the ground state and first excited state of the odd In nuclei to be described by holes in the $1g_{9/2}$ and $2p_{1/2}$ proton orbits. This was established, by the work of Silverburg[36] and verified by transfer studies.[32,34,37-39]

The second excited state has been shown[32,34,37-42] to have $I^{\pi} = 3/2^{-}$. A state of this nature can arise from a hole in the $2p_{3/2}$ proton orbit or from the coupling of a hole in the $2p_{1/2}$ proton orbit to the one phonon (2_1^+) state ($P_{1/2}^{-1} \otimes 2_1^+$) in the adjacent even Sn nucleus. The former state has been calculated[43] to lie about 1.2 MeV, which is the region where the latter could be expected. This being the case, they could interact strongly, so that one is pushed down in energy. Silverburg[36] suggested, and experiments have verified, that the second state is primarily $2p_{3/2}^{-1}$ in character. However, as evidenced by E3 excitation, there may also be some collective (possibly) $g_{9/2}^{-1} \otimes 3^{-}$) character to this state.

Core-Coupled States

The observation of two $5/2^+$ and two $9/2^+$ states poses somewhat of a dilema. Specifically, which of these are the members of the $g_{9/2}^{-1} \otimes 2_1^+$ multiplet and what is the origin of the others?

In reality, states of the same spin probably contain some component of the multiplet wave function. However, examination of the (BE2)

values suggests that the higher lying of the two $5/2^+$ states and the lower lying of the two $9/2^+$ states contain the large component of the $g_{9/2}^{-1} \otimes 2_1^+$ multiplet wave function. For ^{115}In, the choice between $5/2^+$ levels is more apparent than the choice between $9/2^+$ levels. The converse holds for ^{113}In.

Having selected candidates for members of the $g_{9/2}^{-1} \otimes 2_1^+$ multiplet, one can now further compare the data to the predictions of the weak coupling model. For ^{115}In, the center of gravity, as given by Equation (2-28) is 1287 keV which is in good agreement with the energy (1293 keV) of the 2_1^+ level in ^{116}Sn. The sum of the $B_{ex}(E2)$ for the multiplet is $20.5 \pm 0.5 \times 10^2 e^2 fm^4$ which compares with the value $B_{ex}(E2, 0^+ \rightarrow 2^+) = 21.6 \pm 0.6 \times 10^2 e^2 fm^4$ for ^{116}Sn. Inclusion of the $B_{ex}(E2)$ for the two "extra" states makes the agreement perfect. However, for ^{113}In, the agreement is not as good. The E_{cg} for the multiplet of ^{113}In and the energy of the 2_1^+ state in ^{114}Sn are, respectively, 1349 and 1300 keV. Furthermore, the sum of the $B_{ex}(E2)$'s for the multiplet is $19.4 \pm 0.6 \times 10^2 e^2 fm^4$ for ^{114}Sn. This latter value was obtained from systematics of the $B_{ex}(E2, 0^+ \rightarrow 2^+)$ for the even Sn nuclei as given by Stelson.[44] Inclusion of the "extra" states does not help significantly. Finally, there are other discrepancies from the model as evidenced in the data for both nuclei. These include appreciable M1 components in ground state transitions, uneven distribution of the $B_d(E2)$ strength, and the large energy separation of the multiplet compared to the energy of the core 2_1^+ state.

Theoretical Studies

In order to explain discrepancies such as discussed above, there have been a number of theoretical studies dealing with the structure of the odd In nuclei. The results of this experiment will be compared to the four of them which are best suited to the nature of this experiment. These comparisons are summarized in Figures 6-1 and 6-2 and in Tables 6-1 and 6-2.

The first study considered was the one by Dietrich.[45] Here a rather simple model for ^{115}In was used in that only the coupling of a $1g_{9/2}$ proton hole to the zero, one, and two quadrupole phonon vibrations of the ^{116}Sn core was considered. The interaction strength A, as defined by

$$\langle (9/2)^{-1} n' R' J | H_{int} | (9/2)^{-1} n R J \rangle$$

$$= (-1)^{J-1/2} \begin{Bmatrix} J & 9/2 & R \\ 2 & R' & 9/2 \end{Bmatrix} \langle n' R' \| \alpha_2^\dagger + \alpha_2 \| n R \rangle A \,, \qquad (6\text{-}1)$$

is treated as a parameter. Plots of energy levels and $B_{ex}(E2)$ strengths were developed as a function of A, the latter of which is reproduced in Figure 6-1.

The agreement with experiment for a value of $A \tilde{=} 3.0$ MeV is surprisingly good. The sequence of energy levels is well reproduced except for inversion of the $11/2^+$ and $5/2^+$ states in both nuclei which lie close together, and for ^{113}In, the inversion of the $7/2^+$ and $9/2^+$ states which also are close lying. Increasing the coupling strength will help the latter situation, but at a cost of hurting the overall agreement. Examination of Figure 6-1 shows how well the data fit the

predicted $B_{ex}(E2)$ values. For good agreement, one need only consider one of the $9/2^+$ levels, but for the $5/2^+$ levels, the sum of both $B_{ex}(E2)$ is still short of the predicted value. Otherwise, the biggest discrepancy is with the $13/2^+$ level. From this plot it would appear that the coupling strength needs to be a little stronger for ^{115}In than for ^{113}In. To calculate M1 transition strengths, another adjustable parameter g_R (core gyromagnetic ratio) is introduced. In Figure 6-2 Dietrich's[45] plots of M1 transition strengths versus A for his "best" value of g_R are reproduced. The overall agreement is not as good as that of the E2 strengths, but generally speaking it is more difficult to precisely measure M1 strengths. Certainly the results are the right order of magnitude and again suggest that the coupling strength is a bit stronger for ^{115}In than for ^{113}In. In Tables 6-1 and 6-2 are listed the values obtained by Dietrich for E2 and M1 transition strengths using his "best" values of A = 3.0 MeV and $g_R = 0.2$.

A study in the same spirit as Dietrich,[45] but more extensive, was performed by Covello.[46] This study considered holes in the $1g_{9/2}$, $2p_{1/2}$, $2p_{3/2}$, and $1f_{5/2}$ proton shells coupled to core excitations of up to three quadrupole and one octupole phonons. Also, there were "no adjustable parameters." Such an enlarged model space gives rise to other $5/2^+$ and $9/2^+$ levels, as well as some low spin, positive parity states such as seen in other experimental studies.[32,40-42,47] The results of Covello's calculations for E2 and M1 transition strengths are listed in Tables 6-1 and 6-2. The overall level structure determined was similar to that of Dietrich. No additional positive

parity states were predicted below 2 MeV, and the electromagnetic properties of the $g_{9/2}^{-1} \otimes 2_1^+$ multiplet are similar.

Sen[47] has performed two types of calculations. First, his "hole-core (h.c.)" model uses the same model space as Covello,[46] but treats the coupling strengths and single hole energies as variables. Secondly, his "extended hole core (e.h.c.)" model attempts to explain discrepancies such as discussed previously by considering the coexistence of a $K = 1/2^+$ rotational band built on a deformed Nilsson [431] state with the core coupled states. This postulate of deformation has previously been used to explain the character of $1/2^+$, $3/2^+$ levels in odd In nuclei (see Ref. 48 for a recent discussion). With this coexistence, some of the "deformed states" could mix with the core-coupled states, affecting the results as determined by the simpler core-coupled model. Sen treats the interaction matrix for this mixing as a variable, considering only the $5/2^+$ and $9/2^+$ states to be mixed. The results of his calculations are included in Tables 6-1 and 6-2, the e.h.c. model results are used whenever possible. This model seems to give a good explanation for the "extra" states, but this may be a result of having more parameters.

A different type of approach to explain the "extra" states and other discrepancies has been explored by Abecasis.[49] Here, in a "generalized semimicroscopic" model, the usual space of the hole phonon coupling model is enlarged by the inclusion of the degrees of freedom associated with the incoherent two-hole-one-particle (2h-1p) modes of excitation. This theory predicts "extra" $1/2^+$, $3/2^+$, $5/2^+$, and $7/2^+$ states. Again, results are listed in Tables 6-1 and 6-2.

A comparison of the four theories and the data suggests that to first order, an intermediate coupling strength in a particle-core coupling model provides a good explanation of the features of $^{113,115}In$ as seen in Coulomb excitation.

2. DISCUSSION OF STRUCTURE OBSERVED IN THE $^{110}Pd(^{6}Li,3n)^{113}In$ REACTION

The five states constituting the $g_{9/2}^{-1} \otimes 2_1^+$ multiplet are also seen in the $^{110}Pd(^{6}Li,3n)^{113}In$ reaction. As expected, the yield of the higher spin members is predominent. Generally speaking, one might expect levels feeding this multiplet to be members of multiplets formed by coupling holes (predominately in the $g_{9/2}$ orbital) to the two quadrupole phonon or one octupole phonon core vibrations.

2233.1 keV Level

Because the most probable spin-parity assignment for this level is $15/2^-$, it is the logical candidate to be the highest spin member of the $g_{9/2}^{-1} \otimes 3^-$ multiplet, and as such, the most strongly populated. This is consistent with the energy of the 3^- state in ^{114}Sn being 2.275 MeV.[50]

2282.7 keV Level

Because the most probable spin-parity assignment for this level is $17/2^+$, it is a logical candidate to be the highest spin member of the $g_{9/2}^{-1} \otimes 4_2^+$ multiplet. This is supported by the strength of the 938.3 keV transition to the $13/2^+$ 1344.4 keV level which is the highest spin

member of the $g_{9/2}^{-1} \otimes 2_1^+$ multiplet. Furthermore, the energy of the 4_2^+ level in ^{114}Sn is 2.187 MeV.[50]

2164.8, 2224.7, 2264.1, 2442.3 keV Levels

Since these levels feed the high spin members of the $g_{9/2}^{-1} \otimes 2_1^+$ multiplet, but are not populated as strongly as the preceeding two levels, the best assumption one can make regarding their character is that they are other high spin members of the $g_{9/2}^{-1} \otimes 3^-$ and $g_{9/2}^{-1} \otimes 4_1^+$ multiplets. They also could be high spin members of the $g_{9/2}^{-1} \otimes 2_2^+$ multiplet, although a candidate for the second 2^+ member in ^{114}Sn has not been found.

1472.9, 1536.2, and 1590.7 keV Levels

These levels feed only the $3/2^-$ 646.9 keV state which has mostly a $p_{3/2}^{-1}$ character.[36] One possibility for their character is that they carry some $f_{5/2}^{-1}$ strength. In ^{115}In, the $f_{5/2}^{-1}$ strength has been shown[37] to be split. But, since there apparently is some $g_{9/2}^{-1} \otimes 3^-$ character to the $3/2^-$ 646.9 keV state, another possibility is that these states contain some of the low spin character of the $g_{9/2}^{-1} \otimes 3^-$ multiplet.

1191.3, 1688.8, 2358.8, and 2389.7 keV Levels

These levels are strongly populated in the ^{110}Pd(^{6}Li,3n)^{113}In reaction but have no observed transitions to those levels populated by Coulomb excitation. Thus, these levels are good candidates for the proposed[48] $K = 1/2^+$ rotational band built on a Nilsson [431] state. This possibility was investigated by searching for the transition from the 1191.3 keV level to the $I^\pi = 3/2^+$ member of the band (either 1029 or 1064 keV). It was not found, but this may be due to poor statistics.

In ^{115}In, the analogous $7/2^+$ level decays only $\sim$ 0.2% of the time to the $3/2^+$ level. A good fit to the Equation (2-32) could not be found. This is complicated by the uncertainty in assignment of spin-parity for the 1029.7 and 1064.2 levels. This is especially true if the assignments are $1/2^+$ and $3/2^+$ respectively as Meyer[51] and Dietrich[35] suggest. These assignments would reverse the trend observed[48] in ^{115,117,119}In. However, a fit to Equation (2-32) as good as that found for ^{115,117,119}In may be obtained.

169.6, 189.5, 267.7, 163.3 keV Cascade

Perhaps the most startling feature observed in the ^{110}Pd(^{6}Li,3n)^{113}In experiment was the rather strong 169.6, 189.5, 267.7, 163.3 keV cascade feeding the 2233.1 keV level. Bands of these type (but a factor of two higher in energy) have been seen[52] in the odd mass Sb nuclei. However, the type of explanation used in the Sb case cannot be applied in this case. Thus, the nature band remains quite puzzling and poses an interesting theoretical problem.

3. CONCLUSIONS

Coulomb Excitation

As indicated earlier, the results of the measurements are summarized in Tables 5-5 and 5-6 (pages 83 and 84). From this, a remarkable similarity between the two nuclei is readily apparent. Their structure is, to first order, explained by a particle-core coupling model with intermediate coupling strength. Differences observed between the structure of the two nuclei are as follows: 1) Inversion of the core-coupled

$7/2^+$ and $9/2^+$ states, 2) stronger excitation of the lower of the two $5/2^+$ states in ^{113}In vs ^{115}In, and 3) weaker excitation of the higher of the two $9/2^+$ states in ^{113}In vs ^{115}In.

(HI,xn)

From this experiment good candidates for members of the multiplets formed by coupling a $g_{9/2}$ hole to two quadrupole phonon and one octupole phonon core vibrations are observed. In addition, there is a candidate for the proposed $K = 1/2^+$ rotational band. Finally, there is an unusual cascade of γ rays with energies on the order of 200 keV feeding a level at 2233 MeV. The nature of this cascade is very puzzling and poses an interesting theoretical problem.

REFERENCES

REFERENCES

1. Webster's Seventh New Collegiate Dictionary, G & C. Merriam Company, 1969, p. 544.

2. J. P. Davidson, Collective Models of the Nucleus, Academic Press, 1968.

3. J. M. Eisenberg and W. Greiner, Nuclear Models, North-Holland Publishing Company, 1970.

4. M. A. Preston, Physics of the Nucleus, Addison-Wesley Publishing Company, Inc., 1962.

5. A. Bohr, Dan. Mat. fys. Medd. 26, No. 14 (1952).

6. A. Bohr and B. R. Mottelson, Dan. Mat. fys. Medd. 27, No. 16 (1953).

7. S. G. Nilsson, Dan. Mat. fys. Medd. 29, No. 16 (1955).

8. M. G. Mayer, Phys. Rev. 75, 1969 (1949).

9. O. Haxel, J. H. P. Jensen, and H. E. Suess, Phys. Rev. 75, 1766 (1949).

10. P. F. A. Klinkenberg, Revs. Mod. Phys. 24, 63 (1952).

11. C. F. Von Weizsäcker, Z. Physik 96, 431 (1935).

12. S. Flügge, Ann. d. Phys. 39, 373 (1941).

13. J. Rainwater, Phys. Rev. 79, 432 (1950).

14. E. Merzbacher, Quantum Mechanics, John Wiley and Sons, 1961.

15. K. Alder, A. Bohr, T. Huus, B. R. Mottelson, Rev. Mod. Phys. 28, 432 (1956).

16. W. T. Milner, Doctoral Dissertation, Univ. of Tennessee, 1968 (unpublished).

17. R. O. Sayer, Doctoral Dissertation, Univ. of Tennessee, 1968 (unpublished).

18. A. Winther and J. deBoer, A Computer Program for Multiple Coulomb Excitation, Calif. Inst. of Technology, Technical Report, 1965.

19. J. O. Newton, Nuclear Spectroscopy and Reactions, part C, ed. J. Cerny, Academic Press, 185 (1974).

20. G. J. Smith, Doctoral Dissertation, Purdue University, 1972, (unpublished).

21. J. R. Grover and J. Gilat, Phys. Rev. 157, 802 (1967).

22. T. Yamazaki, Nucl. Data Tables A3, 1 (1967).

23. E. der Mateosian and A. W. Sunyar, Atom. Nucl. Data Tables 13, 391 (1974).

24. R. M. Diamond, E. Matthias, J. O. Newton, F. S. Stephens, Phys. Rev. Lett. 16, 1205 (1966).

25. K. S. Krane, R. M. Steffen, and R. M. Wheeler, Nucl. Data Tables 11, 351 (1973).

26. J. A. Graw, Z. W. Grabowski, F. A. Rickey, P. C. Simms, and R. M. Steffen, Phys. Rev. Lett. 32, 677 (1974).

27. H. J. Kim, R. Ballini, B. Delaunay, J. Delaunay, J. P. Fovan, and M. Pichevar, (to be published in Nucl. Phys.).

28. H. J. Kim (private communication).

29. P. B. Fossan and E. K. Warburton, Nuclear Spectroscopy and Reactions, part C, ed. J. Cerny, Academic Press, 307 (1974).

30. W. T. Milner, ORNL High Voltage Laboratory Computer Handbook, 1975 (unpublished).

31. C. D. Moak, H. E. Banta, J. N. Thurston, J. W. Johnson, and R. F. King, Rev. Sci. Inst. 30, 694 (1959).

32. S. Raman and H. J. Kim, Nucl. Data Sheets 16, 195 (1975).

33. R. G. Stokstad, I. A. Fraser, I. S. Greenberg, S. H. Sie, and D. A. Bromley, Nucl. Phys. A156, 145 (1970).

34. R. G. Markham and H. W. Fulbright, Phys. Rev. C9, 1633 (1974).

35. W. Dietrich and A. Backlin, Uppsala U. Institute Phys. Rept. 881, (1974) (to be published in Physica Scripta).

36. L. Silverburg, Arkiv. Fysik 20, 341 (1961).
L. Silvergurg, Nucl. Phys. 60, 483 (1964).
L. Silverburg, Nucl. Phys. A119, 385 (1968).

37. W. H. A. Hesselink, B. R. Kooistra, L. W. Put, R. H. Siemssen, and S. Y. Van der Werf, Nucl. Phys. A226, 229 (1974).

38. M. Conjeaud, S. Harar, and E. Thuriere, Nucl. Phys. A129, 10 (1969).

39. C. Weiffenbach and R. Tickle, Phys. Rev. C3, 1668 (1971).

40. F. E. Bertrand, Nuclear Data Sheets 6, 1 (1971).

41. S. Raman and H. J. Kim, Nuclear Data Sheets 6, 39 (1971).

42. S. Raman and H. J. Kim, Nuclear Data Sheets 5, 181 (1970).

43. V. R. Pandharipande, Nucl. Phys. A100, 449 (1967).

44. P. H. Stelson, F. K. McGowan, R. L. Robinson, and W. T. Milner, Phys. Rev. C2, 2015 (1970).

45. F. S. Dietrich, B. Herskind, R. A. Naumann, R. E. Stokstad, and G. E. Walker, Nucl. Phys. A155, 209 (1970).

46. A. Covello, V. R. Manpredi, and N. Azziz, Nucl. Phys. A201 (1973).

47. S. Sen, Nucl. Phys. A191, 29 (1972).

48. J. McDonald, B. Fogelberg, A. Backlin, and Y. Kawase, Nucl. Phys. A224, 13 (1974).

49. S. M. Abecasis, O. Civitarese, and F. Krmpotic, Phys. Rev. C9, 2320 (1974).

50. H. J. Kim, Nuclear Data Sheets 16, 107 (1975).

51. R. A. Meyer, (to be published in Zeitschrift für Physik).

52. A. K. Gaigalas, R. E. Shroy, G. Schatz, and D. B. Fossan, Phys. Rev. Lett. 35, 555 (1975).

VITA

William Kelley Tuttle III was born in Sacramento, California, on July 8, 1942. He attended elementary, junior high, and high school in Dallas, Texas, and graduated from Highland Park High School in 1960. The following September he entered the University of Texas at Austin, and in January, 1965, he received a Bachelor of Science degree in Physics. He then entered Fresno State College, Fresno, California to begin work on a Master's degree in Physics, which he received in May, 1967. After receiving his Master's degree he was employed by the U. S. Naval Ordinance Laboratory, Corona, California.

In September, 1970, he accepted a fellowship at the University of Tennessee, Knoxville, and began study toward a Doctor of Philosophy degree with a major in Radiation Physics.

He is married to the former Charlene Estelle Brand and has one son, William Kelley Tuttle IV born July 4, 1968.